Exploring large coherent spin systems with solid state NMR

by

HyungJoon Cho

Submitted to the Department of Nuclear Science and Engineering
in partial fulfillment of the requirements for the degree of

Doctor of Philosophy in Nuclear Science and Engineering

at the

MASSACHUSETTS INSTITUTE OF TECHNOLOGY

Feb 2005

Author .....
Department of Nuclear Science and Engineering
Jan 28, 2005

Certified by .....
David G. Cory
Professor
Thesis Supervisor

Read by .....
Sow-Hsin Chen
Professor
Thesis Reader

Accepted by .....
Jeffrey Coderre
Chairman, Department Committee on Graduate Students

Exploring large coherent spin systems with solid state NMR

by

HyungJoon Cho

Submitted to the Department of Nuclear Science and Engineering
on Jan 28, 2005, in partial fulfillment of the
requirements for the degree of
Doctor of Philosophy in Nuclear Science and Engineering

Abstract

Solid state Nuclear Magnetic Resonance (NMR) allows us to explore a large coherent spin system and provides an ideal test-bed for studying strongly interacting multiple-spin system in a large Hilbert space.

In this thesis, we experimentally investigate the spin dynamics in a rigid lattice of dipolarly coupled nuclear spins using multiple quantum NMR spectroscopy. Encoding multiple quantum coherences (MQC) in an arbitrary quantizing axis is developed. We utilized this method to encode coherence numbers in an orthogonal basis to Zeeman basis and showed that the dipolar-ordered state is a two spin correlated state, and confirmed the presence of the $I_i^+ I_j^- + I_i^- I_j^+$ (flip-flop) terms in the experimentally prepared dipolar-ordered state. A new experimental investigation of the problem of the NMR free induction decay (FID) in a lattice of spin 1/2 nuclei is presented to verify the multi-spin nature of the FID and the dominant role of the geometrical arrangement of the spins in the development of higher order correlations under the dipolar evolution. To study the dynamics and the controllability of these multiple spin correlations, effective decay times of individual coherence orders are measured under the dipolar interaction and under the control sequence that suppresses the dipolar evolution. It is seen that the decay time of each coherence order becomes shorter and more uniform among different coherence orders as the spin correlation size grows larger in both cases.

Additional work has been done in this thesis, toward creating a pure state in solid state nuclear spins by transferring polarization from electron spins, i.e Dynamic Nuclear Polarization (DNP). A new cryogenic DNP probe was developed enabling multiple pulse irradiations at low temperature with enhanced polarization.

Thesis Supervisor: David G. Cory
Title: Professor

Acknowledgments

I have been privileged to work with many wonderful people during my thesis work at MIT. Professor David G. Cory invited me to join his group when I was not sure what to do and guided me through this work with patience and thoughtful insight throughout my time in his Lab. I still remember the one night in the Lab when he showed me how to strip off a coaxial cable. It is a great pleasure to thank Dr. Chandrasekhar Ramanathan not only for his help on every single aspect of my work but also for his warm support when things are not working well. His support and advice pushed me through many hurdles to reach here. I am thankful for Dr. Timothy Havel for making me challenge myself starting from first principles. I cannot thank enough Greg Boutis for a wonderful time we spent in the Lab together for my initial two years in Cory Lab and his solid friendship. He generously passed me on his valuable skills, which he learned from trials and errors.

Of my lab-mates, I enjoyed working with Paola Cappellaro, Daniel Greenbaum and Suddhasattwa Sinha on solid state NMR work. I believe we had constructive interferences with each other. I shared mind-clearing break at the back of NW14 building with Nicolas Boulant, and regret that we didn't share any research experience together.

I also would like to thank Debra Chen and Yaakov Weinstein for going through NUKE qualifiers together, it was a rewarding experience to work out lists of problem sets with them. I am thankful for Jamie Yang and Michael Henry taking over magnet cryogen maintenance work.

My lab mates and friends, Joseph Emerson, Dmitry Pushin, Tirthahalli Mahesh, Jonathan Hodges, Tatjana Atanasijevic, Gabriela Leu, Ruopeng Wang, Yong Xiao and Yun liu were always there when I needed them. I will look back fondly on many aspects of activities we shared together at MIT.

Outside MIT, I had trustworthy relationships with my roommates, Hyunkyu Kim, Kyujin Cho, and Sangyoon Min. They were great people to be around. We shared valuable moment of our lives and hope our friendships last our lifetime. I also want

to thank Unnam Park and Kyungjin Lee for inviting me to Redsox Nations and their hospitalities.

Back in Korea, a group of my friends (DON1974) provided me with warm relief of not being alone while I am away from my home town. I had to pay a price of not being able to attend any single of my friends' weddings for completing my work here, and I will miss those precious moments slipped by.

My parents, my brother and sister in law have been a huge moral support to me. They made me think that I am doing one of the most valuable things in the world. Without them, I would not be here today.

Finally, I would like to thank Eunmi Choi, my fiance, for being there. She lights up my life. *S.D.G.*

For my parents ;

Chungnam Cho

and

Youngho Choi.

Contents

List of Figures

List of Tables

Chapter 1

Introduction

The availability of coherent control methods, a well-known internal Hamiltonian, and a relatively long decoherence time of nuclear spins in Nuclear Magnetic Resonance (NMR) have collectively made NMR one of the most ideal test-beds for Quantum Information Processing (QIP). Liquid state NMR allowed us to implement key quantum algorithms and to develop coherent control methods in small quantum systems with pseudo-pure initial state preparation followed by ensemble measurement on identical molecules [1, 2]. Even if liquid state NMR is currently by far the leading technology for QIP among various experimental modalities, these studies have been limited up to 10 qubits, mainly because creating the pseudo-pure state from highly mixed states at room temperature requires exponential costs either in the signal strength or the number of experiments involved.

Dipolarly coupled nuclear spins in solid state NMR hold potential promise in the approach of designing and implementing scalable quantum information processors. Key advantages of solid state NMR are that we can achieve a nearly pure state with existing methods, and that stronger dipolar interaction (typically on the order of tens of kHz in dielectric crystal) can be used to achieve faster operation times within coherent regime. Moreover, spatial addressing of the spins using gradient field might possibly overcome control issues arising from the chemistry addressing method, which is mainly used in liquid state NMR to address the qubits. There have been various proposals for scalable solid state NMR-QIP utilizing the above advantages of dipolarly

coupled spins.

1. Cory *et al.* proposed to use ensemble solid state NMR quantum information processor, using large number of n-qubit fixed in a lattice. The lattice is deuterated, and paramagnetic impurities are used to dynamically polarize the deuterium spins and this enhanced polarization is transferred to QIP molecules [3].

2. Kane as well as other researchers brought silicon into the picture, which can potentially take advantage of the existing infrastructure of the semiconductor industry. Kane proposed to use phosphorus atoms 20 nanometers apart in a silicon grid at low temperature followed by single nuclear spin measurement [4]. Ladd *et al.* proposed to use an all silicon quantum computer, in which qubits are addressed using the magnetic field gradient of microfabricated ferromagnets and measurements are performed via magnetic resonance force microscopy (MRFM) [5].

3. Suter and Lim proposed to use a solid state spin based quantum computer that uses endohedral fullerenes, which can be positioned on the silicon surface. In this approach, each local qubit is stored in nuclear and electron spins, and qubits are addressed using magnetic field gradients [6].

Whichever architectures we decide to pursue, it is essential that we understand the dynamics of spins in a large Hilbert space under the action of many-body Hamiltonians, as well as develop the ability to accurately perform desired unitary transformations in this space.

The nuclear spins in a dielectric solid such as calcium fluoride are excellent testbeds to investigate large-scale spin dynamics and control issues in a large Hilbert space under dipolar interactions because they have very long spin-lattice relaxation times (ranging from minutes to days depending on the concentration of paramagnetic impurities in the crystal) and nuclear spins are completely isolated from the environment. It is therefore possible to investigate the dynamical behavior of coherent spins in a large Hilbert space under the action of their mutual couplings and applied radiofrequency perturbations, while they are essentially isolated from their environment [7].

In this thesis, we focus on experimental investigation of spin dynamics under a

relatively short ($t \sim 5T_2$) time regime of dipolar evolution using Multiple Quantum NMR (MQ-NMR). The long time regime of dipolar evolution ($t \sim T_1$) has recently been probed via direct spin diffusion measurements [8, 9]. It should be noted that new experimental methods and theoretical understandings to study the spin dynamics in intermediate time regime is also necessary to verify how microscopic quantum mechanical properties manifest themselves in a corresponding dynamics at the macroscopic level.

In the next chapter, we briefly introduce the notion of Multiple Quantum Coherence (MQC) in solid state NMR followed by a newly developed experimental technique to encode MQC in non-commuting bases [10]. Chapter 3 of this thesis describes the direct reconstruction of the density matrix of the dipolar-ordered state from correlated 2D MQC encoding experiments [12], and chapter 4 shows the first direct observation of multi-spin dynamics during the Free Induction Decay (FID) in a single crystal of CaF_2 [13]. In chapter 5, experimental investigations of the decay of multi-spin states under the dipolar interaction and under the 48-pulse time suspension sequence is presented. A design and construction of low temperature Dynamic Nuclear Polarization (DNP) probe for solid state NMR application is described in the last chapter, which is an effort toward state purification in solid state NMR.

Chapter 2

Encoding multiple quantum coherences in non-commuting bases

2.1 Multiple Quantum Coherences (MQC) in solid state NMR

[1] At thermal equilibrium in a high magnetic field, the density matrix of the spin system in a rigid lattice of nuclear spins can be given as

$$\hat{\rho}(0) = \frac{e^{-\beta H}}{Z}, \tag{2.1}$$

where Z is the partition function and $\beta = 1/kT$. The Hamiltonian of spin system is given as $H = H_Z + H_D$. H_Z is Zeeman interaction, which is

$$H_Z = \hbar\omega \sum_j I_{zj}, \tag{2.2}$$

and H_D is the secular dipolar interaction.

$$\hat{H}_D = \sum_{j<k} D_{jk} \left\{ \hat{I}_{jz}\hat{I}_{kz} - \frac{1}{4}(\hat{I}_{j+}\hat{I}_{k-} + \hat{I}_{j-}\hat{I}_{k+}) \right\}. \tag{2.3}$$

[1]This chapter was drawn from sections of [10] with major contribution from Dr. Chandrasekhar Ramanathan

The dipolar coupling constant D_{jk} between spins j and k is given as

$$D_{jk} = \frac{\gamma^2\hbar^2}{r_{jk}^3}(1 - 3\cos^2\theta_{jk}), \tag{2.4}$$

where γ is the gyromagnetic ratio, r_{jk} is the distance between spins j and k, and θ_{jk} is the angle between the external magnetic field and internuclear vector $\vec{r}_{jk}$.

All the spins in a rigid lattice of nuclear spins are coupled through dipolar interaction. Therefore in principle, the size of the Hilbert space of the spin system is determined by the total number of the spins in the system. However, in a high temperature ($\beta\hbar\omega \ll 1$) limit (typically valid when T>1 K) and a high field ($|H_D| \ll |H_Z|$) approximation, the equilibrium density matrix becomes

$$\hat{\rho}(0) \simeq \frac{1}{Z}(\mathbf{1} - \beta\hbar\omega\sum_j \hat{I}_{jz}) = \frac{\mathbf{1}}{Z} - \frac{\beta\hbar\omega}{Z}\sum_j \hat{I}_{jz} = \frac{\mathbf{1}}{Z} - \delta\rho, \tag{2.5}$$

where $\mathbf{1}$ is the identity. Since identity does not evolve under any interaction, it is sufficient to describe the spin system in terms of $\delta\rho$. At thermal equilibrium in a high temperature limit and a high field approximation, the dipolarly coupled spin system in a rigid lattice of nuclear spins can be treated as an ensemble of weakly coupled subsystems, in which effectively one spin out of 10^6 is pointing up at room temperature in a high magnetic field.

In a strong magnetic field ($B_0\hat{z}$), an interacting N-spin 1/2 system has 2^N stationary states. These can be classified according to the magnetic (Zeeman) quantum number,

$$M_z = \sum_j m_{zj} = (N_{(+1/2)} - N_{(-1/2)})/2, \tag{2.6}$$

where $m_{zj} = \pm 1/2$ is the individual eigenvalue of the jth spin in the system, $N_{(+1/2)} - N_{(-1/2)}$ represents the difference in the number of spins pointing up and down along a background magnetic field, and the energy eigenvalue corresponding to M_z is $E_z = -\gamma\hbar B_0 M_z$. For non-degenerate stationary states, there are on the order of 2^{2N-1} possible transitions between any two levels. The difference in M_z values between the two levels is referred to as the coherence number. This definition of coherence is

useful since Zeeman states are also eigenstates of any secular internal Hamiltonian, such as the secular dipolar Hamiltonian.

While these coherences refer to transition between levels, it is useful to discuss multiple quantum coherences for states of a system. When the state is expressed in the eigenbasis of the system, the presence of a nonzero matrix element $< z_i|\rho|z_j >$, indicates the presence of an n-quantum coherence, where $n = M_z(z_j) - M_z(z_i)$, the difference of the magnetic quantum numbers.

Since each of the N interacting nuclei retains its own Zeeman quantum number for weakly coupled systems, a particular Zeeman state can be expressed as a product of N-spin 1/2 eigenstates, given as

$$|M_z >= |m_{z1} > |m_{z2} > ...|m_{zN} >, \tag{2.7}$$

where M_z and m_{zj} are defined in Eq. (2.6).

Now the 2^{2N} basis operators are needed to form a density operator for spin-1/2 N interacting spin system, and these basis operators can be expressed as products of basis operators for each of the separate spins-1/2,

$$\rho = |m_{z1}m_{z2}...m_{zN} >< m_{zN}...m_{z2}m_{z1}| = |m_{z1} >< m_{z1}||m_{z2} >< m_{z2}|...|m_{zN} >< m_{zN}|. \tag{2.8}$$

Meanwhile, it is useful to introduce the Pauli matrices for easier manipulation of the density operators. The relationships between the Pauli matrices and the basis operators for each spin can be given as [22]

$$I_{xj} = \frac{1}{2}(|\uparrow><\downarrow| + |\downarrow><\uparrow|), \tag{2.9}$$

$$I_{yj} = -\frac{i}{2}(|\uparrow><\downarrow| - |\downarrow><\uparrow|), \tag{2.10}$$

$$I_{zj} = \frac{1}{2}(|\uparrow><\uparrow| - |\downarrow><\downarrow|). \tag{2.11}$$

With these single-spin operators as building blocks, N-spin density operators can now

be expressed as the tensor products of above single spin operators, yielding

$$\rho = \underbrace{\mathbf{1}_j \bigotimes \mathbf{1}_k \bigotimes ....}_{N-K} \underbrace{I_{\alpha l} \bigotimes I_{\beta m} \bigotimes I_{\gamma n} ...}_{K} + ..., \tag{2.12}$$

where $N - K$ is the number of non-interacting spins, and K is the total number of interacting spins in the N-spin system. K is usually defined as the size of the coherent spin cluster (spin number) in the system of interest. α, β, and γ denote x, y or z. Additionally, the x and y components of the operator can be expressed as the spherical operators with the relationships below

$$I_{\pm j} = I_{xj} \pm I_{yj}. \tag{2.13}$$

For example, states such as $I_{+j}I_{+k}$ are called two spin double quantum coherence, and $I_{+j}I_{zk}$ is called two spin single quantum coherence. Consequently, the size of a coherent spin cluster (spin number) of a thermal initial state ($\rho(0) = \sum_j I_{zj}$) can be considered as one.

From the experimental perspective, unfortunately a spin number is not an observable quantity. On the other hand, since a coherence number is a good quantum number, we can use a collective rotation about the axis of the quantization, $\sum_i I_z^i$, to characterize coherence numbers:

$$< z_i|\exp(-i\phi \sum_i I_z^i)\rho\exp(-i\phi \sum_i I_z^i|z_j >= \exp(in\phi) < z_i|\rho|z_j > . \tag{2.14}$$

This coherence number information of quantum spin states can be recorded to the phase factor and this phase factor can be easily extracted using a method which will be explained in the next section of this chapter. To make the above explanation more concrete, Fig. 2-2 shows a Fourier transform multiple quantum spectra obtained in a single crystal of CaF_2.

Historically, the advent of Multiple Quantum (MQ) Nuclear Magnetic Resonance (NMR) techniques opened up a new possibility of describing dynamical aspects of

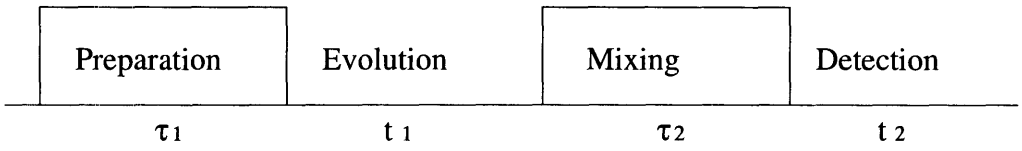

Figure 2-1: The general form of a two dimensional MQ experiment

multi-spin processes beyond thermodynamic descriptions by studying emerging multiple quantum coherences. MQ-NMR techniques in solids have generally been used to study the size and the dimensionality of localized spin clusters as well as to probe the many-body dynamics of a solid state spin system. We briefly describe previous experimental efforts and success in probing forbidden degrees of freedom in a collection of nuclear spins (1/2 spins), that is, MQ-NMR. A complementary review can be found elsewhere [19, 20, 21, 23].

The general form of a two-dimensional MQ experiment is shown in Fig. 2-1. Since the inductive measurement of NMR signal must be carried out by measuring single quantum magnetization, the periods of preparation and evolution of multiple quantum coherences are followed by a mixing period (existing multiple quantum coherences are transformed to observable single quantum during this period). In the final detection period, single quantum transverse magnetization is observed and the corresponding data are Fourier transformed to extract coherence number information. Based on this scheme, several pulse sequences are developed to create and detect multiple quantum coherences. Before the development of the time-reversed version of preparation and mixing periods, MQ-NMR spectroscopy had been generally applied to systems with a small number of spins due to the inefficiency in refocusing higher order coherences to observable magnetization [14, 15, 16, 17, 18, 19, 20]. Selective excitation scheme was also introduced to compensate for this low signal in higher order coherences by channeling the signal only to desired coherence orders [24, 25]. Utilization of time-reversal scheme enhanced the overall intensity of MQ-NMR experiment otherwise lost by refocusing dipolar interaction, [26, 27, 28] and expanded the application of MQ-NMR to strongly coupled network of spins.

The selective excitation and transformation of multiple quantum coherences led

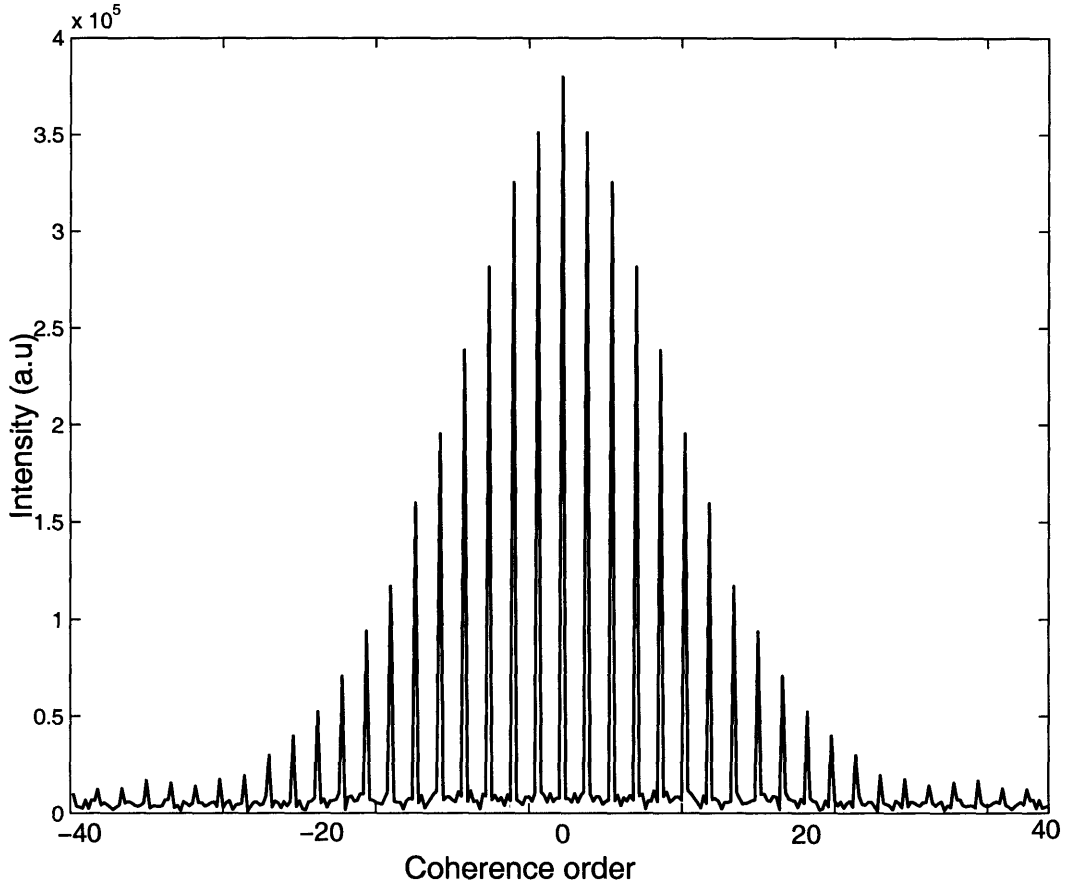

Figure 2-2: A Fourier transformed multiple quantum spectra in a single crystal of CaF_2

to a new picture of many-body spin dynamics in a dipolar coupled solids [29, 30, 31, 32, 33]. These techniques also have been widely used to probe spatial relationships between spins in large macromolecules, polymers, and crystalline systems, including determining the dimensionality and the size of localized, weakly interacting spin clusters. [20, 23, 34, 36, 35]

In this chapter, we introduce a new experimental method and measurements that extend our knowledge of the multiple quantum state by encoding the coherences in two non-commuting bases which are related by similarity transformation.

2.2 Encoding MQC along non-commuting quantizing axes

While the coherences have a physical meaning in the eigenbasis of the system (usually the Zeeman basis), a generalized coherence number reports on the response of the system to any collective rotation of the spins. This is equivalent to expressing the state of the spins in a basis where the apparent axis of quantization is given by the axis of rotation, and can be obtained from the eigenbasis via a similarity transformation. For example, the similarity transform $\mathcal{P}$ connects the density matrices of the system in the two representations (the z and the x bases, for instance).

$$[\rho^x] = \mathcal{P}^{-1}[\rho^z]\mathcal{P}, \tag{2.15}$$

where the elements of the matrices are

$$[\rho^x] =< x_i|\rho|x_j >, \tag{2.16}$$

$$[\rho^z] =< z_i|\rho|z_j >, \tag{2.17}$$

and x_i and z_i are complete sets of basis operators. Under a collective rotation about the x axis, we obtain,

$$< x_i|\exp(-i\phi \sum_i I_x^i)\rho\exp(-i\phi \sum_i I_x^i)|x_j >= \exp(in_x\phi) < x_i|\rho|x_j >, \tag{2.18}$$

where n_x is the x basis coherence number.

Measurements in non-commuting basis are a central task of quantum state tomography. Suter and Pearson previously used a variable flip angle pulse to encode for coherences in the y basis as well as the z basis [37]. In this chapter, we demonstrate an improved technique for the encoding of coherences in the x basis as well as encoding coherences simultaneously in the x and z basis. While the measurement of coherence number in an orthogonal basis does provide more information about the state, it does not yield a direct measure of the spin number, since there is a mixing of coherence orders from different spin states. But measuring multiple quantum coherences in a basis other than the usual z basis is particulary important to study the dynamics of the spin system under a Hamiltonian that conserves z basis coherence number, such as the secular dipolar Hamiltonian.

Table. 2.1 shows the initial state, Hamiltonian, and selection rules for the standard MQ experiment (using double quantum (DQ) Hamiltonian) in both the standard z basis and the x basis using transformation of z basis operators to x basis operator [38],

$$I_z = -\frac{i}{2}(I_x^+ - I_x^-), \tag{2.19}$$

$$I_z^+ = I_x + \frac{i}{2}(I_x^+ + I_x^-), \tag{2.20}$$

$$I_z^- = I_x - \frac{i}{2}(I_x^+ + I_x^-), \tag{2.21}$$

Thus, starting from the initial Zeeman state, we see that under double quantum evolution we obtain even order coherences in the z basis and only odd order coherences in the x basis.

The pulse sequence shown in Fig. 2-3 allows us to encode coherences in the two bases under essentially identical conditions. Fig. 2-3 (a) is a z basis encoding ex-

	z basis	x basis
Initial state	I_z	$\frac{-i}{2}\{I_x^+ - I_x^-\}$
MQ Hamiltonian	$\sum_{i<j} d_{ij}\{I_i^+ I_j^+ + I_i^- I_j^-\}$	$\sum_{i<j} d_{ij}[\{2I_{xi}I_{xj}$ $-1/2(I_{xi}^+ I_{xj}^- + I_{xi}^- I_{xj}^+)\}$ $-1/2\{I_{xi}^+ I_{xj}^+ + I_{xi}^- I_{xj}^-\}]$
Spin number selection rule	± 1	± 1
Coherence number selection rule	± 2	$0,\pm 2$

Table 2.1: MQ experiments in z and x bases

periment and Fig. 2-3 (b) is an x basis encoding experiment. Fig. 2-3 (c) shows the 16-pulse cycle double quantum sequence used. This improved sequence was used to eliminate pulse imperfections and resonance offsets by placing two cycles of standard MQ sequence, phase shifted by π with respect to each other. The two $(\pi/2)$ pulses and Cory 48-time suspension sequence are not required for z basis encoding experiment, but they were inserted to perform the two experiments in identical conditions. In the x basis experiments, the two $(\pi/2)$ pulses perform the basis transformation and the phase encoding of the coherences by progressively incrementing the phase of the first $(\pi/2)$ pulse. A Cory 48-pulse sequence was placed to prevent any unwanted switching transients when $(\pi/2)$ pulses are put back to back, and the Cory 48-pulse sequence prevents evolution under the secular dipolar Hamiltonian between two $(\pi/2)$ pulses [40]. The operator corresponding to the observable signal is I_z. The measured signal for experiments in Fig. 2-3 (a) corresponds to $< I_z >_\phi = Tr[\rho_f I_z]$, where the final density matrix is given by

$$\begin{aligned} \rho_f &= U_{DQ}^\dagger R_y(-\pi/2)R_y(\pi/2)U_{DQ}\rho_i U_{DQ}^\dagger R_y(-\pi/2)R_y(\pi/2)U_{DQ} \\ &= U_{DQ}^\dagger R_z(-\phi)U_{DQ} I_z U_{DQ}^\dagger R_z(\phi)U_{DQ}, \end{aligned} \tag{2.22}$$

where we defined $R_a(\phi) = e(i\phi I_a)$. If we define $\rho_s = U_{DQ} I_z U_{DQ}^\dagger$, then the measured signal in z basis experiment becomes

$$< I_z >_\phi = Tr[\rho_f I_z] = Tr[R_z(-\phi)\rho_s R_z(\phi)\rho_s]. \tag{2.23}$$

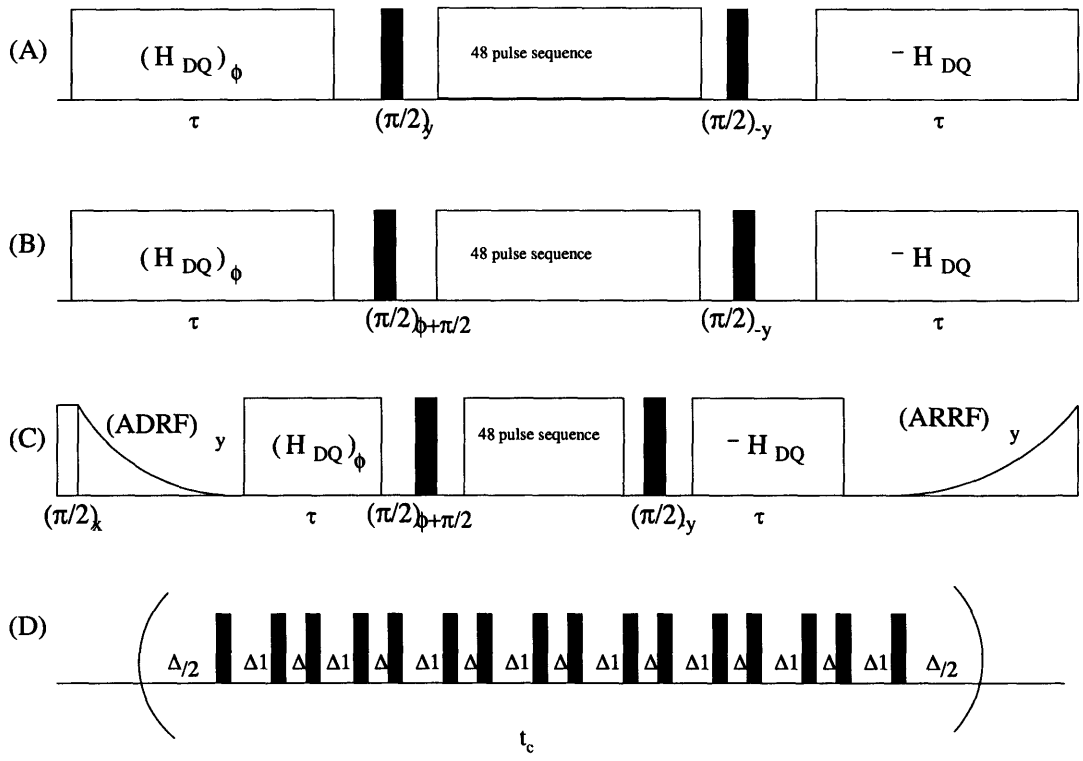

Figure 2-3: Pulse sequences for encoding multiple quantum coherences in non-commuting bases

For the experiment in Fig. 2-3 (b), it can be shown that the final density matrix is given by,

$$\begin{aligned}\rho_f &= U_{DQ}^{\dagger} R_y(-\pi/2) R_z(-\phi) R_y(\pi/2) U_{DQ} \rho_i U_{DQ}^{\dagger} R_y(-\pi/2) R_z(\phi) R_y(\pi/2) U_{DQ} \\ &= U_{DQ}^{\dagger} R_x(-\phi) U I_z U^{\dagger} R_x(\phi) U. \end{aligned} \tag{2.24}$$

Accordingly, observed magnetization in the x basis experiment is similarly

$$< I_z >_{\phi} = Tr[\rho_f I_z] = Tr[R_x(-\phi)\rho_s R_x(\phi)\rho_s]. \tag{2.25}$$

In both cases, ϕ is uniformly sampled out to a multiple of 2π and resulting data are Fourier transformed with respect to ϕ to obtain a coherence number distribution.

2.3 Experimental results

The experiments were performed at room temperature at 2.35 T (94.2 MHz, ^{19}F), using a BRUKER Avance spectrometer and home built probe. The samples used were a 1 mm^3 single crystal of CaF_2 with $T_1 \sim 7$ s. A 0.51 μs $\pi/2$ was used, and the pulse spacing Δ in the double quantum sequence was set to 1.3 μs. The cycle time was determined to be 43.4 μs. The pulse spacing in the 48-pulse sequence was set to 1.5 μs.

2.3.1 Z and X basis encoding

Fig. 2-4 shows the experimental results obtained for z and x basis encoding experiment, using the pulse sequence depicted by Fig. 2-3 (a) and Fig. 2-3 (b) respectively. The phase (ϕ) was incremented from 0 to 8π with $\Delta\phi = \frac{\pi}{32}$ to encode up to 32 quantum coherences for every experiment. A fixed time point corresponding to maximum intensity signal was sampled for each ϕ value and Fourier transformed with respect to ϕ to obtain the coherence order distribution at the given double quantum evolution time, which is τ. Clear even and odd selectivity was obtained, which was described

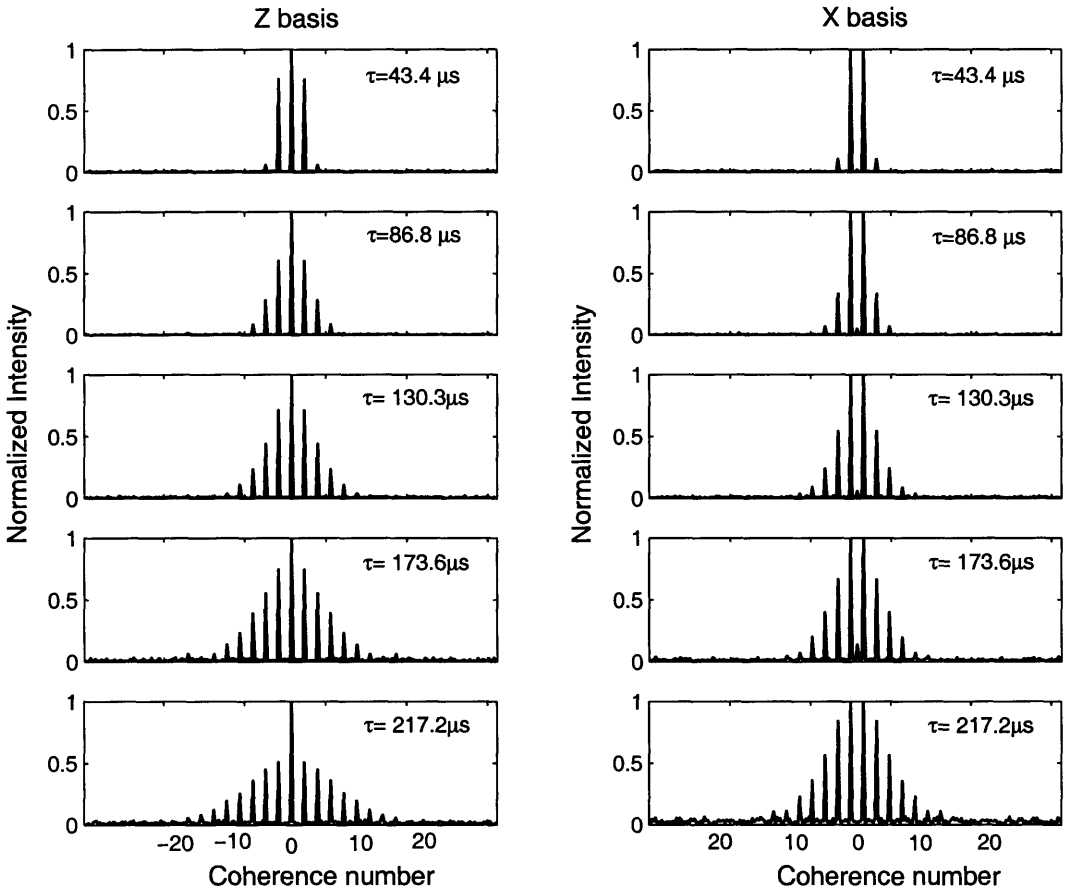

Figure 2-4: Z and X bases coherence number encoding experiments for $1-5$ loops of 16-pulse double quantum cycles. Clear odd and even selectivity in coherence number distribution is shown.

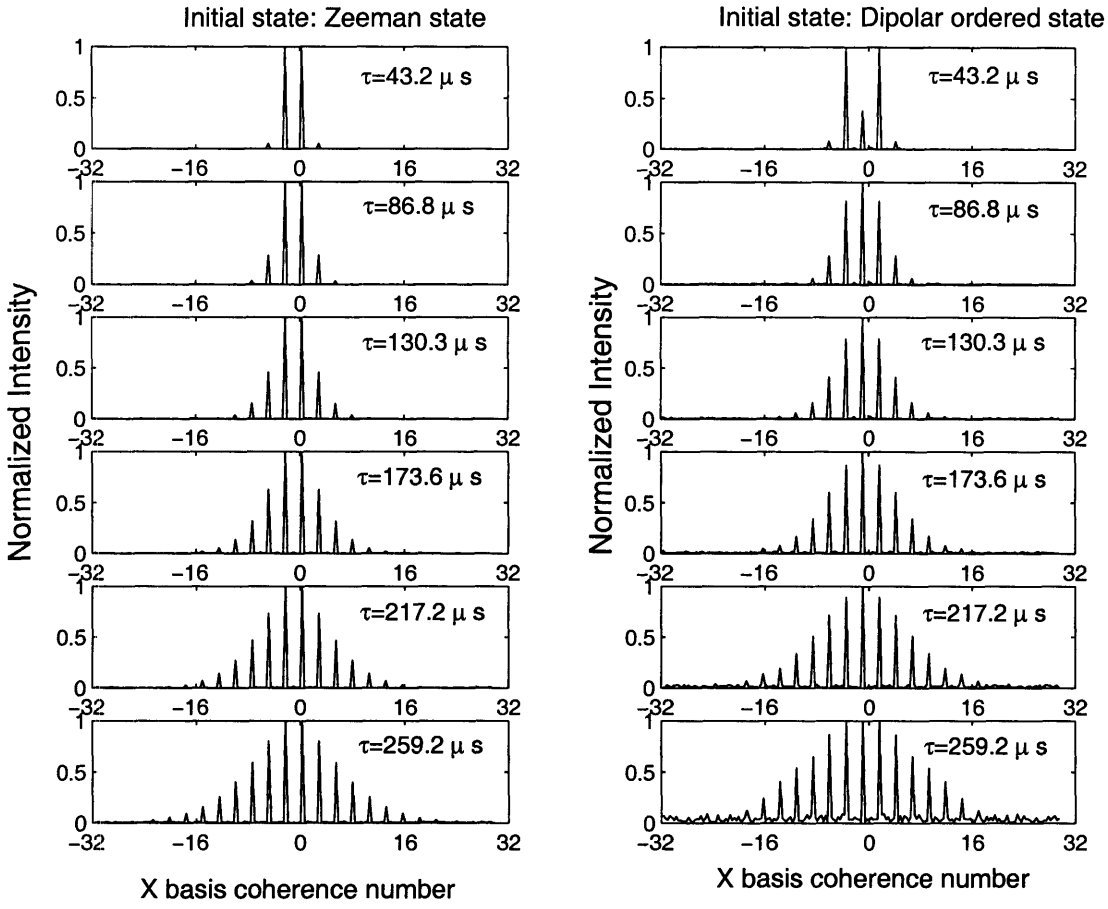

Figure 2-5: X basis coherence number distribution as a function of evolution time under the double quantum Hamiltonian. Data show clear even and odd selectivity depending on initial state preparation.

in the previous sections, and higher order coherences are created as double quantum evolution time (τ) increases as the number of loops of 16-pulse double quantum cycle increases.

Narrower distribution of x basis coherence number distribution can be understood from the selection rules of double quantum Hamiltonian in two different bases. In the z basis, the coherence number is forced to change by ± 2, while in the x basis, existence of zero quantum terms can slow down the coherence number growth.

2.3.2 X basis encoding for different initial states

The study of the evolution of different initial states under the secular dipolar Hamiltonian has been a subject of interest as it provides a well-posed problem in many-body dynamics with the well-known system Hamiltonian. Recently spin diffusion measurements of both initial states have been performed showing unexpected fast diffusion constants for dipolar-ordered state [8, 9]. The Zeeman order state contains only single spin population term, while dipolar ordered state consists of correlated two spin states, and it is suggested that this fast diffusion constant of the dipolar-ordered state was a consequence of constructive quantum interference effect [9].

Fig. 2-5 shows the development of higher order coherences under double quantum Hamiltonian for two different initial states, Zeeman order and dipolar-ordered states. We used the x basis encoding technique to monitor the evolution of the spin system for both initial states under double quantum Hamiltonian. Clear even and odd selectivity was maintained up to experimentally probed time scales, which is the result of coherence number selection rule originating from different initial states under the evolution of the same Hamiltonian. Fig. 2-6 shows the effective spin cluster size, estimated using conventional Gaussian fit method for both Zeeman and dipolar-ordered state under the double quantum evolution [27]. Effective cluster sizes ($< N >$) are seen to follow t^3 curve and were fit using Eq. (2.26).

$$< N >= At^3 + B. \tag{2.26}$$

It is observed that the rate of growth of the dipolar-ordered state is faster than that of the Zeeman state under the double quantum evolution with Gaussian estimation ($A_{\text{dipolar}}/A_{\text{zeeman}} \sim 1.64$). This experiment does not provide unique information regarding the dynamics of spin diffusion processes, but demonstrates the fact that the initial state information is kept in the coherent evolution of the spin system under dipolar interaction in a rigid lattice of nuclear spins. Additionally, the growth rate of spin cluster size are seen to depend on the initial state preparation, which might provide useful information for understanding unexpectedly fast spin diffusion process

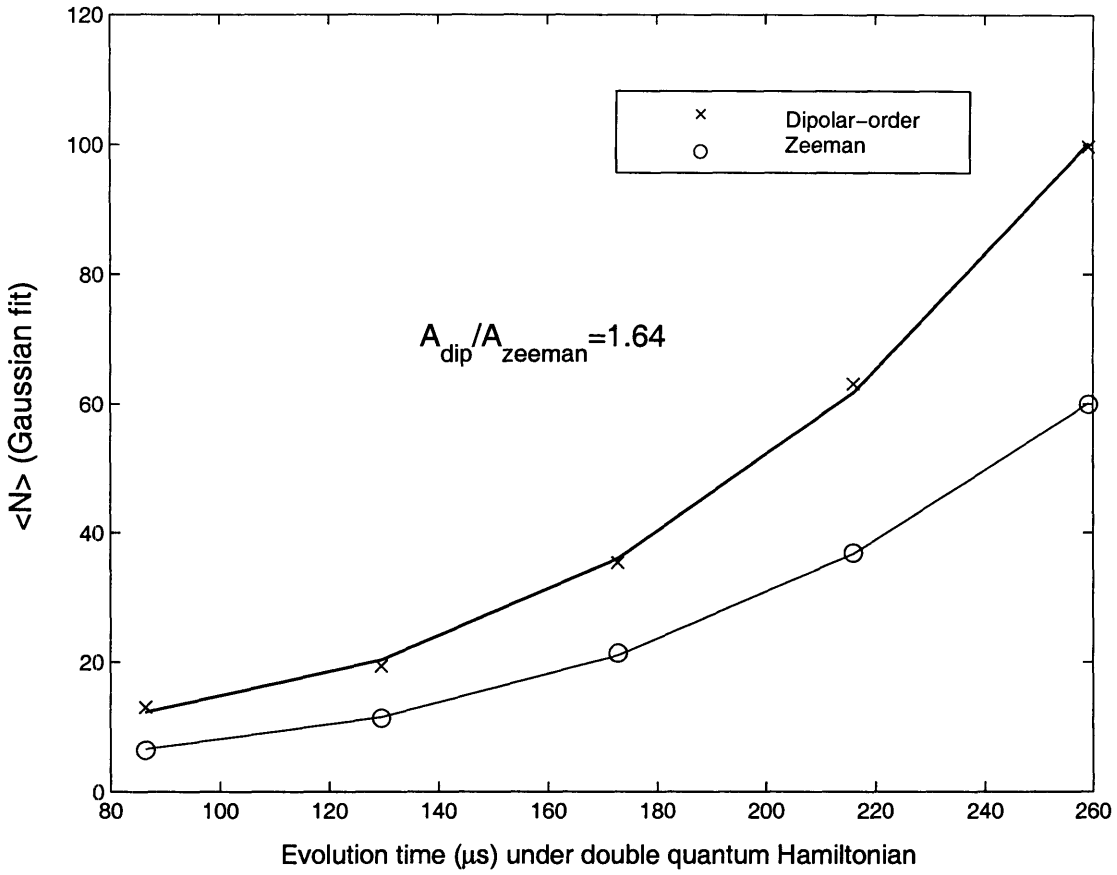

Figure 2-6: Estimated spin cluster sizes ($< N >$) for different initial states, Zeeman and dipolar-ordered state. Solid lines are fits to Eq. (2.26).

for dipolar-ordered state.

2.3.3 Two dimensional correlation experiment between Z and X bases

The correlation between x and z basis coherence numbers can be experimentally probed by using 2D experiment. The 2D experiment can be performed by progressively incrementing the phases of refocusing double quantum Hamiltonian ($U_{DQ}^{\dagger}$) by ζ independent of ϕ. The measured data in the 2D experiment is given by,

$$< I_z >_{\phi\zeta} = Tr[R_z(-\zeta)R_x(-\phi)\rho_s R_x(\phi)R_z(\zeta)\rho_s]. \tag{2.27}$$

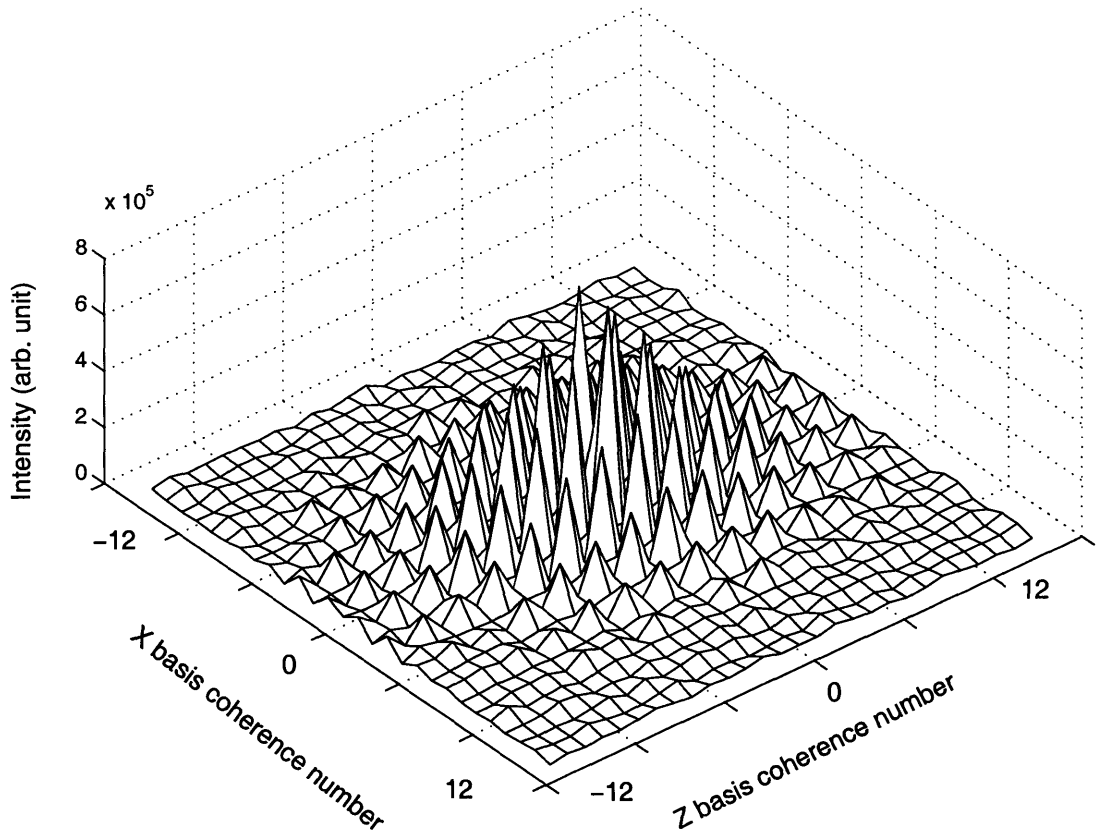

Figure 2-7: The result of 2D correlation experiments. The width in z basis coherence number distribution appears to be broader than that of x basis.

The phases of ϕ and ζ are independently incremented to sample a rectangular grid and a 2D Fourier transformation is performed to obtain coherence distribution along x and z bases at the same time.

Fig. 2-7 shows 2D correlation experiments. We used $\tau = 130.3\ \mu s$ corresponding to 3 loops of 16-pulse cycles, and $\Delta\phi$ and $\Delta\zeta$ were set to $2\pi/28$ to encode up to 14 coherence orders in each bases. The phases were incremented up to 2π along each axis, resulting in a 28x28 grid, and this grid was 2D Fourier transformed to yield Fig. 2-7. The width of the z basis coherence number distribution was seen to be larger than that of the x basis.

2.4 Conclusion

We have shown that by encoding MQ coherences in the non-commuting bases, it is possible to extract additional information about the spin system. It will be shown in the following chapters that the x basis encoding method can be used to estimate the state of the spin system where z basis encoding does not provide any information.

Chapter 3

Spin counting experiment in dipolar-ordered state

3.1 Introduction

[1] Dipolar-ordered states are eigenstates of spin Hamiltonian, and hence are constants of the motion. In the strong magnetic field, Zeeman and dipolar-ordered states are independently conserved quantities and decay on a time scale of T_1 and T_{1D} respectively as the spin system interacts with the external environment or lattice. The dipolar-ordered state can be prepared from a state of Zeeman equilibrium at high field by adiabatically removing the Zeeman field [41, 42]. It is also possible to produce the dipolar- ordered state in the rotating frame using two well known methods: adiabatic demagnetization in the rotating frame (ADRF) and the Jeener-Broekaert (JB) sequence [44]. While the spin system is in the dipolar-ordered state at the end of ADRF process (by definition), following a JB pulse pair the spin system is in a transit state, and only evolves into the dipolar-ordered state on a time scale of the order of T_2. Emid *et al.* have shown that the spin system contains multiple quantum coherences immediately after the second pulse [46, 47, 48].

Recently, direct measurement and comparison of spin diffusion rates of the Zee-

[1] This chapter was drawn from sections of [12] with contribution from Dr. Chandrasekhar Ramanathan.

man and the dipolar-ordered states have been made available by NMR incoherent scattering method using strong gradient fields [8, 9]. The diffusion constant for the Zeeman ordered state is shown to agree well with existing theories and simulation results, while experimental measurement of spin diffusion rate for the dipolar-ordered state shows a large discrepancy with existing theories. The Zeeman ordered state consists of single-spin population terms only, while the dipolar-ordered state ($\rho \sim H_d$) is expected to contain correlated two spin terms because dipolar Hamiltonian contains bilinear interactions. It is suggested that the constructive interference in the transport of the two-spin state is responsible for this enhancement in spin diffusion rate of the dipolar-ordered state. Further analysis of above problem requires exact knowledge on the nature of dipolar-ordered state that is experimentally created either in ADRF or JB methods.

In this chapter, we utilize coherence number encoding technique explained in the previous chapter to experimentally investigate the nature of the dipolar-ordered state prepared using these two methods. We also explore the transient response of the spin system following a JB pulse pair and its evolution into the dipolar-ordered state.

Conventional Multiple Quantum (MQ) Nuclear Magnetic Resonance (NMR) techniques in solids have been generally used to study the size of the localized spin clusters as well as to explore many body dynamics of solid state nuclear spins. However, these standard techniques are of limited utility in the study of the dipolar-ordered state, as the state is not encoded by usual MQ techniques. We measure the coherence numbers of the dipolar-ordered state in both the x and z bases, by observing the response of the system to a collective rotation of the spins about the appropriate axis, and use this information to reconstruct the dipolar-ordered state [10].

	Secular Dipolar Hamiltonian	Coherence number
z basis	$\sum_{j<k} D_{jk}\{\hat{I}_{zj}\hat{I}_{zk} - \frac{1}{4}(\hat{I}_{zj+}\hat{I}_{zk-} + \hat{I}_{zj-}\hat{I}_{zk+})\}$	0
x basis	$-\frac{1}{2}\sum_{j<k} D_{jk}\{\hat{I}_{xj}\hat{I}_{xk} - \frac{1}{4}(\hat{I}_{xj+}\hat{I}_{xk-} + \hat{I}_{xj-}\hat{I}_{xk+})\}$	0,± 2
	$-\frac{3}{8}\sum_{j<k} D_{jk}\{\hat{I}_{xj+}\hat{I}_{xk+} + \hat{I}_{xj-}\hat{I}_{xk-})\}$	

Table 3.1: Coherence numbers of the secular dipolar Hamiltonian in the z and x bases

3.2 Theory

In the dipolar-ordered state the density operator of the spin system should correspond to the dipolar Hamiltonian. In the high temperature approximation,

$$\rho_D = \frac{exp(-H_D/kT_s)}{Z} \simeq \frac{1}{Z}(\mathbf{1} - \frac{H_D}{kT_s}) \tag{3.1}$$

$$Z = \mathrm{Tr}\{\exp(-H_D/kT_s)\}, \tag{3.2}$$

where

$$\hat{H}_D = \sum_{j<k} D_{jk}\left\{\hat{I}_{jz}\hat{I}_{kz} - \frac{1}{4}(\hat{I}_{j+}\hat{I}_{k-} + \hat{I}_{j-}\hat{I}_{k+})\right\}, \tag{3.3}$$

$$D_{jk} = \frac{\gamma^2\hbar^2}{r_{jk}^3}(1 - 3\cos^2\theta_{jk}). \tag{3.4}$$

H_D is secular dipolar Hamiltonian, T_s is the spin temperature, γ is the gyromagnetic ratio, r_{jk} is the distance between spins j and k, and θ_{jk} is the angle between the external magnetic field and internuclear vector $\vec{r}_{jk}$. As the dipolar-ordered state only contains population and zero quantum terms in the z basis, its structure cannot be revealed by z basis encoding.

While z basis encoding is not useful, x basis encoding technique developed in the previous chapter can be used to yield Table. 3.1 showing the structure of secular dipolar Hamiltonian in both z and x bases and coherence numbers in each basis.

The presence of both zero and double quantum terms in the x basis representation provides additional observable information about the state of the spin system.

3.3 Creation of dipolar-ordered state

3.3.1 Adiabatic demagnetization in rotating frame

Experimental methods for creating the dipolar-ordered state using adiabatic demagnetizing fields in the rotating frame were shown by Slichter and Holton, and Anderson and Hartmann extending Redfield's concept of spin temperature to the spin system in a rotating reference frame [41, 42, 43]. Adiabatic process represents the slowness of change in time in such a way that the changes are reversible, and the entropy of the system remains constant during the process.

In the ADRF experiment, a $\pi/2$ pulse is applied onto the spin system in thermal equilibrium under static Zeeman field, followed by a phase shifted adiabatically decreasing RF field whose initial intensity is larger than that of the local dipolar fields. The density matrix of the spin system in the rotating reference frame with respect to Zeeman field during the RF irradiation can be written as

$$\hat{\rho} = \frac{e^{-(H_{rf}+H_D)/kT_s}}{Z}, \tag{3.5}$$

where T_s is the spin temperature and can be given by

$$\frac{T_s}{(B_{rf}^2 + B_d^2)} = \frac{T}{(B_o^2 + B_d^2)}, \tag{3.6}$$

assuming that the changes in the RF field are made so slowly that the total entropy of the system remains constant. B_{rf} is the RF field strength, B_o is the strength of the Zeeman field and B_d is the strength of local dipolar fields. When the RF field is made zero, then spin temperature becomes $T_s = TB_d/B_o$ $(B_o >> B_d)$ and the resulting density matrix can be given by

$$\hat{\rho} = \frac{e^{-(H_D)/kT_s}}{Z}, \tag{3.7}$$

which is the dipolar-ordered state.

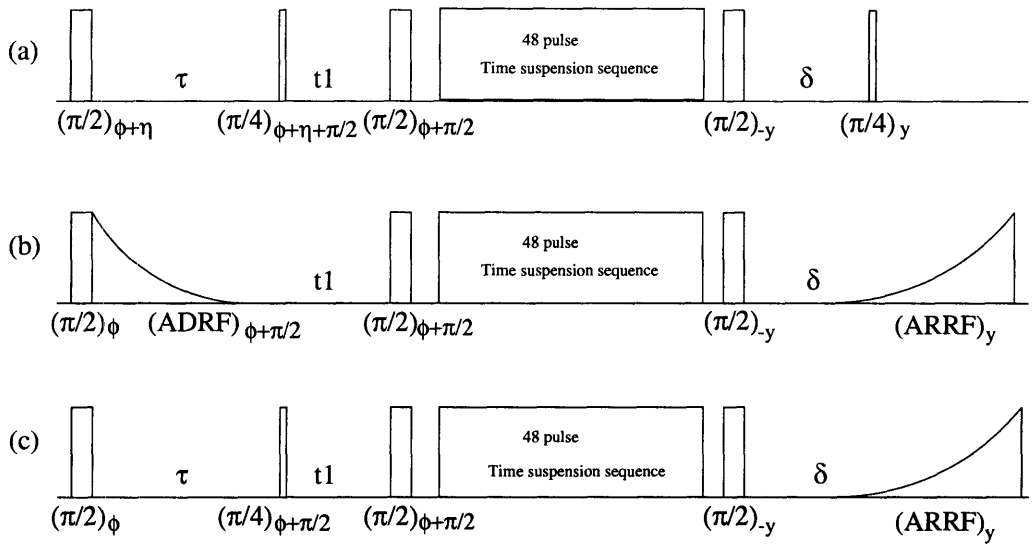

Figure 3-1: Pulse sequences for z and x bases encoding of the dipolar-ordered state. (a) Jeener-Broekaert and 45° pulse readout for simultaneous z and x basis encoding. (b) ADRF creation and ARRF readout for x basis encoding. (c) JB creation and ARRF readout for x basis encoding. The 48-pulse sequence was used to suppress the evolution of the internal Hamiltonian between the two $\pi/2$ pulses. We assume that relaxation effects are negligible during one cycle of this sequence.

3.3.2 Jeener -Broekaert two pulse method

A two pulse method creating the dipolar-ordered state is introduced by Jeener and Broekaert [44, 45]. Even though it's efficiency is lower than that of adiabatic demagnetization, this method is practically suitable for the study of fast phenomena, such as the very fast relaxation of dipolar energy, or the dynamical evolution of spin system to the dipolar order.

3.4 Experimental results

The pulse sequence used in the various experiments are shown in Figs. 3-1 (a)- 3-1 (c). The phases (ϕ) were incremented from zero to 4π with $\Delta\phi = \pi/8$ to encode up to 8 quantum coherences in every experiment. A fixed time point, corresponding to a maximum intensity signal in the echo, was sampled for each value of ϕ and the data was Fourier transformed with respect to ϕ to create the coherence numbers.

3.4.1 State estimation of the dipolar-ordered state

In order to estimate the state of the system, the two dimensional coherence encoding experiment shown in Fig. 3-1 (a) was performed. By incrementing the phases ϕ and η independently, it is possible to simultaneously encode the system in both the z and x bases, and observe correlations between them. The pulse spacing (τ) in the JB sequence was set to 13 μs, and t_1 was set to 1 ms. It is assumed that all transients have decayed away by this time. The 48-pulse sequence is used to suppress evolution of the internal Hamiltonian between the $\pi/2$ pulses in the x basis experiment. The spacing between the pulses in the sequence was set to 1.5 μs. The delay δ was set to 20 μs. Fig. 3-2 shows the coherences observed for the dipolar-ordered state in a 2D experiment where the coherences in the two bases are correlated. The dipolar-ordered state is observed to contain zero quantum coherence terms in the z basis, and zero and double quantum terms in the x basis. The highest coherence order observed was ± 2 in the x basis experiment. The absence of single quantum order in the x basis data illustrates the symmetry of the state under exchange of two spins. Given the axial symmetry of the secular dipolar Hamiltonian, a generic two spin zero quantum state is

$$\rho = \sum_{i<j} \left\{ a_{ij} I_z^i I_z^j + b_{ij} (I_z^{i+} I_z^{i-} + I_z^{i-} I_z^{i+}) \right\}. \tag{3.8}$$

Transforming this state to the x basis yields

$$\rho = \sum_{i<j} \left\{ \frac{1}{4}(-a_{ij} + 2b_{ij})(I_x^{i+} I_x^{i+} + I_x^{i-} I_x^{i-}) + 2b_{ij} I_x I_x + \frac{1}{4}(a_{ij} + 2b_{ij})(I_x^{i+} I_x^{i-} + I_x^{i-} I_x^{i+}) \right\}. \tag{3.9}$$

We expect the +2 and -2 coherences to have the same intensity, and the ratio of the double quantum coherence to the zero quantum coherence to be

$$R = \frac{-a_{ij} + 2b_{ij}}{6b_{ij} + 2a_{ij}}. \tag{3.10}$$

We performed one dimensional x basis encoding experiments in order to measure the ratio between the zero and double quantum terms, following the ADRF and JB

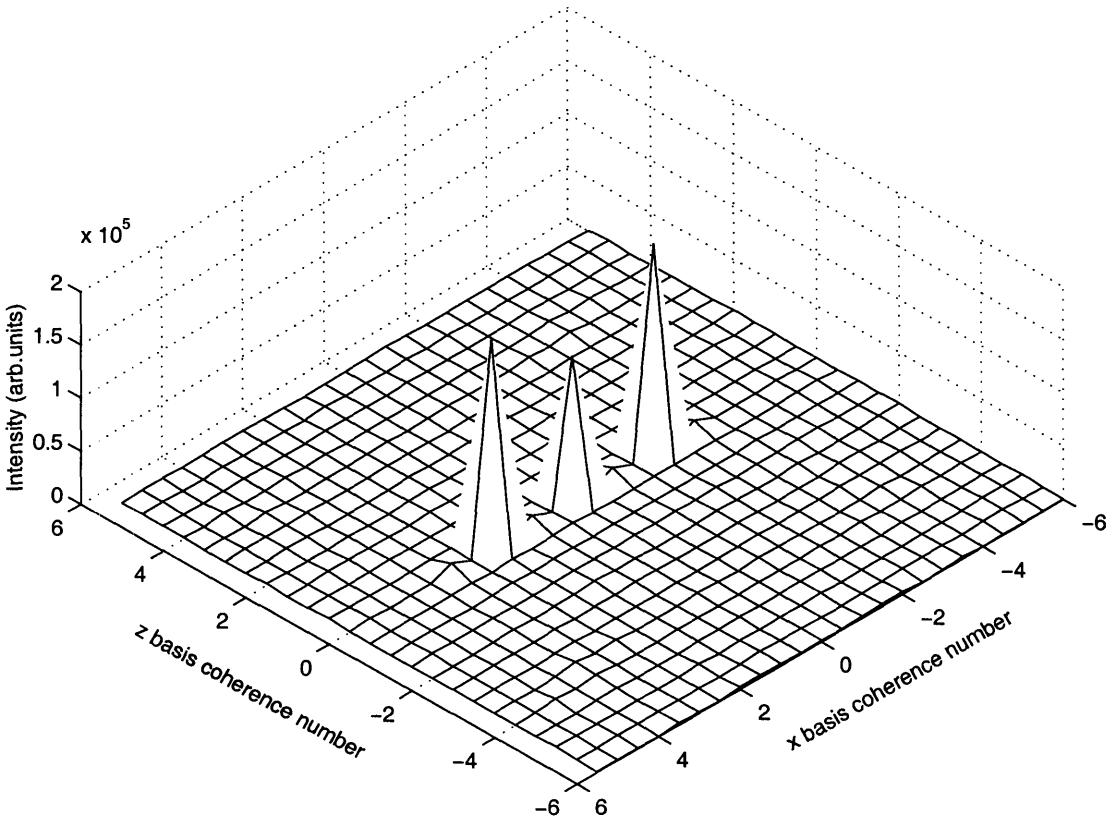

Figure 3-2: Results of the correlated 2D experiment that simultaneously encodes z and x bases coherence for the dipolar-ordered state. The dipolar-ordered state is observed to contain only zero quantum in the z basis, and both zero and double quantum coherences in the x basis.

sequences. The pulse sequences for this experiment are shown in Figs. 3-1 (b) and 3-1 (c). Adiabatic remagnetization in the rotating frame (ARRF) was used to refocus the state in both cases in these experiments, in order to ensure that the full dipolar state was refocused.

The pulse spacing (τ) in the JB sequence was set to 13 μs, and t_1 varied from 1 ms to 5 s. A 3 ms long hyperbolic secant pulse, corresponding to an adiabatic half passage of the amplitude, was used for both the ADRF (decreasing amplitude) and ARRF (increasing amplitude). A delay of 20 μs was inserted before the ARRF to minimize transient effects. Fig. 3-3 shows the experimentally obtained ratio using both JB and ADRF sequences as a function of t_1. While the dipolar-ordered state decays with time constant of T_{1D}, the ratio between the two coherences remains constant at 1.5 in both cases. When this is set equal to R, we get $a_{ij} = -4b_{ij}$, indicating that the state measured is

$$\rho = \sum_{i<j} a_{ij} \left\{ I_z^i I_z^j - \frac{1}{4}(I_z^{i+} I_z^{i-} + I_z^{i-} I_z^{i+}) \right\}. \tag{3.11}$$

3.4.2 Zeeman contamination in T_{1D} measurement

T_{1D} measurements are done exclusively on resonance in order to avoid possible contamination of the data by encoded Zeeman magnetization. However, it can be difficult to be simultaneously on the exact resonance condition in strongly coupled dipolar solids such as single crystal CaF_2, and impossible to be simultaneously on resonance everywhere in powder sample. Emid *et al.* designed an offset-independent method to measure dipolar relaxation times, by summing the results of two experiments using $\pi/4$ and a $-3\pi/4$ pulse to convert dipolar order back to Zeeman order [46, 47]. The difference in pulse lengths can be a problem in strongly coupled dipolar systems, as the evolution under a long pulse becomes non-negligible. In the x basis measurements presented here, the Zeeman term ($\sum_i I_z^i$) is encoded into single quantum coherence while the dipolar-ordered state is encoded into zero and double quantum coherence. Fig. 3-4 shows the x basis coherences measured following a JB pulse pair (Fig. 3-2 (c)) when the experiment is performed on and off resonance by 21 kHz.

This clean separation of the two terms allows very accurate T_{1D} measurement,

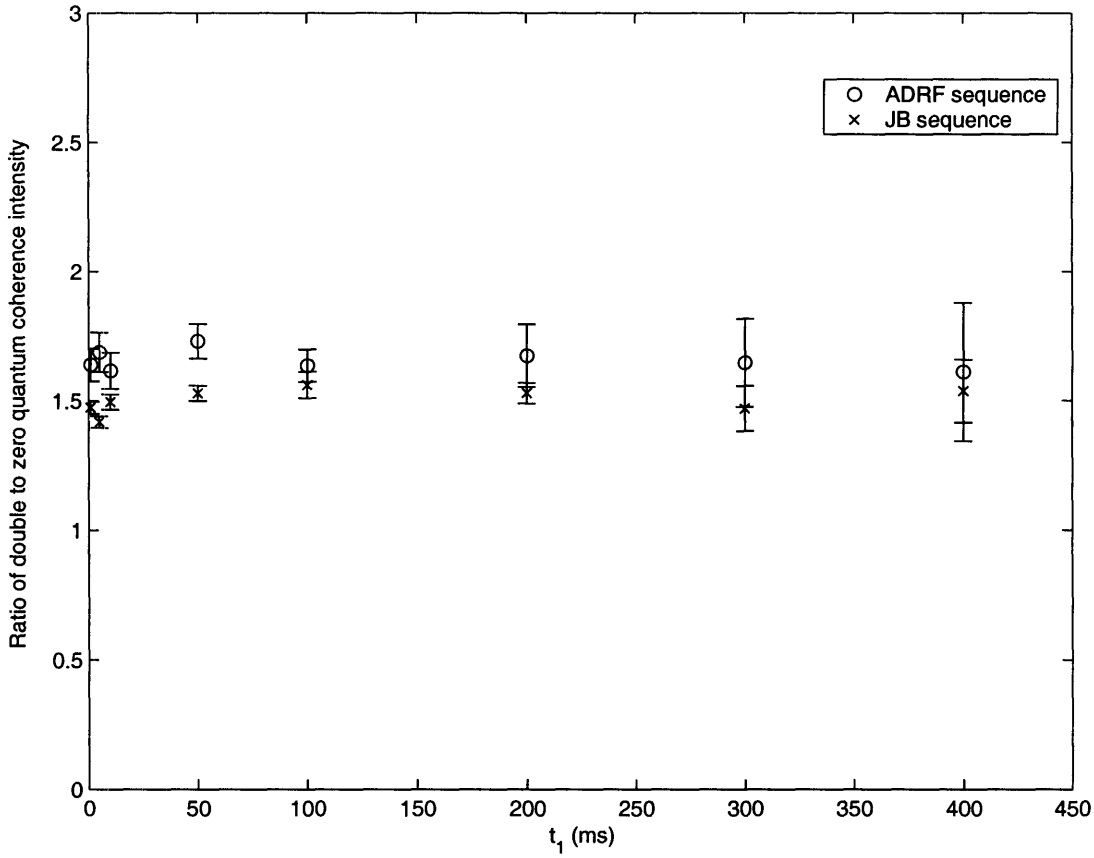

Figure 3-3: Ratio between x basis double and zero quantum signals as a function of t_1. As the dipolar-ordered state decays, the intensity of the double and zero quantum orders decay. However, the ratio is maintained at ~ 1.5. The errors were estimated from the variance of the noise in a signal free region of the spectrum. The increase in the error with longer evolution time is due to the deteriorating signal to noise ratio as the signal decays.

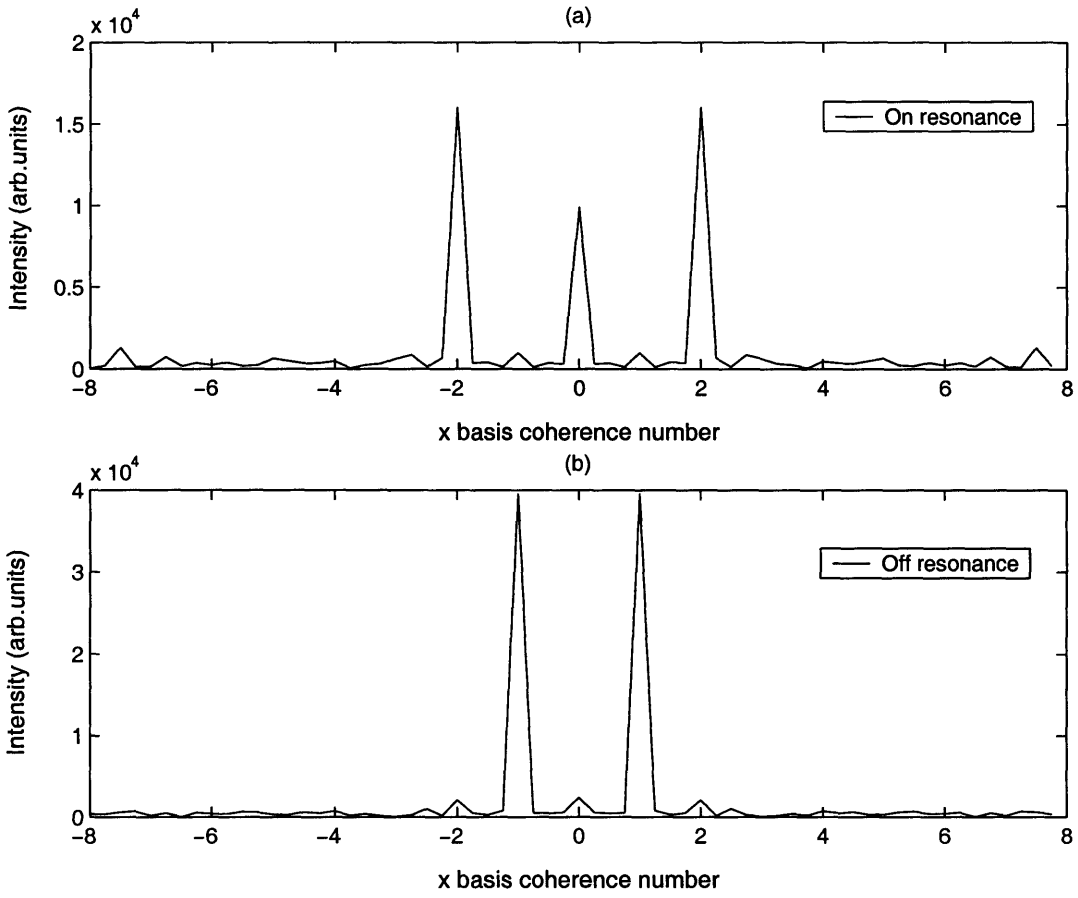

Figure 3-4: A pulse sequence in Fig. 3-1 was used to encode the x basis coherences (a) on resonance, and (b) 21 kHz off resonance. t_1 was set to 5 ms in both experiment.

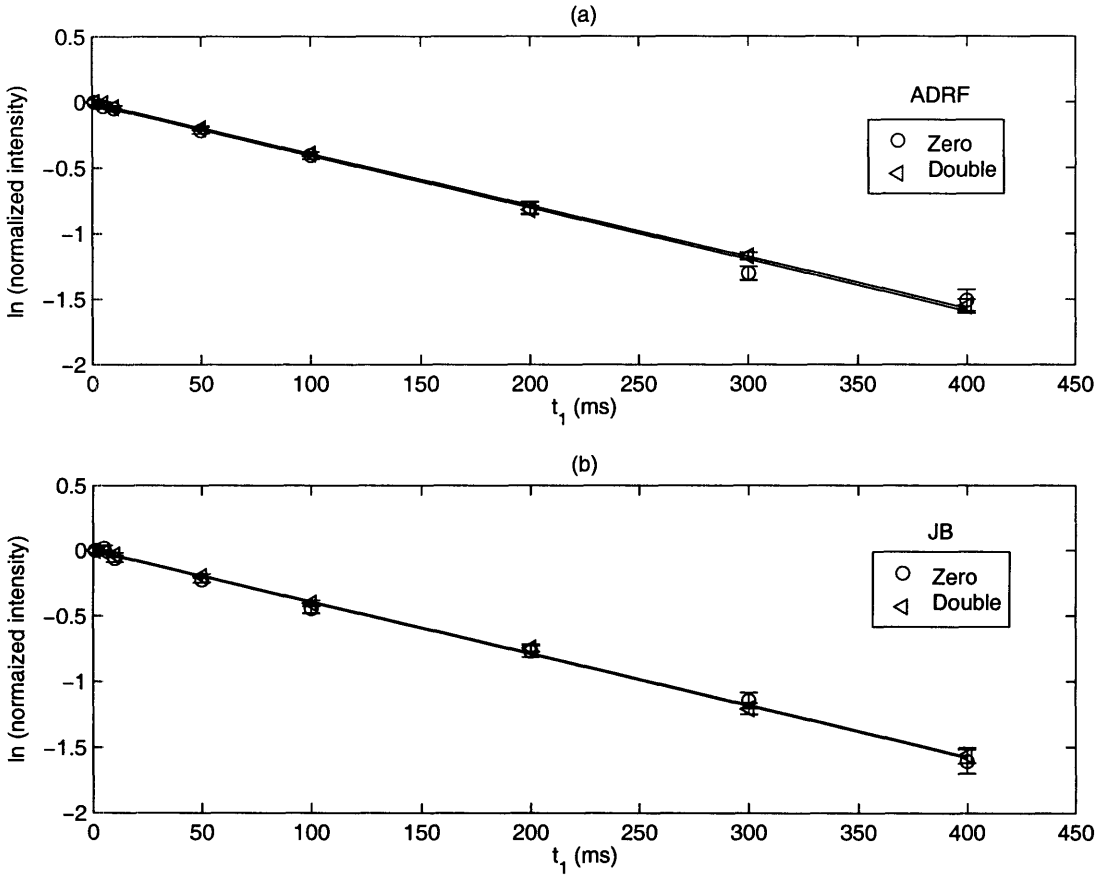

Figure 3-5: Decay of x basis double and zero quantum signals in the (a) ADRF and (b) JB experiments. The measured decay constant was 255 ± 3.1 ms and 254 ± 3.1 ms for the zero and double quantum terms, respectively, in the ADRF experiment, and 254 ± 2.9 ms for both zero and double in the JB experiments.

without any T_1 contamination. Fig. 3-5 shows the relaxation data for dipolar-ordered state created by JB and ADRF methods. The measured T_{1D} was essentially identical for the zero and double quantum x basis coherences in both sets of experiments (255 ± 3.1 ms and 254 ± 3.1 ms for the zero and double quantum terms, respectively, in the ADRF experiment, and 254 ± 2.9 ms for both zero and double in the JB experiment) as expected, as dipolar relaxation should not depend on the method used to create the state. The pulse sequences in Figs. 3-1 (b)- 3-1 (c) were used. The $\pi/2$ pulse was 1.5 μs and a 4 ms hyperbolic secant pulse was used for the ADRF and ARRF (decaying and growing respectively).

3.4.3 Initial transient for Jeener-Broekaert sequence

Emid *et al.* have previously shown that multiple quantum coherences are contained in the transverse magnetization following the JB sequence [46, 47, 48]. By performing the JB experiment off-resonance they were able to detect the presence of single, double, and triple quantum coherences during the initial transient regime following the $\pi/4$ pulse. Using a combination of JB experiments with different phases, they were also able to selectively observe the even and odd coherences in this initial transient regime as well as in a sample of l-alanine powder. Their experimental data showed that the evolution of the transients die out about 60 μs.

We used the pulse sequence in Fig. 3-1 (a) to study the transient response of the spin system following a JB pulse pair, and the evolution of the system to a state of dipolar order. Fig. 3-6 shows the transient response of the spin system following a JB sequence, for a single crystal of calcium fluoride oriented along the [110] direction with respect to the external field (the crystal was actually between [110] and [111] directions). Immediately after the $\pi/4$ pulse, the largest intensity is present in the $z = 0, x = \pm 2$ term, but zero, single, and double quantum z basis terms correlated to zero, single, double, and even a few triple quantum x basis contributions are observed. As the spin system evolves under the secular dipolar Hamiltonian, the coherence distribution appears to expand in the x basis and contract in the z basis. This is expected as the Hamiltonian is zero quantum selective in the z basis, and contains both zero and double quantum selective in the x basis. The intensity of the triple quantum grows, indicating the presence of three spin terms. The presence of four spin terms have also been observed albeit at low intensity. These coherences then decay and around 100 μs, the system appears to have reached the dipolar-ordered state in the JB experiment.

Figs. 3-7 (a) and 3-7 (b) show the FIDs measured for a single crystal of calcium fluoride at two orientations, (a) the [100] direction and (b) the [110] direction. Figs. 3-7 (c) and 3-7 (d) show the projection of the measured 2D data onto the z axis for the two orientations, and Figs. 3-7 (e) and 3-7 (f) show the corresponding projection in

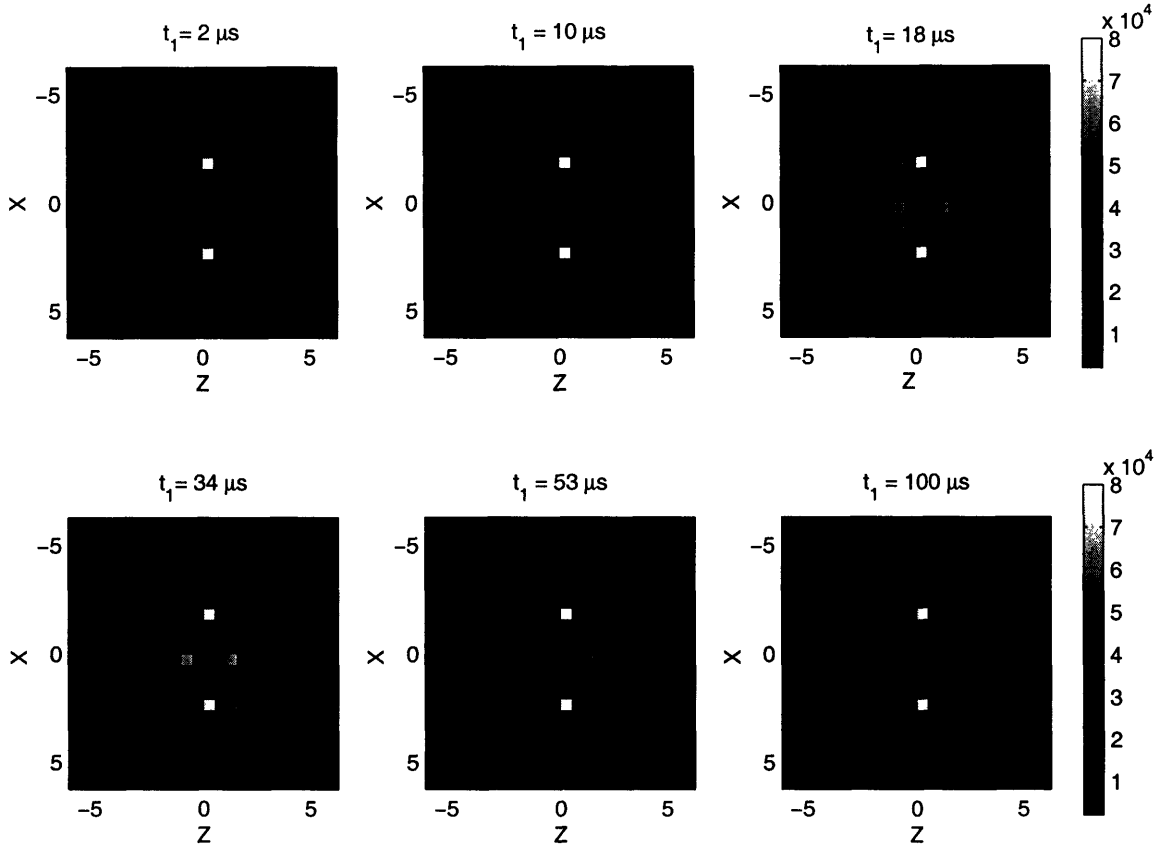

Figure 3-6: Results of the 2D correlated x and z bases coherence number measurements illustrating the dynamical evolution of the spin system following a JB pulse pair, and the approach of the system to the dipolar-ordered state when the crystal is aligned along [110] direction.

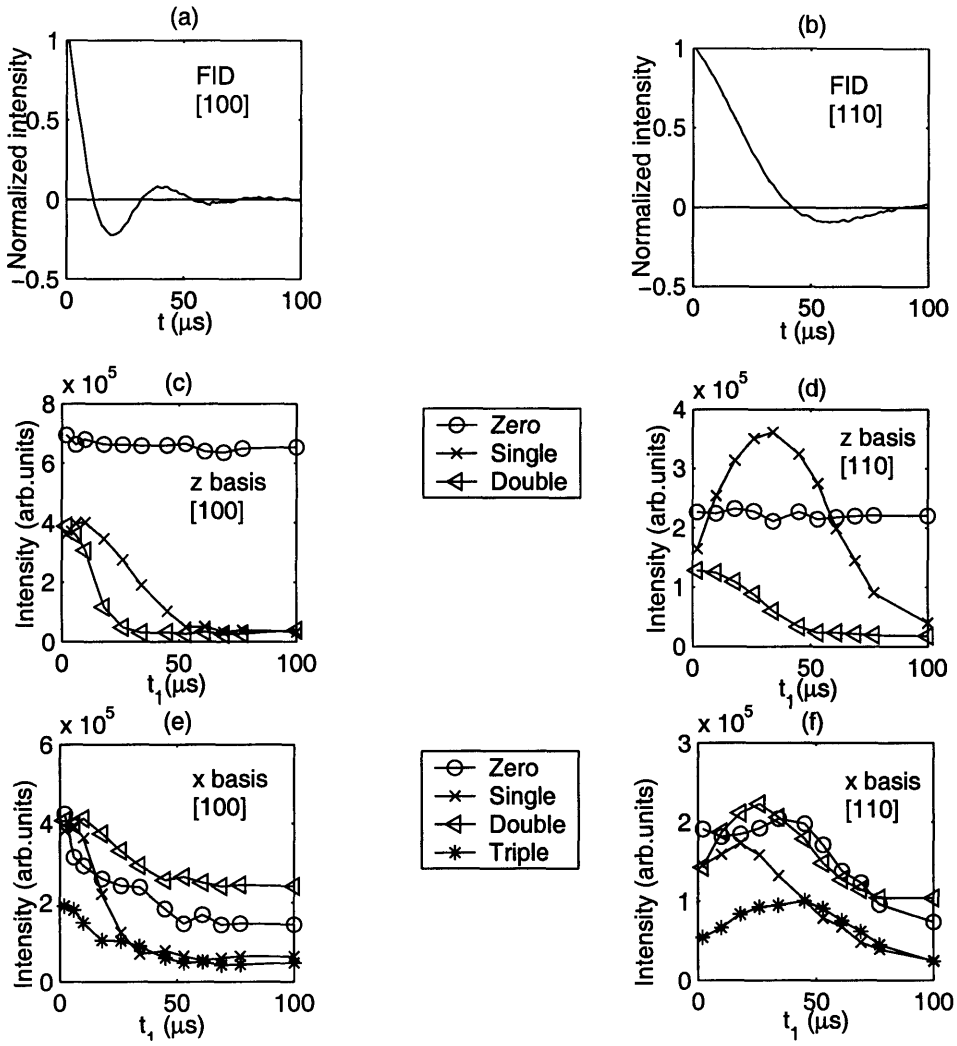

Figure 3-7: (a) FID measured when the crystal is aligned along the [100] direction and (b) [110] direction. (c) Evolution of the z basis coherences obtained by projecting the two-dimensional data onto the appropriate axis for the [100] and (d) [110] directions. (e) Evolution of the x basis coherences obtained by projecting the two dimensional data onto the appropriate axis for [100] and (f) [110] directions. As the data shown is the sum of the absolute values of the different coherences, the nonequilibrium curves do not go to zero.

the x axis. When the crystal is aligned along the [110] direction, the dipolar couplings between the nearest-neighbor fluorine spins become small. In the z basis, the double quantum term is seen to decay while the single quantum term initially grows, reaches a maximum around 30 μs and then decays. The intensity of the zero quantum term is seen to peak around 20 μs and the triple quantum term to peak around 45 μs, while the zero and double quantum terms are seen to oscillate before settling down to constant values. The dipolar-ordered state appears to be created after approximately 100 μs. When the crystal is oriented along the [100] direction the transient signals decay much faster as expected, as the dipolar coupling between the nearest neighbor spins is the strongest. The dipolar-ordered state appears to be established within approximately 60 μs.

3.5 Conclusion

We have been able to illustrate the nature of the dipolar-ordered state by simultaneously encoding the state in the x and z bases. We have also been able to show the dynamical evolution of the spin system to the state of the dipolar-ordered state, following the application of a Jeener-Broekaert pulse pair. Such techniques open up the possibility of experimentally investigating the details of spin dynamics in a strongly dipolar coupled spin system.

Chapter 4

Multi-spin dynamics in solid state NMR free induction decay

[1] In this work, we experimentally investigate the many-spin dynamics of the NMR free induction decay. This is a classic problem in spin dynamics and has been well-studied since the early days of NMR [7, 49, 50, 51, 52, 53, 54, 55, 56].

The free induction decay (FID) is the response of the spin system following a $\pi/2$ pulse. In a solid lattice of spin-1/2 nuclei in a strong magnetic field, this evolution is dominated by the secular dipolar Hamiltonian.

In the high temperature and high field approximation, the density matrix immediately following a $\pi/2$ pulse is

$$\hat{\rho}(0) = -\sum_j \hat{I}_{jx}. \tag{4.1}$$

The system evolves under the secular dipolar Hamiltonian

$$\hat{H}_{\text{int}} = \sum_{j<k} D_{jk} \left\{ \hat{I}_{jz}\hat{I}_{kz} - \frac{1}{4}(\hat{I}_{j+}\hat{I}_{k-} + \hat{I}_{j-}\hat{I}_{k+}) \right\}, \tag{4.2}$$

[1] This chapter was drawn from sections of [13] with contributions from Dr. Thaddeus Ladd, Dr. Jonathan Baugh, and Dr. Chadrasekhar Ramanathan.

where the dipolar coupling constant D_{jk} between spins j and k is given by

$$D_{jk} = \frac{\gamma^2\hbar^2}{r_{jk}^3}(1 - 3\cos^2\theta_{jk}). \tag{4.3}$$

γ is the gyromagnetic ratio, r_{jk} is the distance between spins j and k, and θ_{jk} is the angle between the external magnetic field and internuclear vector $\vec{r}_{jk}$. Now the density matrix of the spin system at time t following the pulse can be expressed as,

$$\hat{\rho}(t) = e^{-\frac{i}{\hbar}\hat{H}_{\text{int}}t}\hat{\rho}(0)e^{\frac{i}{\hbar}\hat{H}_{\text{int}}t}. \tag{4.4}$$

The above equation is not analytically solvable, but can be expanded in a power series to examine the short time behavior of the system:

$$\hat{\rho}(t) = \hat{\rho}(0) + \frac{i}{\hbar}t[\hat{\rho}(0), \hat{H}_{\text{int}}] - \frac{t^2}{2\hbar^2}[[\hat{\rho}(0), \hat{H}_{\text{int}}], \hat{H}_{\text{int}}] + ...$$

Evaluating the commutators, we get

$$\begin{aligned}\hat{\rho}(t) = & -\frac{1}{2}\sum_j(\hat{I}_{j+} + \hat{I}_{j-}) + \frac{3}{2}it\sum_{jk}D_{jk}(-\hat{I}_{jz}\hat{I}_{k+} + \hat{I}_{jz}\hat{I}_{k-}) \\ & -\frac{3}{4}t^2\sum_{jkl}D_{lk}D_{jk}(\hat{I}_{jz}\hat{I}_{lz}\hat{I}_{k+} + \hat{I}_{jz}\hat{I}_{lz}\hat{I}_{k-}) + ...\end{aligned} \tag{4.5}$$

In an inductively detected NMR experiment (in which a coil is used to measure the average magnetization), the observed signal is given by

$$S(t) = N_{\text{spins}}\gamma\hbar < \hat{I}_+ >= N_{\text{spins}}\gamma\hbar\text{Tr}\{\hat{I}_+\hat{\rho}(t)\}. \tag{4.6}$$

The only terms in $\hat{\rho}(t)$ that contribute to the observed signal are the single spin, single quantum coherence terms. Substituting Eq. (4.5) into Eq. (4.6), it can be seen that the observable magnetization decays during the evolution under $\hat{H}_{\text{int}}$ because single spin, single quantum coherence terms are transformed to unobservable multiple spin, single quantum coherence terms by the higher order nested commutators. The n^{th} term in the expansion from Eq. (4.5) has n-spin correlations. The secular dipolar

Hamiltonian conserves coherence order in the Zeeman basis.

There have been a number of theoretical attempts to predict the shape of the FID in calcium fluoride (CaF_2) [7, 49, 50, 51, 52, 53, 54]. Calcium fluoride is a standard test system for spin dynamics as the ^{19}F (spin 1/2) nuclei are 100% abundant and form a simple cubic lattice. The main goal has been to reproduce the decay and beat pattern of the observed time domain NMR signal. For example, Engelsberg and Lowe [56] measured up to 14 moments of the FID in CaF_2, and these were found to be in good agreement with theoretically calculated values for the 2nd to 8th moments. The odd moments of the FID are zero, and the even moments are given by [7]

$$M_{(2n)} = (-1)^n \mathrm{Tr}\{\underbrace{[\hat{H}_{\mathrm{int}}, [\hat{H}_{\mathrm{int}}, [..., [\hat{H}_{\mathrm{int}}, \hat{I}_x]...]}_{\text{2n times}}] \hat{I}_x\} / \mathrm{Tr}\{\hat{I}_x^2\}. \tag{4.7}$$

Evaluating the nested commutators becomes increasingly challenging and the higher order moments are difficult to calculate. However, it is these higher moments that characterize the many spin correlations of the spin system. It can be seen that $2n^{th}$ moment arises from the $(2n+1)^{th}$ term in the expansion in Eq. (4.5), which creates up to $(2n+1)$ correlated spins. The main weakness of the moment method lies in the fact that the most important contribution to the value of the higher moments comes from the tails of the FID, which are acquired with the lowest signal to noise ratio (SNR) in typical FID measurements [7].

In this chapter, we present a new experimental investigation of the problem of the NMR free induction decay (FID) in a lattice of spin 1/2 nuclei. Following a $\pi/2$ pulse, evolution under the secular dipolar Hamiltonian preserves coherence number in the Zeeman basis, but changes the number of correlated spins in the state. To probe multiple spin dynamics during the FID, we measured the growth of coherence orders in a basis other than the usual Zeeman basis [10]. This measurement provides the first direct experimental observation of the growth of coherent multiple spin correlations during the FID.

4.1 Characterization of FID using multiple quantum coherences

Usual MQ-NMR techniques [26, 23, 27, 62] encode coherence orders in the Zeeman or z basis, but coherence numbers are conserved under the secular dipolar Hamiltonian in this basis. In our experiment we encode MQ coherences in the x basis. The dipolar Hamiltonian in the x basis is

$$\begin{aligned}\hat{H}^x_{\rm int} &= -\frac{1}{2}\sum_{j<k} D_{jk}\{\hat{I}^x_j\hat{I}^x_k - \frac{1}{4}(\hat{I}^x_{j+}\hat{I}^x_{k-} + \hat{I}^x_{j-}\hat{I}^x_{k+})\} \\ &\quad -\frac{3}{8}\sum_{j<k} D_{jk}\{\hat{I}^x_{j+}\hat{I}^x_{k+} + \hat{I}^x_{j-}\hat{I}^x_{k-}\}, \end{aligned} \tag{4.8}$$

and is seen to generate both 0 and ± 2 coherences. The coherence orders are encoded by a collective rotation about the x axis (which is the effective quantizing axis in this basis). Transforming the density matrix shown in Eq. (4.5) into the x basis yields,

$$\begin{aligned}\hat{\rho}(t)^x &= -\sum_j \hat{I}^x_j - \frac{3}{4}it\sum_{jk} D_{jk}(\hat{I}^x_{j+}\hat{I}^x_{k+} + \hat{I}^x_{j+}\hat{I}^x_{k-} - \hat{I}^x_{j-}\hat{I}^x_{k+} - \hat{I}^x_{j-}\hat{I}^x_{k-}) \\ &\quad +\frac{3}{8}t^2\sum_{jkl} D_{lk}D_{jk}(\hat{I}^x_{j+}\hat{I}^x_{l+}\hat{I}^x_k - \hat{I}^x_{j+}\hat{I}^x_{l-}\hat{I}^x_k - \hat{I}^x_{j-}\hat{I}^x_{l+}\hat{I}^x_k + \hat{I}^x_{j-}\hat{I}^x_{l-}\hat{I}^x_k) + ..., \end{aligned} \tag{4.9}$$

where $\hat{I}^x_j$ refers to the spin angular momentum operator of spin j in the x basis. From Eq. (4.9), it can be seen that even order multiple quantum coherences are created in the x basis (Odd order coherences can be created using a y basis encoding for the same initial state). Since there is a mixing of coherence orders from different spin states, a coherence number (n) in x basis does not solely arise from n-spin correlation. However, the advent of a n quantum coherence guarantees the existence of n-spin correlations.

It is useful to consider the dipolar evolution of this highly mixed state using Liouville space formulation for multiple quantum dynamics suggested previously [61].

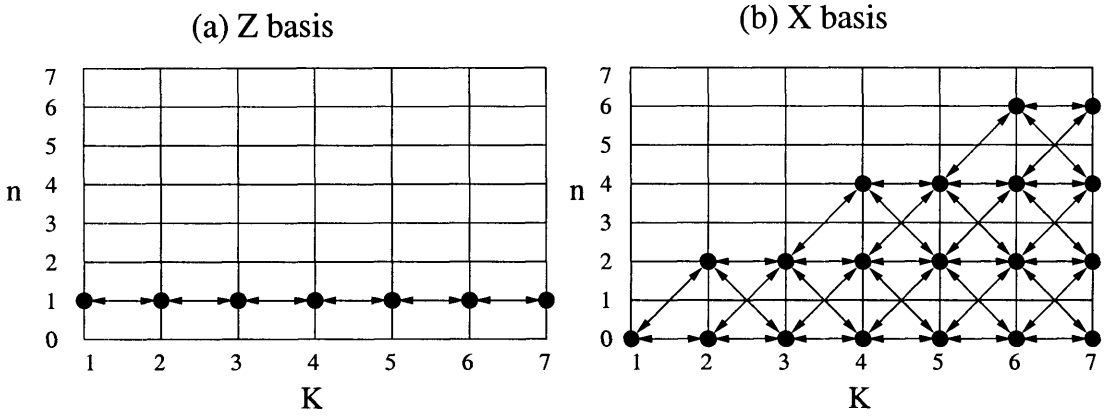

Figure 4-1: Projection of Liouville space onto the two dimensional plane $K - n$ showing the dynamics of the FID in (a) the Zeeman eigenbasis, and (b) the x basis. The arrows show the allowed paths in each case.

The density operator is now a vector in Liouville space and can be represented as

$$|\rho(t)) = \sum_{K=0}^{N} \sum_{n=-K}^{K} \sum_{p} g_{Knp}(t)|Knp), \tag{4.10}$$

where the Liouville space ket $|Knp)$ represents a basis operator which is a product of the K single-spin angular momentum operator, n is the coherence order of the operator, and p is a label that identifies a particular configuration of spins having the same K and n. The selection rules for the dipolar Hamiltonian in the Zeeman basis are given by

$$\begin{aligned} \Delta K &= \pm 1, \\ \Delta n &= 0. \end{aligned} \tag{4.11}$$

A projection of Liouville space onto the two dimensional plane $K - n$ is shown in Fig. 4-1 (a)

Following a $\pi/2$ pulse, the trajectory in the Zeeman basis is indicated by the arrows (only positive coherences are shown here-the evolution is perfectly symmetric for negative n). Increasing numbers of spins are correlated following evolution under the dipolar Hamiltonian, but the coherence number does not change. Fig. 4-1 (b)

also shows the same evolution in the x basis where the selection rules are

$$\begin{aligned} \Delta K &= \pm 1, \\ \Delta n &= 0, \pm 2. \end{aligned} \tag{4.12}$$

Starting from an initial I_x state ($K = 1, n = 0$), only even order coherences are observed.

4.2 Experimental results

The pulse sequence used in this experiment is shown in Fig. 4-2. After an initial $\pi/2$ pulse, multiple spin, single quantum states in the Zeeman basis are created during evolution under the secular dipolar Hamiltonian as described in Eq. (4.5). A $\phi\hat{I}_x$ rotation encodes coherence orders in the x basis, and a magic-echo sequence [59] is used to refocus the multiple spin terms back to observable single spin, single quantum coherence terms. The $\phi\hat{I}_x$ rotation is obtained by applying two $\pi/2$ pulses, with phases $y + \phi$ and $\bar{y}$, which results in the propagator $\exp(i\phi\hat{I}_z)\exp(i\phi\hat{I}_x)$. The initial $\pi/2$ excitation pulse is also phase shifted by ϕ to cancel out the rotation about $\hat{I}_z$. Since it is difficult to apply back to back $\pi/2$ pulses without a delay between them(without introducing phase transients or allowing some dipolar evolution during the pulses). and evolution suspension sequence needs to be used in between the two $\pi/2$ pulses. In this experiment, we use a previously described 48-pulse evolution suspension sequence. [40]

The experiments were performed at room temperature at 2.35 T (94.2 MHz, ^{19}F), using a BRUKER Avance spectrometer and home built probe. The samples used were a 1 mm^3 single crystal of CaF_2 with $T_1 \sim 7$ s, and a crystal of fluorapatite (FAP) with $T_1 \sim 200$ ms. All experiments were conducted on resonance. A 1.5 μs $\pi/2$ was used during the magic echo sequence to minimize the effect of phase transient errors. High power 0.5 μs $\pi/2$ pulses were used for the 48-pulse evolution suspension

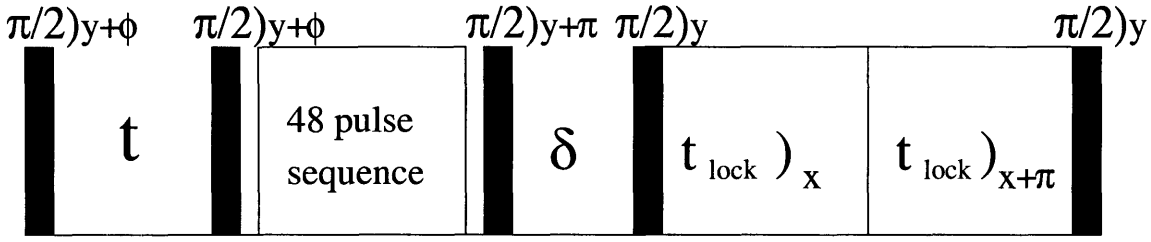

Figure 4-2: The pulse sequence used in this experiment. t is the evolution time under the secular dipolar Hamiltonian. The 48-pulse sequence was used to suppress the evolution of the internal Hamiltonian during the x basis encoding step. A magic-echo sequence was used to reverse the dipolar evolution. A delay (δ=10 μs) was inserted before the magic echo to push the echo out to minimize any pulse transient and dead time effects in the receiver. $t_{\text{lock}} = t + 2\delta + 3\mu\text{s}$

sequence [40]. The phase (ϕ) was incremented from 0 to 4π with $\Delta\phi = \frac{\pi}{32}$ to encode up to 32 quantum coherences for every experiment. A fixed time point corresponding to maximum intensity signal was sampled for each ϕ value and Fourier transformed with respect to ϕ to obtain the coherence order distribution at each dipolar evolution time (t).

4.2.1 FID in a cubic lattice of spins (^{19}F in Calcium Fluoride)

Fig. 4-3 shows the coherence order distribution observed for CaF_2 at various time points during the FID. At short times, the maximum coherence order (n_{max}) corresponds to the maximum number of correlated spins (N_{max}). At longer times, the maximum coherence order observed in the experiment sets the lower-limit of the size of the spin correlation, since the SNR of higher order coherences might be too low to be observed.

Fig. 4-4 shows the growth of the various coherence orders in CaF_2 during the FID along ~[110] direction. In order to remove the decay due to imperfect refocusing of the dipolar evolution, the intensity for each coherence order is normalized with respect to the total signal measured for that evolution time. Fig. 4-5 shows the decay patterns of measured total spectral intensity (summation over the intensities of all the coherence order, $\sum_n S_n$ for time (t)) with the pulse sequence used in the experiment as the function of the dipolar evolution time (t) for various crystal orientations. Initial

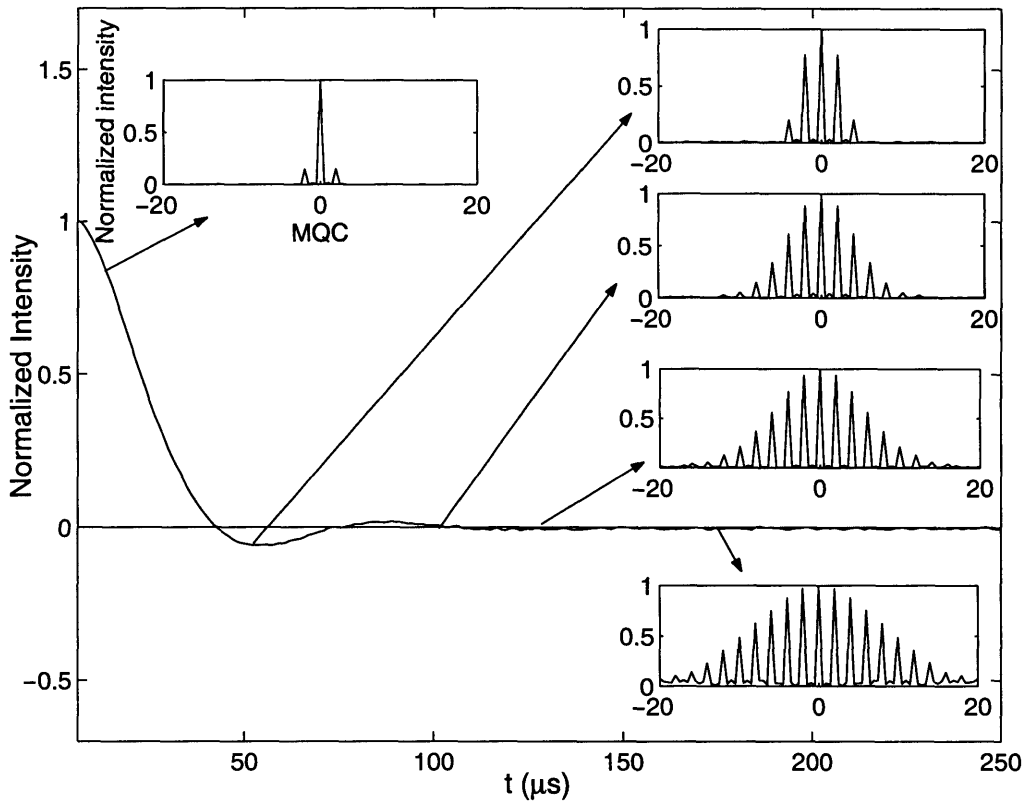

Figure 4-3: X basis coherence order distribution at various time points under the evolution of the secular dipolar Hamiltonian in CaF_2. The peak intensity has been re-normalized to put the zero quantum intensity to one in each case.

sharp decay curves are seen to be dependent on the strength of dipolar couplings and followed by flat regions and somewhat linearly decaying regimes, which are observed to be less dependent on crystal orientations. Fig. 4-6 shows the normalized growth of the various coherence orders in CaF_2 during the FID along ~[110], Fig. 4-7 and Fig. 4-8 for along [111] and [100] respectively . The inset figures show the initial oscillation between the zero and double quantum coherences at short times (which corresponds to single and two spin correlations respectively) due to the resolved nearest neighbor coupling at the [100] and [110] directions. This oscillation can be understood if we consider the dipolar evolution of two spins. For two spins, initial density matrix and dipolar Hamiltonian can be given by

$$\rho(0) = I_{x1} + I_{x2}, \tag{4.13}$$

and

$$H_D^{12} = D_{12}\left\{I_{z1}I_{z2} - \frac{1}{4}(I_{+1}I_{-2} + I_{-1}I_{+2})\right\}. \tag{4.14}$$

There exist an analytical solution of Eq. (4.4) for two spin case, and the solution is

$$\rho(t) = \frac{1}{2}\cos(3D_{12}t/4)(I_{x1} + I_{x2}) + \frac{1}{2}\sin(3D_{12}t/4)(I_{y1}I_{z2} + I_{z1}I_{y2}), \tag{4.15}$$

which shows the oscillation between the single and double spin terms in the density matrix. In the x basis representation, Eq. 4.15 transforms to

$$\rho(t)^x = \frac{1}{2}\cos(3D_{12}t/4)(I_1^x + I_2^x) + \frac{i}{4}\sin(3D_{12}t/4)(I_{1+}^x I_{2+}^x + I_{1-}^x I_{2-}^x), \tag{4.16}$$

which explains the oscillation between zero and double quantum coherences in the x basis experiment. In an extended spin system, this oscillation is rapidly damped as higher order spin correlations develop.

The higher order coherences ($n \geq 4$) are seen to follow a sigmoidal growth curve.

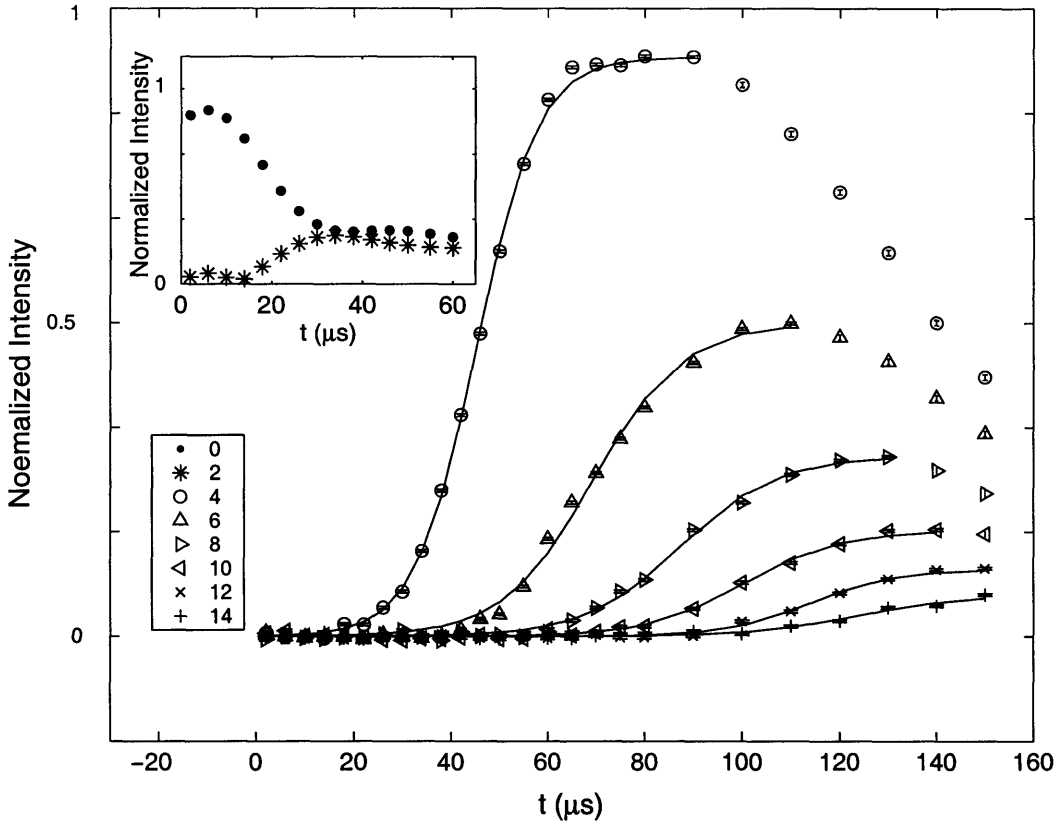

Figure 4-4: The growth of multiple spin correlations during the FID, showing sigmoidal fit to the initial growth data of each x basis coherence order ($n \geq 4$). Inset figure shows dynamics of 0 and 2 coherence orders. Along ~[110] direction in CaF_2

We have fit the initial growth data to the following sigmoidal function

$$S_n(t) = \frac{C_n}{1 + e^{-\alpha_n(t - t_n^{\text{onset}})}}. \tag{4.17}$$

A sigmoidal growth curve is typical of dynamical situations where a mass-action law appears to hold, for example chemical reactions or population growth subject to resource constraints. If we restrict ourselves to two coherence orders (S_1 and S_2) in the system and represent the increase in the signal of specific coherence order (S_2) at the expense of S_1 with α being a rate at which this transformation is driven, we can

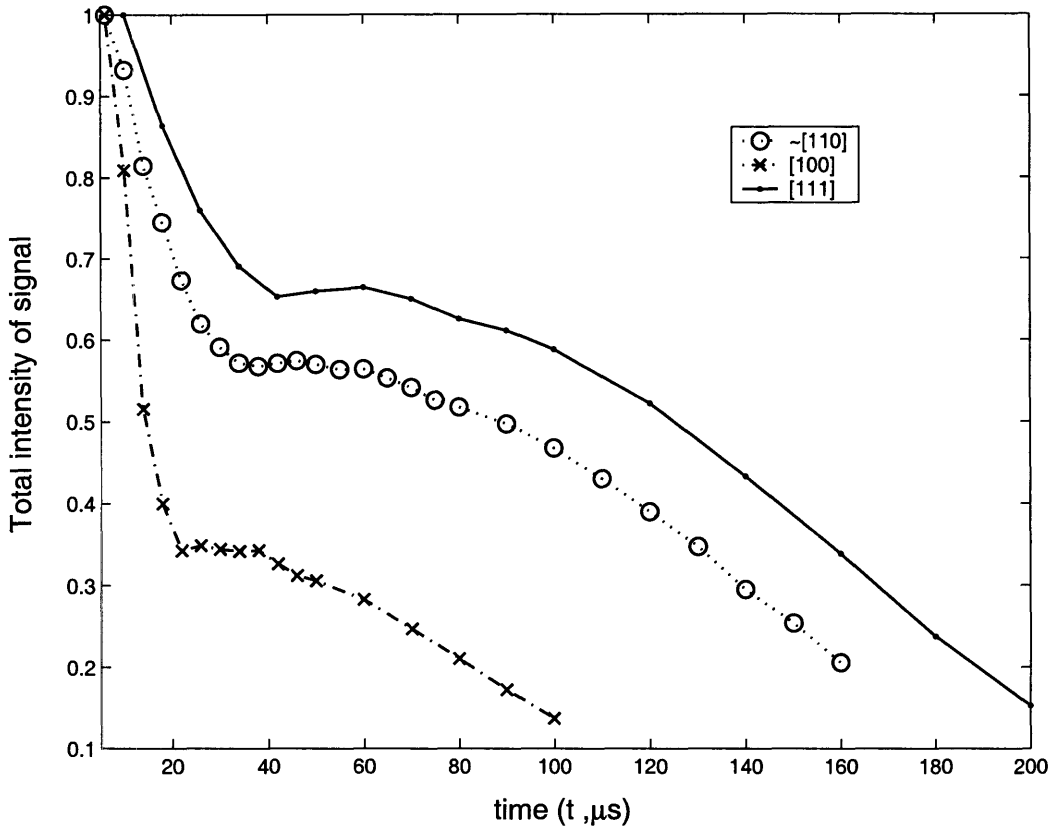

Figure 4-5: Total spectral intensity ($\sum_n S_n$) measured for various evolution time (t) under the evolution of dipolar Hamiltonian

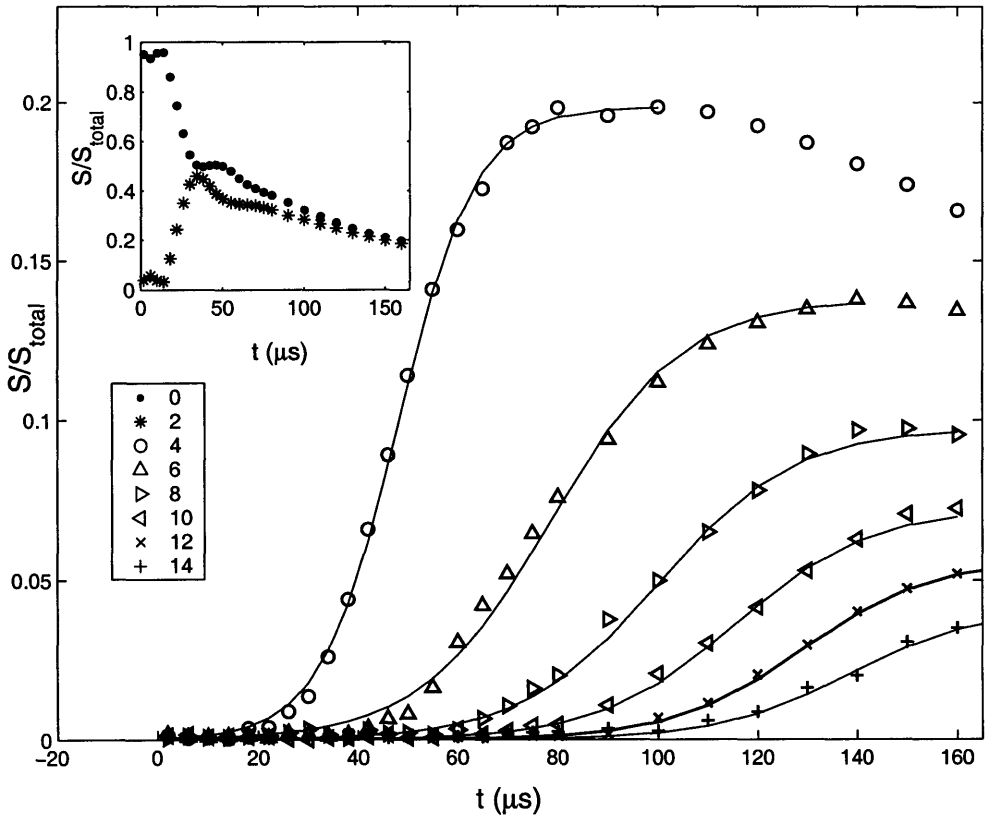

Figure 4-6: The growth of multiple spin correlations (normalized with respect to the total signal for that evolution time to compensate for imperfect refocusing) during the FID, showing sigmoidal fit to the initial growth data of each x basis coherence order ($n \geq 4$). Inset figure shows dynamics of 0 and 2 coherence orders. Along $\sim$[110] direction in CaF_2

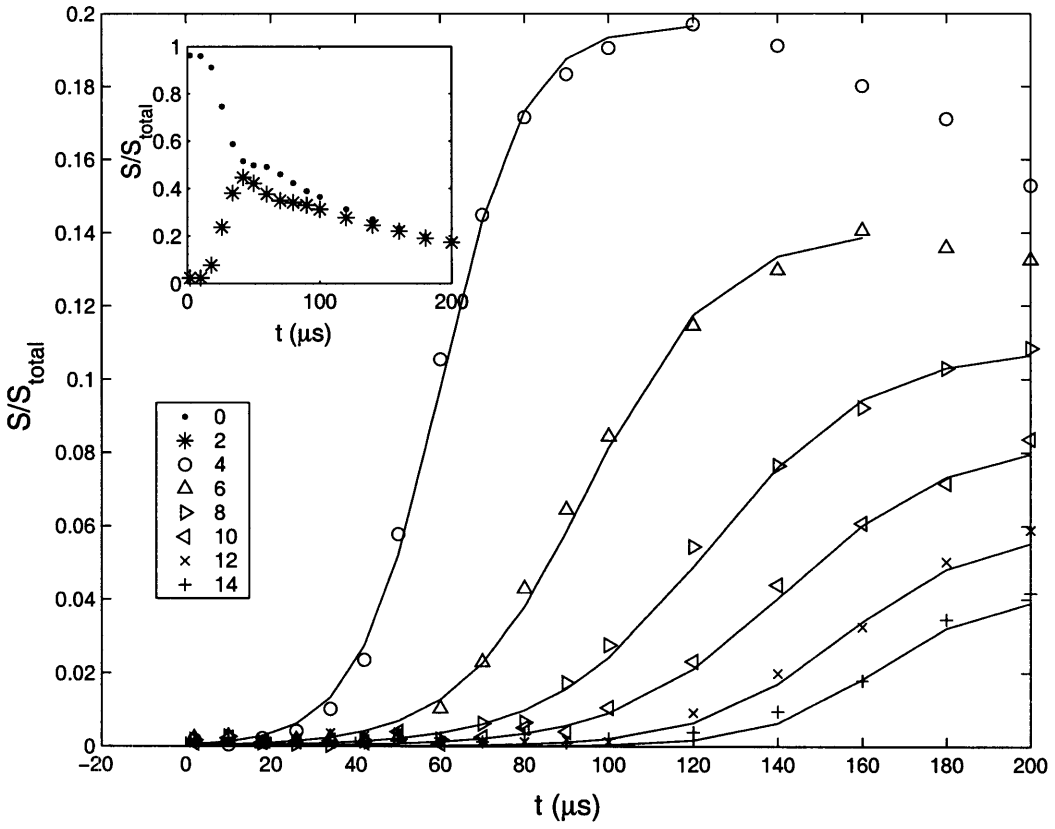

Figure 4-7: The normalized growth of multiple spin correlations during the FID along $\sim$[111] direction in CaF_2

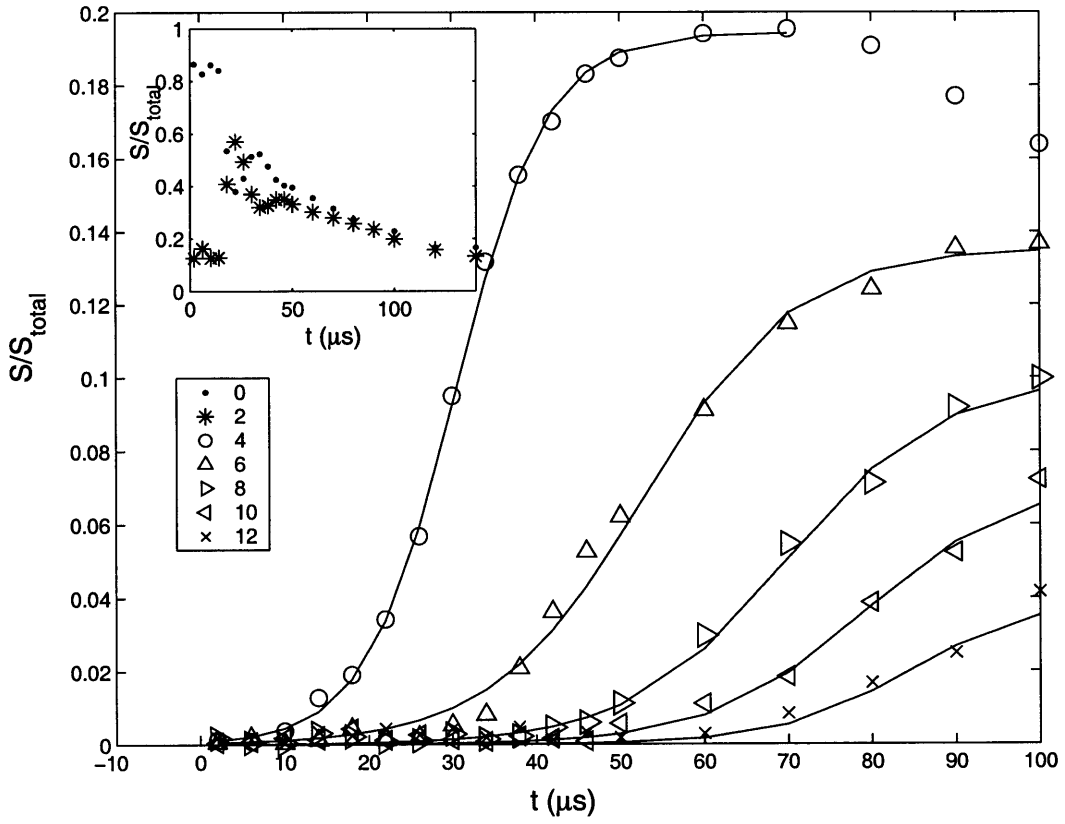

Figure 4-8: The normalized growth of multiple spin correlations during the FID along ~[100] direction in CaF_2

express this transformation as

$$S_1 + S_2 \xrightarrow{\alpha} (1+\epsilon)S_2, \tag{4.18}$$

where ϵ is the increase in the signal of specific coherence order. With the transformation given in Eq. 4.18, we can simply obtain coupled differential equations based on mass action law [60]

$$\begin{aligned} \frac{dS_1}{dt} &= -\alpha S_1 S_2, \\ \frac{dS_2}{dt} &= \alpha\epsilon S_1 S_2. \end{aligned} \tag{4.19}$$

Eq. 4.19 leads to the so-called logistic equation with $K = S_2(0) + \epsilon S_1(0)$.

$$\frac{dS_2}{dt} = \alpha(1 - \frac{S_2}{K})S_2, \tag{4.20}$$

where α is the net rate of growth of intensity of each coherence order and K is an asymptotic limit of S_2, called carrying capacity. An analytical solution of Eq. 4.20 is a sigmoidal curve (Eq. 4.17), which is used to fit the initial growth curve of each coherence order in the experiment as shown in Fig. 4-6

For further analysis, we extend the system to include a third coherence order (S_3) and add a transfer of signal of S_2 to S_3 with β being a rate at which this transfer is driven. We can write

$$\begin{aligned} S_1 + S_2 &\xrightarrow{\alpha} (1+\epsilon)S_2, \\ S_2 &\xrightarrow{\beta} S_3, \end{aligned} \tag{4.21}$$

where ϵ is the increase in the signal of S_2 as before. With the transformations given in Eq. 4.21, we can similarly obtain coupled differential equations based on mass action law [60] to get

$$\begin{aligned} \frac{dS_1}{dt} &= -\alpha S_1 S_2, \\ \frac{dS_2}{dt} &= \alpha\epsilon S_1 S_2 - \beta S_2. \end{aligned} \tag{4.22}$$

A numerical integration of Eq. 4.22 gives rise to a very similar increase and decay pattern of S_2 to the growth curve of fourth quantum order in Fig. 4-6, which shows an initial sigmoidal growth and a somewhat linearly decaying pattern at later times.

While the total polarization of the spin system is conserved, and the higher order correlations progressively develop at the expense of lower order correlations, it is not clear why a mass action behavior should be manifest in this unitary quantum mechanical processes.

In Fig. 4-9, we plot the variation of α and C_n as a function of coherence order n. The parameter α_n represents the underlying rate at which the different coherence orders are created, and should be dominated by the strength of the dipolar couplings involved. It is seen that α_n does not vary with n, suggesting that the near neighbor interactions dominate the dynamics here. As the mean dipolar coupling strength depends on the crystal orientation, we examined the variation in α_n with the crystal oriented along the [111],~[110] and [100] directions with respect to the external magnetic field. The calculated ratio of $\sum_j (|D_{1j}|N_n^j)$ for neighbor spins (lattice sum of 26 neighbor spins including the body diagonal in the cubic lattice) for different crystal orientations with respect to the external field (in a simple cubic lattice) is 1:1.45:1.87 for [111], [110] and [100], which is in good agreement with the ratios of α_n shown in the Fig. 4-9. The values of C_n are seen to decrease as the coherence number increases, independently of crystal orientation.

While a first glance at Eq. (4.5) would seem to suggest that higher order correlations should develop as t^n, it is the geometry of the spin system (the values of D_{ij}) which ultimately determines the rate at that the spin correlations grow.

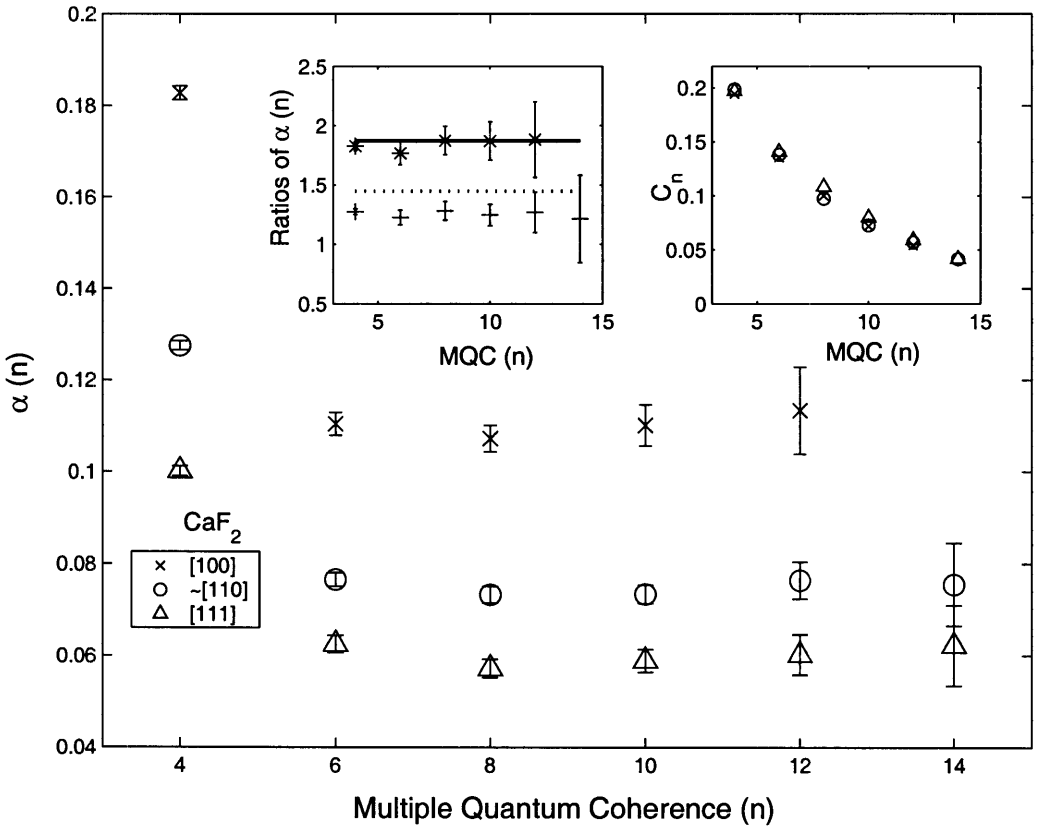

Figure 4-9: The values of α_n's for different orientations in CaF_2. Left inset shows the ratio $\alpha_{[100]}/\alpha_{[111]}(*)$ and $\alpha_{\sim[110]}/\alpha_{[111]}(+)$. The ratio of $\sum_j (|D_{1j}|N_n^j)$ for [100]/[111] (solid line) and [110]/[111] (dotted line) are also shown. The right inset figure shows the values of C_n's for different orientation in CaF_2.

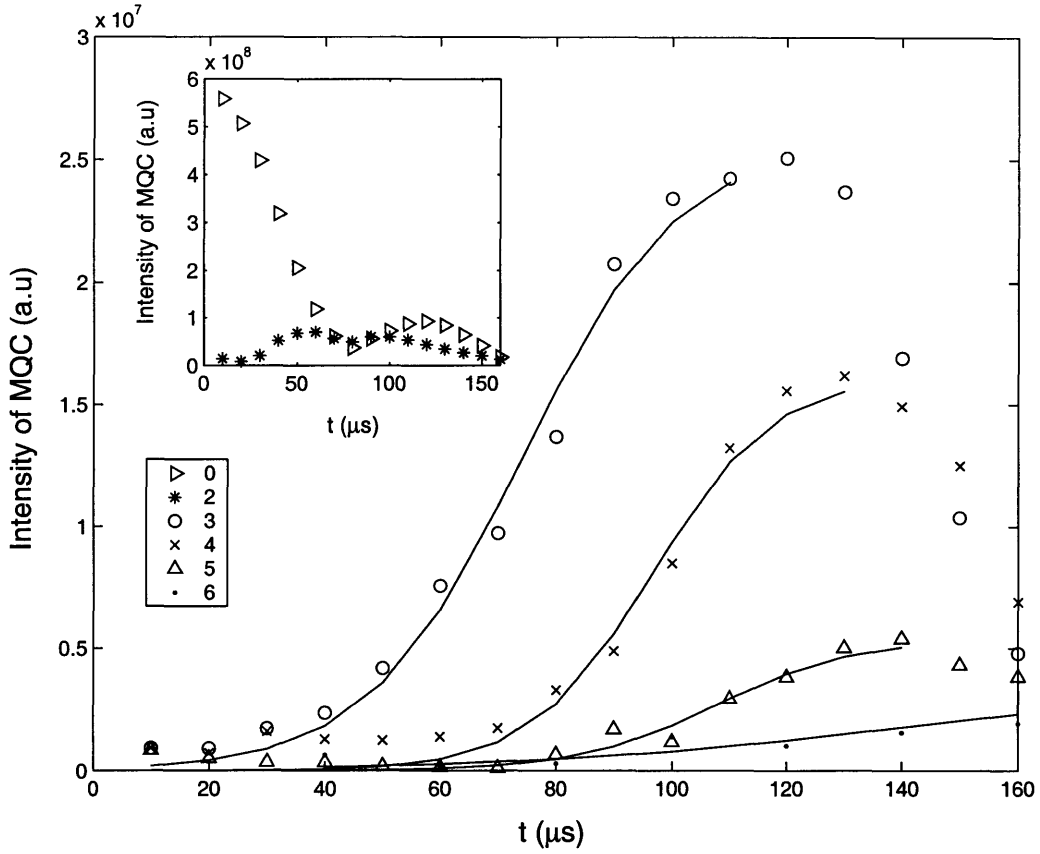

Figure 4-10: The growth of multiple spin correlations during the FID with quasi 1-dimensional a single crystal of fluorapatite, showing sigmoidal fit to the initial growth data of each x basis coherence order ($n \geq 3$). Inset figure shows dynamics of 0 and 2 coherence orders.

4.2.2 FID in a linear spin chain (^{19}F in Fluorapatite)

To verify the effect of the geometrical arrangement of spins on the development of multiple spin correlations during FID, we performed the same experiment using a quasi 1-dimensional spin chain (single crystal of Fluorapatite, shown in Fig. 4-10). Similar oscillation between single and double spin terms is also observed, and the higher order coherences ($n \geq 3$) are fit to sigmoidal curves to extract the onset time of each coherence order in a 1- dimensional spin chain. Odd coherence orders are obtained by y basis encoding on the same initial state.

4.2.3 Onset time measurements of coherence orders

Fig. 4-11 shows the onset time (t_n^{onset}) of each of the x-basis coherences for different orientations of the crystal. Physically, the onset time corresponds to the time required for a specific coherence order to become observable in the experiment. The onset times depend on the rate at which the correlations are spreading through the spin system, which in turn depends on the values of dipolar couplings. Thus the rate is expected to be fastest (shorter onset time) with the crystal orientation along the [100] direction and slowest (longer onset time) for the crystal oriented along the [111] direction. The variation of onset times with coherence order is sub-linear in the cubic CaF_2 system and displays an approximate $n^{2/3}$ dependence. The inset in Fig. 4-11 shows that the onset times obtained for FAP, the quasi 1-dimensional spin system, vary linearly with coherence number, in marked contrast to the results from CaF_2.

4.3 Discussion

A variety of models have been proposed to describe the dynamics under a multiple quantum Hamiltonian. The most commonly used model involves a random walk among the components of the Liouville space basis set $|Knp)$, subject to the selection rules of the multiple quantum Hamiltonian [61]. This model replaces the Liouville von Neumann equation with a set of coupled rate equations with exponential solutions

$$\frac{d}{dt}\mathbf{g} = \mathbf{R}\mathbf{g}, \tag{4.23}$$

where the vector $\mathbf{g}$ contains the coefficients g_{Knp}. All coherences are assumed to be of equal magnitude, and that resulting growth of the spin system is described by a hopping procedure between the allowed points on the lattice (shown in Fig. 4-1). Under this assumption, the hopping rates are solely determined by the degeneracies of the coupled states. The model thus eliminates any oscillatory solutions and precludes the possibility of quantum interference effects playing a role in the evolution. All spin systems display a universal growth kinetics, as long as the dynamics is scaled

by a lattice parameter S that represents the mean dipolar coupling strength of the system, which is similar to the parameter α obtained above. A numerical solution of the coupled equations for the multiple quantum evolution was observed to yield sigmoidal growth curves for the various coherence orders. Limitations to this model have been discussed [63].

Munowitz and Mehring used this model to numerically simulate the growth of the multi-spin dynamics of the free induction decay in a 21 spin system [57]. In order to track the development of correlations among the spins, they defined an induction time t_K over which a particular K-spin coherence reaches half of their maximum values. This parameter is very similar to the experimentally measured inset times of the different coherence orders described here. Fig. 7 of [56] shows the variation of induction times with the number of correlated spins. The numerical results show that the variation of the induction time is sub-linear for small numbers of correlated spins (<10), in agreement with the experimental data. For larger numbers of correlated spins, however, there is a marked deviation from sub-linear behavior, as the effects of the finite system size (21 spins) begin to manifest themselves in the simulations. The number of correlated spins would have to approach the number of spins in the sample ($\sim 10^{21}$) before such effects would be observed experimentally. While providing some insight into the growth dynamics for the cubic spin system, it is seen that the model fails to describe the 1-dimensional spin system completely. It is in this situation that the spin geometry plays a dominant role.

Gleason and co-workers have proposed an alternate model to describe the growth of spin correlations that emphasizes the geometrical ordering of spins [64]. The density matrix ρ is expressed as a sum of terms with spin number K and coefficient C_K,

$$\rho(t) = \sum_{K=0}^{N} C_K(t) P_K. \tag{4.24}$$

Essentially this model assumes a single effective K-spin operator that incorporates all the possible spin and spatial configurations of the K spins. The resulting model for spin propagation through a lattice yields a differential equation for the coefficients

$g_K(t)$ of the form

$$\frac{d}{dt}g_K = -i(W^f_{K-1}g_{K-1} + W^r_{K+1}g_{K+1}), \tag{4.25}$$

where the rate constants W^f and W^r correspond to the forward and reverse rates respectively. Under the assumption that the spatial grouping of the K spins is continuous, and that only the nearest neighbor couplings are important, the forward rate (and equivalently the reverse rate) can be expressed as

$$W^f_K \sim Dn_n n_s, \tag{4.26}$$

where D is the strength of the nearest neighbor coupling, n_s is the number of spins on the surface of the spatial grouping, and n_n is the number of neighbor spins coupled to each spin. New spins are added on the surface of the correlated spin cluster. While n_n is a constant, the term n_s would differ significantly for spin systems of different dimensionalities, and can be expressed as

$$n_s = K^{1-1/d}, \tag{4.27}$$

where d is the dimensionality of the spin system. For a linear spin chain, $d = 1$ and n_s is independent of K, while for a cubic spin system, $d = 3$ and $n_s \sim K^{2/3}$. While this model does not discuss coherence order, the dimensional dependence does agree with the experimental results, if the onset time characterizes the effective rate constant. In the limit of large K, the coefficients $g_K(t)$ are given approximately as

$$g_K(t) \sim (i)^{K-1}[\tanh(\beta t K^{\epsilon-1})]^K, \tag{4.28}$$

where $\epsilon = 1-1/d$ and β is a constant proportional to the mean dipolar coupling. With appropriate normalization, the magnitude of $g_K(t)$ resembles the sigmoidal growth characteristics of the normalized multiple quantum coherence intensities shown in

Fig. 4-6. An onset time can be obtained from this equation by setting

$$(\tanh(\beta t K^{\epsilon-1})^{2K} = \frac{1}{2}, \tag{4.29}$$

which yields

$$t_{1/2} = \frac{\eta}{\beta} K^{1/d} \text{arctanh}(2^{-1/2K}), \tag{4.30}$$

where η is a constant scaling factor. Fig. 4-11 shows the best fit of Eq. (4.30) to the experimental data, assuming that the model holds true for coherence number as well. It is seen that there is excellent agreement at larger values of n. The values of η/β obtained from the fits are 37.47 in the [111] direction, 31.13 in the [110] direction and 21.22 in the [001] direction. Their inverses are in the ratio 1:1.46:1.76 for [111]:[110]:[100] which is in excellent agreement with the theoretically calculated values shown earlier. Eq. (4.30) shows a super-linear behavior for 1-dimensional case ($d = 1$), which is shown in inset of Fig. 4-11. Apparently, experimental onset time measurements shows a linear behavior of onset times in 1-dimensional case, and the approximations used in deriving an analytical solution (Eq. (4.28)) are not fully capturing this feature for 1-dimensional case for low K values. Subsequently, the fit for FAP sample in Fig. 4-11 is not as good as (Eq. (4.28)) is weakly superlinear with respect to low K for 1-dimensional case (d=1). However, it is seen that Eq. (4.28) becomes more linear for large K when d=1.

Alternatively, onset time dependence on geometrical arrangements of spins can be understood by considering that the time to increase the number of spins from K to $K+1$ is $1/W_K^f$, which is also the difference between the onset times (T) of the $K+1$ and K spin correlations

$$T(K+1) - T(K) = \frac{1}{W_K^f} = \frac{1}{D n_n n_s} = \zeta K^{1/d-1}, \tag{4.31}$$

where $\zeta = 1/Dn_n$. Applying this equation recursively we get

$$T(K+1) = \zeta \sum_{j=1}^{K} j^{1/d-1} = \zeta H_K^{(1-1/d)}, \tag{4.32}$$

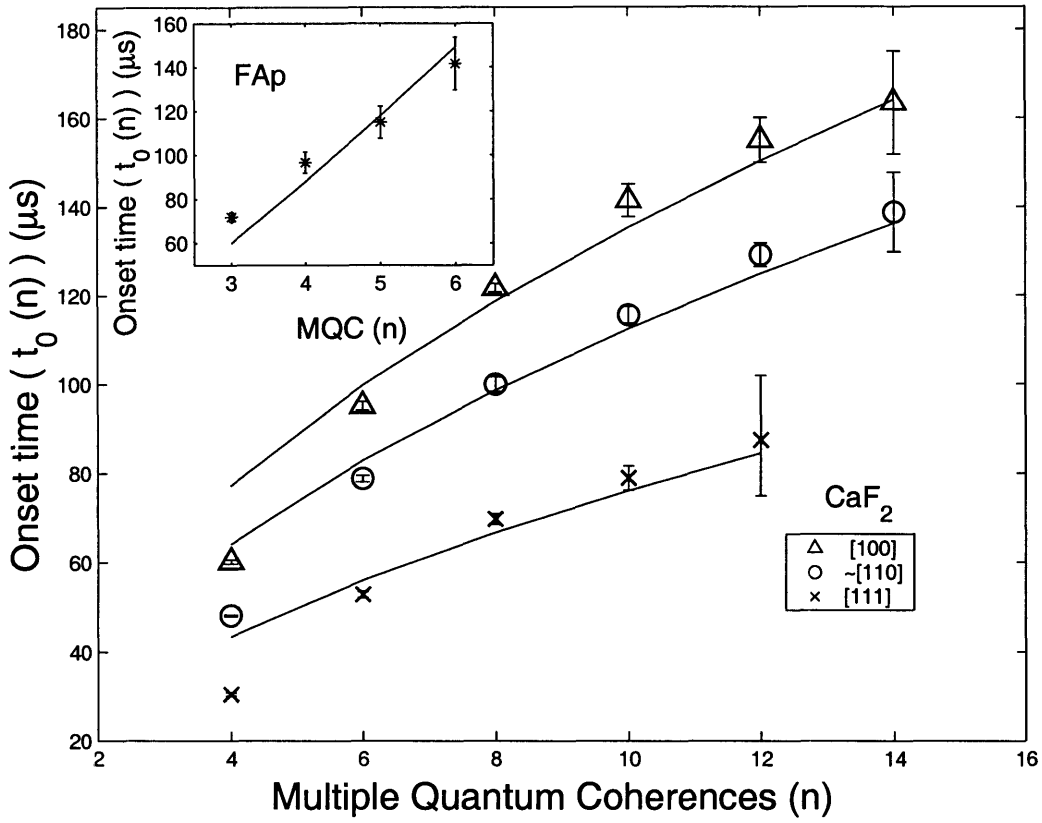

Figure 4-11: Onset time of multiple spin correlations along different orientations in CaF_2. Inset shows onset times for the FAP sample. (Odd coherence orders for the FAP sample are obtained by y basis encoding on same initial state.) The continuous lines represent the best fits of Eq. (4.30) to the data, assuming that the same equation is valid for coherence number as well.

where we have set $T(0) = 0$ and $H_K^{(1-1/d)}$ is the Harmonic Number of order $1 - 1/d$.

For a linear spin system such as FAP, $n_s = 2$, the spins at the ends of the chain, and W_K^f is independent of K. This yields

$$T(K+1) = K\zeta, \tag{4.33}$$

which shows a linear dependence of onset times on the spin number.

For a 3-dimensional spin system, such as CaF_2, Eq. (4.32) yields

$$T(K+1) = \zeta H_K^{(2/3)}. \tag{4.34}$$

Assuming that the same equation is valid for coherence number as well, the best fits of Eq. (4.34) and Eq. (4.33) are shown in Fig. 4-12. The values of ζ obtained from the fits are 34.93 in the [111] direction, 29.03 in the [110] direction and 19.64 in the [001] direction. Their inverses are in the ratio 1:1.25:1.79 for [111]:[110]:[100] which is in excellent agreement with the theoretically calculated values shown earlier also.

The constancy of α_n in the sigmoidal plots in Fig. 4-9 and the good agreement observed between the observed onset times and Eq. (4.30) indicate that the spin dynamics are dominated by the nearest neighbor interactions in this regime. This is not surprising, as we are still operating in the short time regime. Higher order spin processes, if significant, would be expected to manifest themselves at later times, leading to a deviation from the simple model described above.

4.4 Conclusion

We have presented a new experimental method to characterize multi-spin dynamics in solid state NMR free induction decay. The initial creation of coherences were observed to follow a sigmoidal growth curve, with the onset times characterizing the dynamics of the spin system. These dynamics in turn were critically dependent on the geometrical arrangement of the spins as expected.

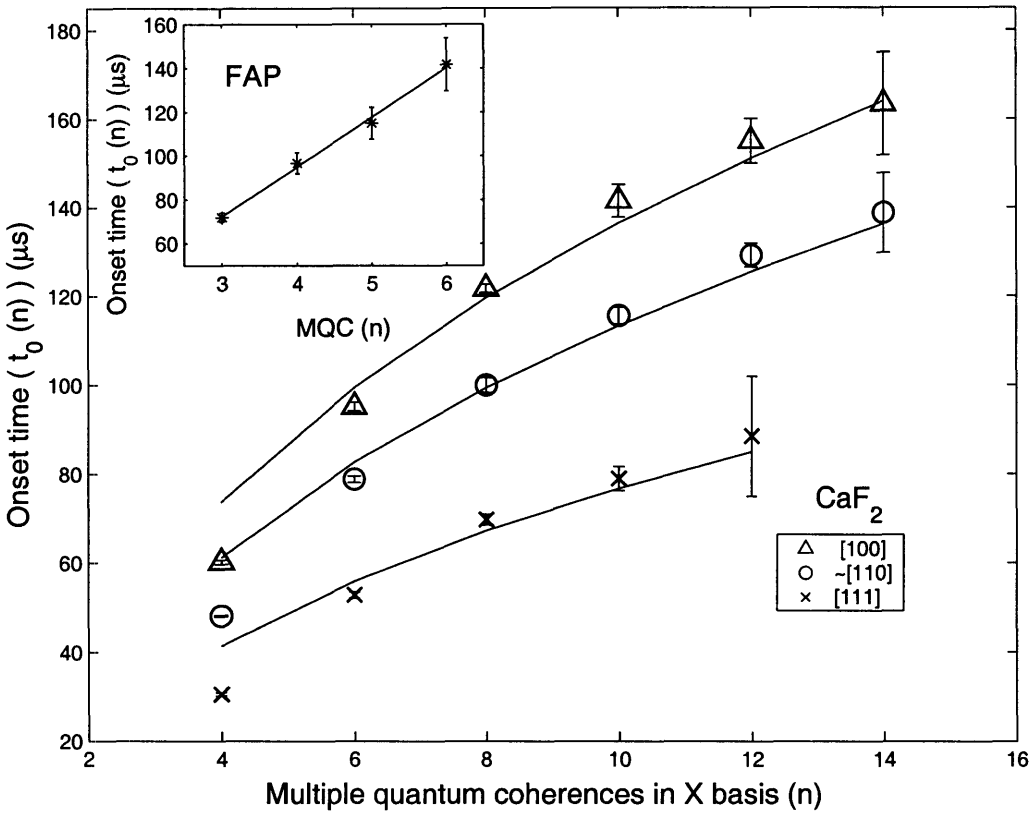

Figure 4-12: Onset time of multiple spin correlations along different orientations in CaF_2. Inset shows onset times for the FAP sample. (Odd coherence orders for the FAP sample are obtained by y basis encoding on same initial state.) The continuous lines represent the best fits of Eq. (4.34) and Eq. (4.33) to the data, assuming that the same equation is valid for coherence number as well.

Chapter 5

Experimental investigation of decay of the multiple spin correlations

5.1 Introduction

Extensive knowledge of the dynamics and the fragility of coherent quantum states is essential for implementing a reliable quantum information processor. To be a scalable quantum information processor, the ratio of coherence time of qubits to gate operation time should remain at a reasonable value even for highly correlated quantum states. In this chapter, we measure the effective T_2 decay times, and test the efficiency of our control sequence for highly correlated spin states in a solid lattice of spins. Solid state NMR provides a ideal test-bed for this study, since highly correlated spin states can be easily generated using its natural dipolar Hamiltonian. The T_2 decay in a well-defined lattice of spins is a coherent evolution of the spin system under the dipolar interaction as shown previously [13], so the measurements of T_2 decay times do not directly represent decoherence rates for highly correlated spin states, but provide detailed information of the dynamics of multi-spin states under the secular dipolar Hamiltonian. To probe the sensitivity of multi-spin states for arbitrary error sources,

we applied a control sequence that suppresses the evolution under dipolar Hamiltonian with certain errors (such as higher order terms in Magnus expansion, pulse width, and phase transients errors), and measured the efficiency of this sequence for different spin correlation size .

Controlling dipolar coupled spins has a long history, since the advent of Average Hamiltonian Theory (AHT) [66], and it has been extensively shown that control sequences using coherent averaging in spin space can be designed to achieve desirable accuracy [70, 67, 68, 69, 71, 72, 73, 77] . But usually this technique was shown to work effectively for relatively small number of spin correlations [74, 75, 76, 78]. (i.e., short cycling time for multiple pulse sequences). In this chapter, we are interested in studying the dynamics of multi-spin states under the evolution of internal Hamiltonian and in verifying our ability to control highly correlated spin states, which is to probe the fragility of these states under our imperfect control sequence.

A conventional multiple quantum sequence in solid state NMR can be used to correlate a large number of ^{19}F spins in a rigid lattice of single crystal calcium fluoride. A single crystal of CaF_2 was examined for this study. A CaF_2 crystal is well suited for this study for the following reasons. First, spin 1/2 ^{19}F is 100% abundant, and only an isotope of calcium that has non zero spin is Ca^{49} and is 0.13% abundant. Additionally, ^{19}F forms a simple cubic lattice and has a high Debye temperature which allows us not to consider any lattice vibrations. The inter-nuclear spin-spin interaction Hamiltonian is well known, and spins are almost completely isolated from other microscopic parameters that might complicate relaxation mechanisms. For the above reasons, a single crystal of CaF_2 has been widely used for various solid state NMR experiments and theory developments.

5.2 Method

In a high temperature and a high field approximation, the density matrix in thermal equilibrium is

$$\hat{\rho}(0) = -\sum_j \hat{I}_{jz}. \tag{5.1}$$

The system evolves under the double quantum Hamiltonian

$$\hat{H}_{\mathrm{DQ}} = -\frac{1}{2}\sum_{j<k} D_{jk}\{\hat{I}_j^+\hat{I}_k^+ + \hat{I}_j^-\hat{I}_k^-\}. \tag{5.2}$$

The dipolar coupling constant D_{jk} between spins j and k is given as

$$D_{jk} = \frac{\gamma^2\hbar^2}{r_{jk}^3}(1 - 3\cos^2\theta_{jk}), \tag{5.3}$$

where γ is the gyromagnetic ratio, r_{jk} is the distance between spins j and k, and θ_{jk} is the angle between the external magnetic field and inter-nuclear vector $\vec{r}_{jk}$. Now the density matrix of the spin system at time τ following the pulses can be expressed as

$$\hat{\rho}(\tau) = e^{-\frac{i}{\hbar}\hat{H}_{\mathrm{DQ}}\tau}\hat{\rho}(0)e^{\frac{i}{\hbar}\hat{H}_{\mathrm{DQ}}\tau}. \tag{5.4}$$

The above equation is not analytically solvable, but can be expanded in a power series to examine the short time behavior of the system:

$$\hat{\rho}(\tau) \;=\; \hat{\rho}(0) + \frac{i}{\hbar}\tau[\hat{\rho}(0), \hat{H}_{\mathrm{DQ}}] - \frac{\tau^2}{2\hbar^2}[[\hat{\rho}(0), \hat{H}_{\mathrm{DQ}}], \hat{H}_{\mathrm{DQ}}] + ... \tag{5.5}$$

Nested commutators give rise to multiple quantum states with selection rules of $N\pm1$ (spin number) and $n\pm2$ (coherence number).

After this step, we let spin system evolve either under the dipolar interaction or the 48-pulse time suspension sequence. The dipolar Hamiltonian is

$$\hat{H}_{\mathrm{dip}} = \sum_{j<k} D_{jk}\{\hat{I}_{jz}\hat{I}_{kz} - \frac{1}{4}(\hat{I}_{j+}\hat{I}_{k-} + \hat{I}_{j-}\hat{I}_{k+})\}, \tag{5.6}$$

and the Hamiltonian for the time suspension sequence can be approximated by neglecting arbitrary errors in experimental implementation,

$$\hat{H}_{\mathrm{time\_sp}} \sim \mathbf{0}. \tag{5.7}$$

Since an inductive NMR experiment is only sensitive to single quantum, single spin

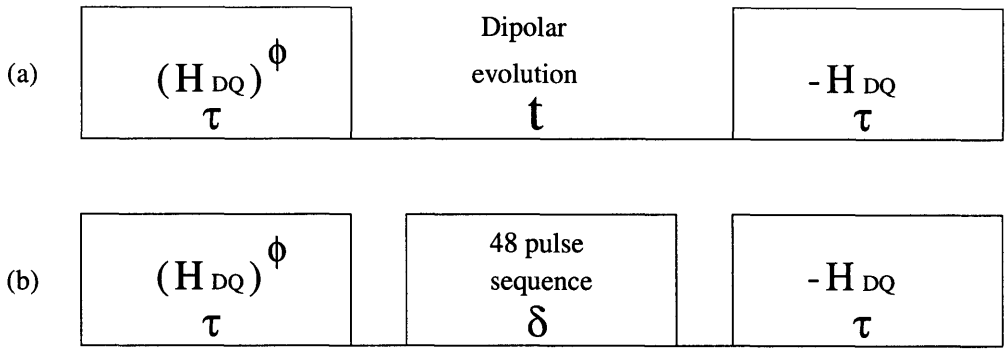

Figure 5-1: The pulse sequence used in this experiment. τ is total evolution time under double quantum Hamiltonian. t is the evolution time under the secular dipolar Hamiltonian, and δ is the cycle time of 48-pulse sequence.

terms in the density matrix, the spin system is run backward with -H_{DQ} to become observable magnetization at the end of the pulse sequence. An entire sequence can be summarized as

$$\hat{\rho}(t) = e^{\frac{i}{\hbar}\hat{H}_{\mathrm{DQ}}\tau}e^{-\frac{i}{\hbar}\hat{H'}t}e^{-\frac{i}{\hbar}\phi\hat{I}_z}e^{-\frac{i}{\hbar}\hat{H}_{\mathrm{DQ}}\tau}\hat{\rho}(0)e^{\frac{i}{\hbar}\hat{H}_{\mathrm{DQ}}\tau}e^{\frac{i}{\hbar}\phi\hat{I}_z}e^{\frac{i}{\hbar}\hat{H'}t}e^{-\frac{i}{\hbar}\hat{H}_{\mathrm{DQ}}\tau}, \qquad (5.8)$$

where H' is either H_{dip} or $H_{\mathrm{time\_sp}}$.

The change in amplitude for each coherence order under the evolution of H' can be measured separately by phase encoding with collective $\phi\hat{I}_z$ rotation.

The pulse sequence for this experiment is shown in Fig. 5-1 (a). The experiments were performed at room temperature at 2.35 T (94.2 MHz, ^{19}F), using a BRUKER Avance spectrometer and home built probe. The sample used was a 1 mm^3 single crystal of CaF_2 with $T_1 \sim 7$s. High power 0.5 μs $\pi/2$ pulses were used. The phase (ϕ) was incremented from 0 to 4π with $\Delta\phi = \frac{\pi}{32}$ to encode up to 32 quantum coherences for every experiment. A fixed-time point corresponding to the maximum intensity signal was sampled for each ϕ value, and then was Fourier transformed with respect to ϕ to obtain the coherence order distribution for each dipolar evolution time (t). Subsequently, changes in intensity of each coherence order as a function of dipolar evolution time (t) were measured.

Highly correlated multiple quantum states were prepared using the double quan-

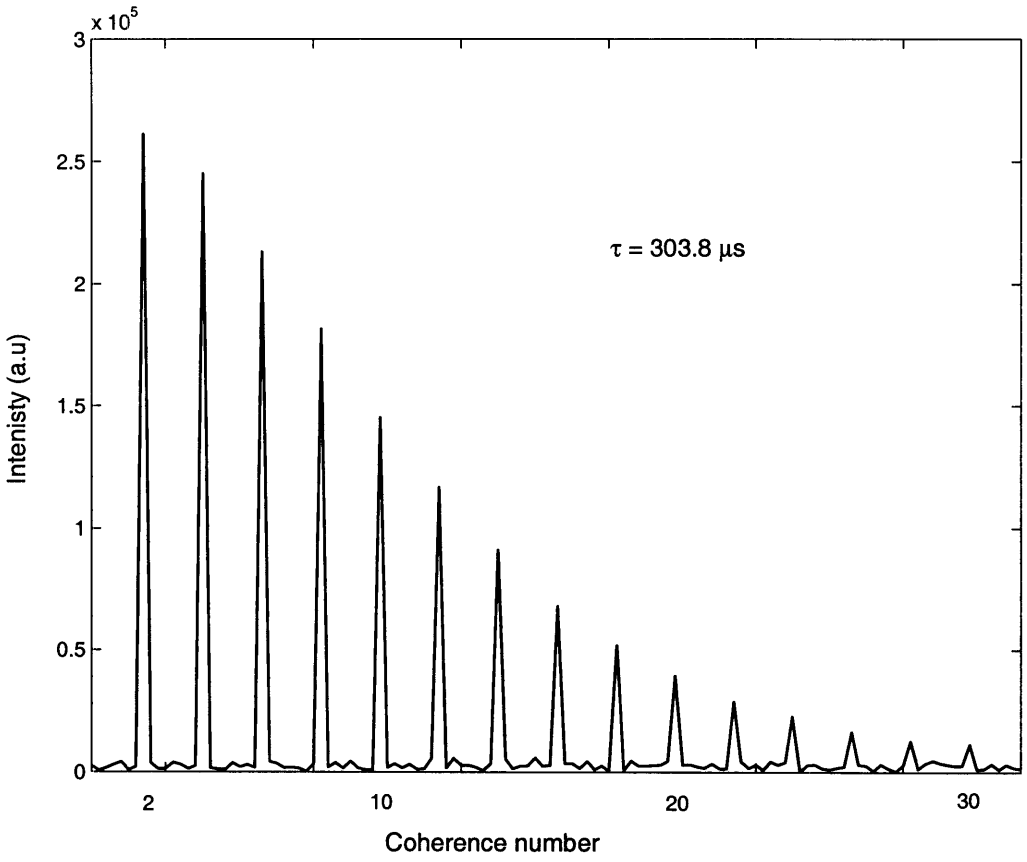

Figure 5-2: Coherence order distribution with t=0, τ=303.8 μs

tum Hamiltonian as shown in Fig. 5-2. Up to 30 coherence orders were prepared in CaF_2

5.3 Decay of multiple spin correlations under the secular dipolar Hamiltonian

Fig. 5-3 shows the intensities of various coherence orders as a function of dipolar evolution time (t) in CaF_2 for two different evolution times (τ) under the double quantum Hamiltonian. Decay curves are seen to follow Gaussian decay, and we have fit the data to the Gaussian curves to extract effective decay times for each coherence order under the dipolar interaction as a function of evolution times under the double

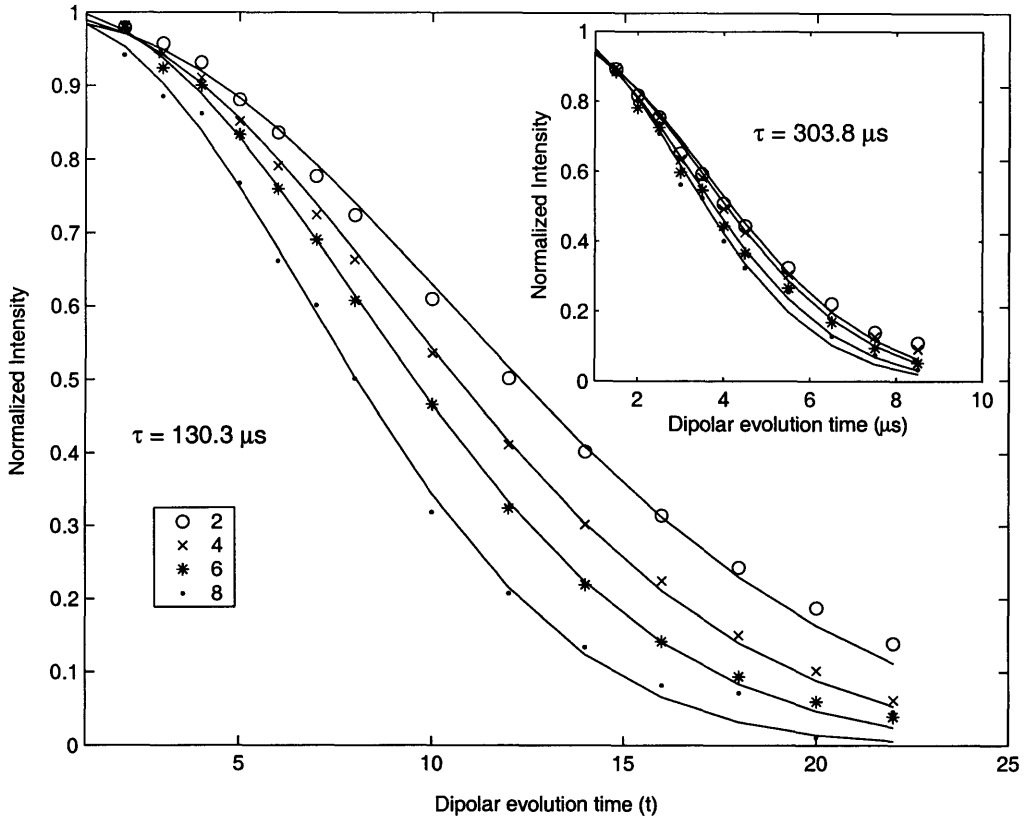

Figure 5-3: Decay of intensity for each coherence orders when τ=130.3 μs. Solid lines are Gaussian fits to the data. Inset figure shows decays of coherence orders when τ=303.8 μs.

quantum Hamiltonian (τ).

Fig. 5-4 shows effective decay times of various coherence orders for different evolution times (τ) under the double quantum Hamiltonian, obtained by Gaussian fit. It shows that decay times of the identical coherence orders gradually become smaller as evolution times (τ) become longer (along the y axis in Fig. 5-4), and the decay times of different coherence orders (along the x axis in Fig. 5-4) for the same τ time appear to become uniform as the evolution time under the double quantum Hamiltonian is made longer.

As pointed out earlier, the T_2 decay in a well-defined lattice of spins is a coherent evolution of the spin system under the dipolar interaction, and therefore the measurements of T_2 decay times do not directly represent the decoherence rates or fragilities

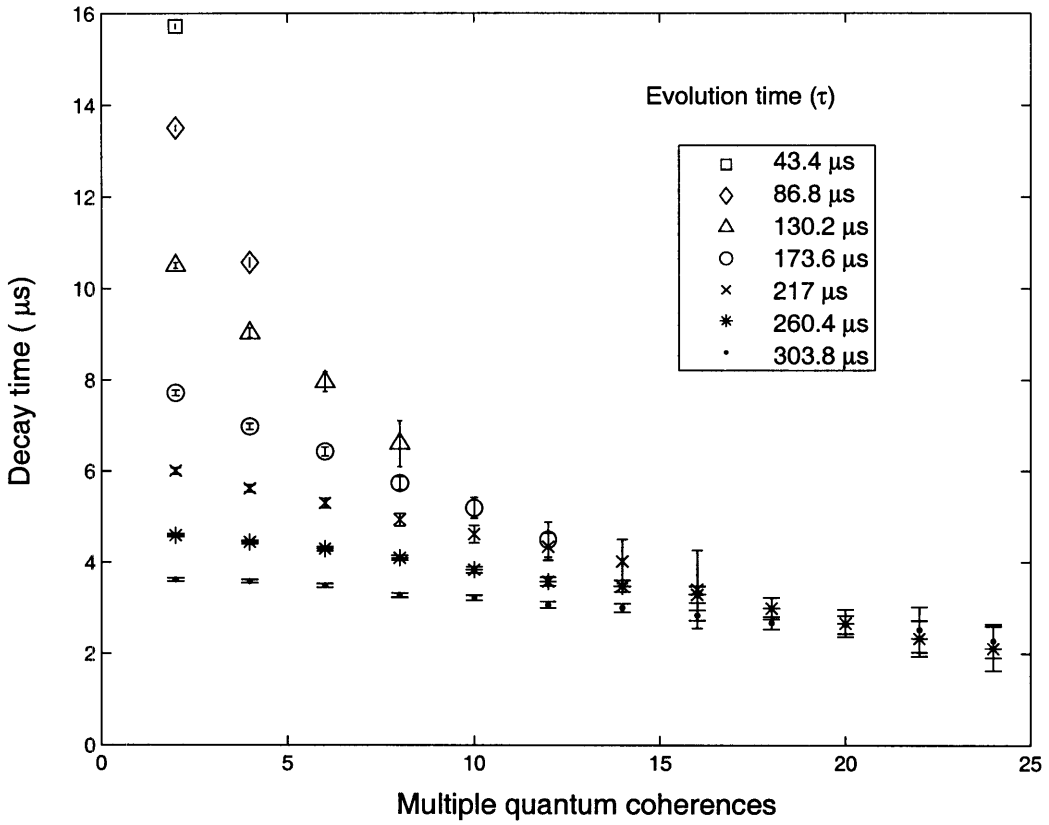

Figure 5-4: Effective decay times of various coherence orders at different evolution time under the double quantum Hamiltonian (τ)

of individual coherence orders. The intensities of coherences are decreasing under dipolar evolution because spins are getting correlated with neighbor spins, but this evolution is not refocused to observable magnetization. Qualitatively speaking, decay times of multiple spin correlations should be dominated by the coupling strength and the number of possible pathways selected by the governing Hamiltonian, not by the fragility of large spin correlations.

A full understanding of experimental decay behavior of multiple-spin, multiple-quantum states in this system is a challenging task, since it involves a lot of strongly interacting multiple spins in the process. However, we can try to study the feature of the embedded physical process by counting the number of possible transition pathways under the dipolar evolution. This approach relies on the fact that the decay of the

multiple quantum state is dominated by the unitary evolution under the dipolar interaction, which is not refocused to the observable magnetization. As pointed out in the earlier chapter, the selection rule of spin and coherence number of dipolar Hamiltonian is given as

$$\begin{aligned} \Delta K &= \pm 1, \\ \Delta n &= 0, \end{aligned} \tag{5.9}$$

where K is the number of correlated spins and n is the coherence number. Above selection rules restricts the possible transition pathways of multiple quantum states under the dipolar evolution. This process can be visualized with the help of the $K-n$ Liouville space diagram [61]. In this diagram, Fig. 5-5, the possible multiple quantum states are represented as dots on the $K-n$ plane, and these dots can move only horizontally under the dipolar evolution. Without refocusing these hopping events on the $K-n$ plane, the signal of multiple quantum states are decaying, and this decay of multiple quantum state is experimentally observed with the pulse sequence depicted in Fig. 5-1 (a).

The emergence of higher order coherences with increasing excitation time under the double quantum Hamiltonian indicates that the effective size of correlated spin clusters also increases. This growing spin cluster size is often estimated using the Gaussian distribution model of coherence numbers [27, 28]. Usually, the spin cluster size of this statistical approach has been used to estimate the maximum spin correlation size in the cluster. However, this approach does not provide any detailed knowledge of the distribution of spin cluster size for various excitation times, which is necessary to further understand the spin dynamics. At any time, a distribution of cluster size is expected to contribute to the spin dynamics. Munowitz and Mehring [57] performed a interesting simulation based on a random walk model in the $K-n$ Liouville space. They simulated the distribution of the cluster size under the double quantum Hamiltonian as a function of excitation times with 21 spins, which shows a broad distribution of spin cluster size centered at K, and this K value is seen to

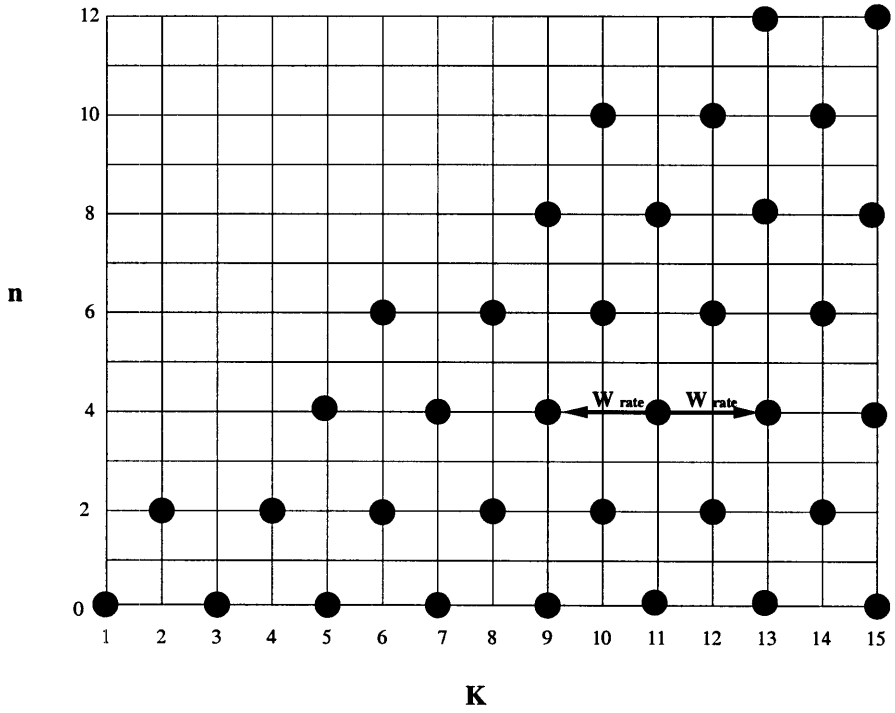

Figure 5-5: A $K-n$ Liouville space diagram. Dots represent possible multiple quantum states under the evolution of the double quantum Hamiltonian. Arrow refers to the hopping to the nearest neighbor multiple quantum states under the dipolar evolution, and W_{rate} denotes its rate.

increase as the evolution time under the double quantum Hamiltonian becomes long.

With the knowledge of the distribution of spin cluster size under the double quantum evolution and the restriction, which is imposed by the selection rules under the dipolar interaction, in the possible transition pathways on the $K-n$ plane, we can set up a simple model to quantitatively study the decay patterns of multiple quantum states under the dipolar Hamiltonian.

First, we assume a binomial distribution of spin cluster size centered at K, and assume that the value of K increases as the excitation times under the double quantum Hamiltonian increases. This assumption is not exact, but captures the correct physics and can be justified by the simulation results in [57]. Next, we initially focus on the hopping of multiple quantum state to the nearest neighbor state on the $K-n$ plane, that is a hopping of a dot from (K,n) to either $(K-1,n)$ or $(K+1,n)$ on the plane, and assume that this nearest neighbor hopping on the $K-n$ plane is dominant process determining the decay rates of multiple quantum states under the dipolar interaction.

For coherence orders $n \neq 0$, the total number of possible degenerate configurations in K spin n coherence order can be given as [63]

$$Z_n = \sum_{M_i - M_j = n} \binom{K}{K/2 + M_i} \binom{K}{K/2 + M_j} = \binom{2K}{K-n}. \tag{5.10}$$

Therefore, with a binomial distribution of spin cluster size centered at K as a initial condition of multiple quantum states created by the double quantum evolution, and the nearest neighbor hopping on the $K-n$ plane as rate limiting dynamics under the dipolar evolution, we can approximate the decay times of multiple quantum states as

$$T^n_{\mathcal{D}(K)} \sim \sum_{n \leq K_i} \frac{C(K_i)}{W_{\text{rate}} \binom{2K_i}{K_i - n}}, \tag{5.11}$$

where $T^n_{\mathcal{D}(K)}$ denotes the decay time of n coherence order with a binomial distribution ($\mathcal{D}(K)$) of spin cluster size centered at K, $C(K_i)$ is the binomial coefficient of K_i ($n \leq K_i \leq K$) spin term within the $\mathcal{D}(K)$ distribution, and W_{rate} denotes the a hopping rate of multiple quantum state to its nearest point on the $K-n$ plane. $\binom{2K_i}{K_i-n}$

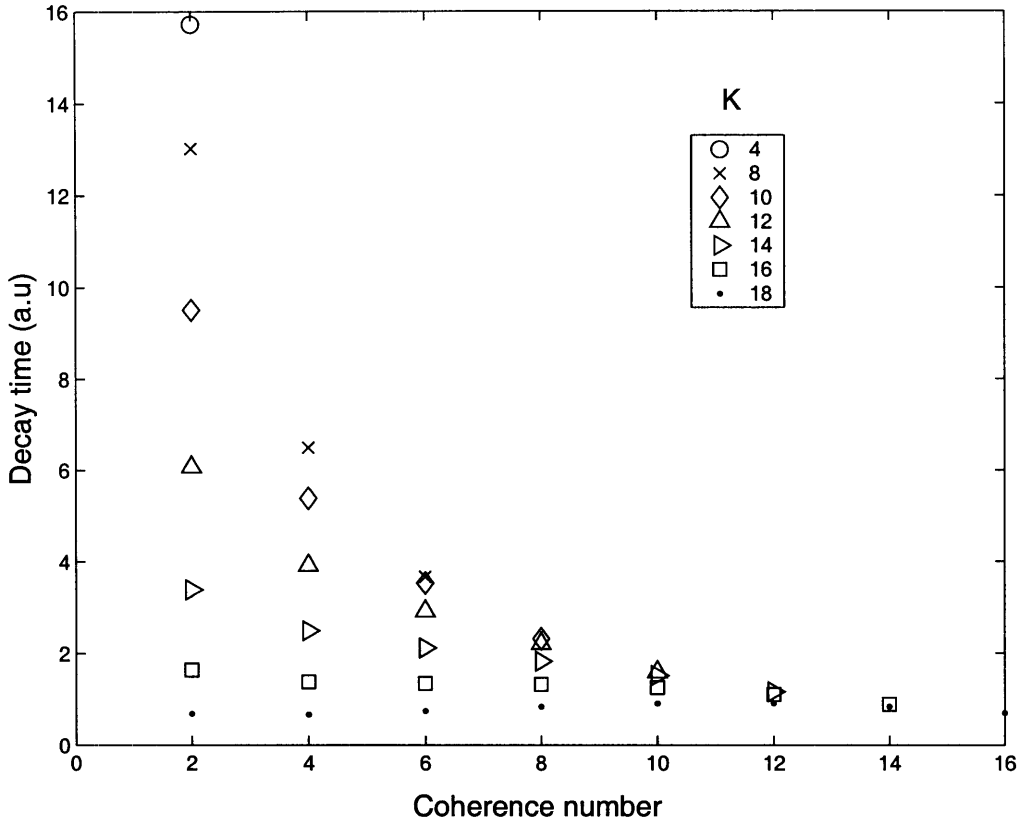

Figure 5-6: Theoretical decay times of multiple quantum states based on Eq. (5.11). The values are re-normalized for comparison with experimental data shown in Fig. 5-4.

represents the number of possible transition pathways for K_i-spin n-coherence, which is the number of degenerate states in a dot on the $K - n$ plane. It is assumed that W_{rate} remains constant for the every nearest neighbor hopping event on the $K - n$ plane, and also a identical binomial distribution ($\mathcal{D}(K)$) is used for different K values.

The result of Eq. (5.11) are shown in Fig. 5-6, and this result contains very similar features we obtained for experimental decay time measurement under the dipolar evolution shown in Fig. 5-4.

Fig. 5-7 shows effective decay times for correlated X and Z bases coherence orders under the dipolar evolution, which provides more information about the dynamics of the spin system (Method described in section 2.3.3).

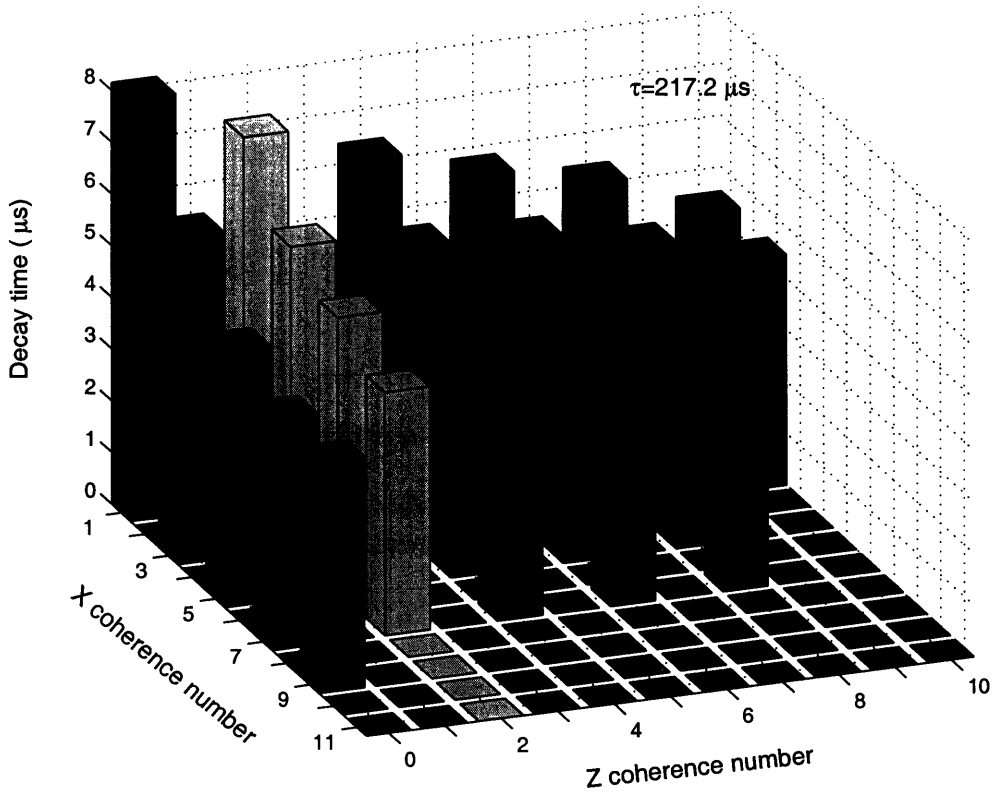

Figure 5-7: Effective decay times for correlated x and z bases coherence orders under the double quantum Hamiltonian (τ)

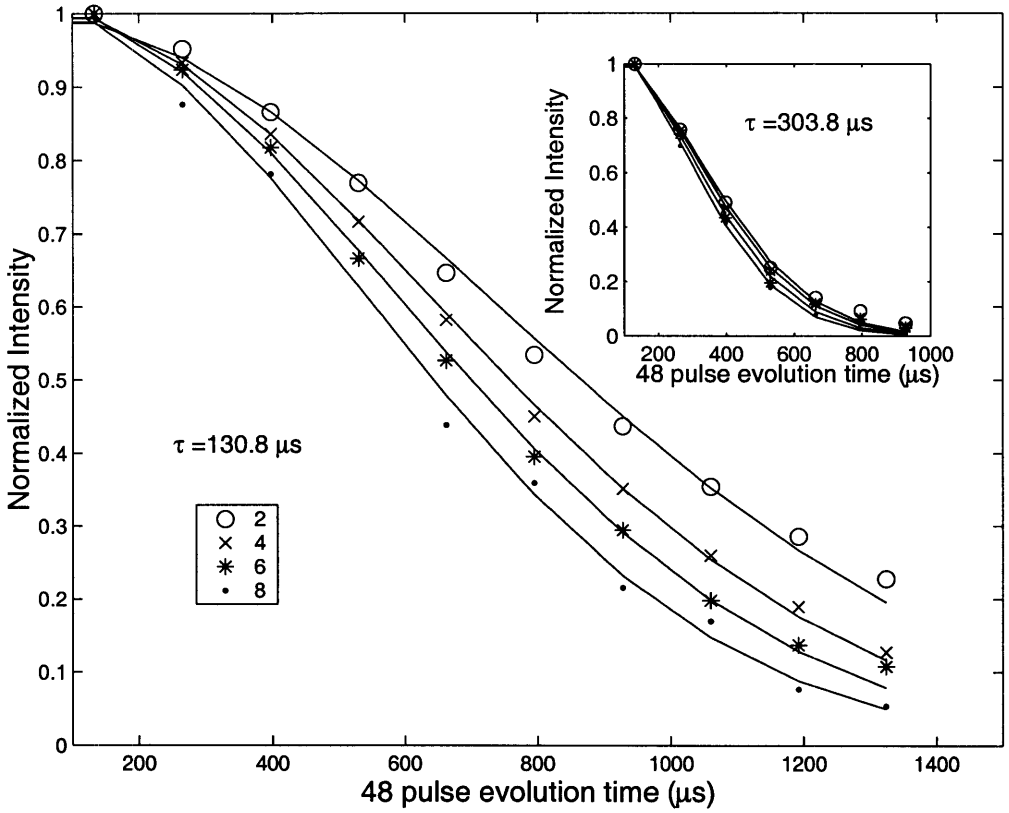

Figure 5-8: Decay of intensity for each coherence order as a function of cycle time of 48-pulse sequence when τ=130.3 μs. Solid lines are Gaussian fits to the data. Inset figure shows decay of coherence orders when τ=303.8 μs.

5.4 Decay of multiple spin correlations under a time suspension sequence

The ability to suppress all the internal Hamiltonians in a large Hilbert space is a key example of a precise control over solid state nuclear spins. We replaced the dipolar evolution during t with the 48-pulse time suspension sequence, which is suppressing the dipolar evolution to test the efficiency of this control sequence on highly correlated spin states. The pulse sequence of this experiment is shown in Fig. 5-1 (b). A cycle time of 48-pulse sequence was 132.48 μs (δ), and the change of intensity of each coherence order as a function of loop of 48-pulse sequences ($n\delta$) was measured.

Fig. 5-8 shows intensities of several coherence orders as a function of loop of 48-

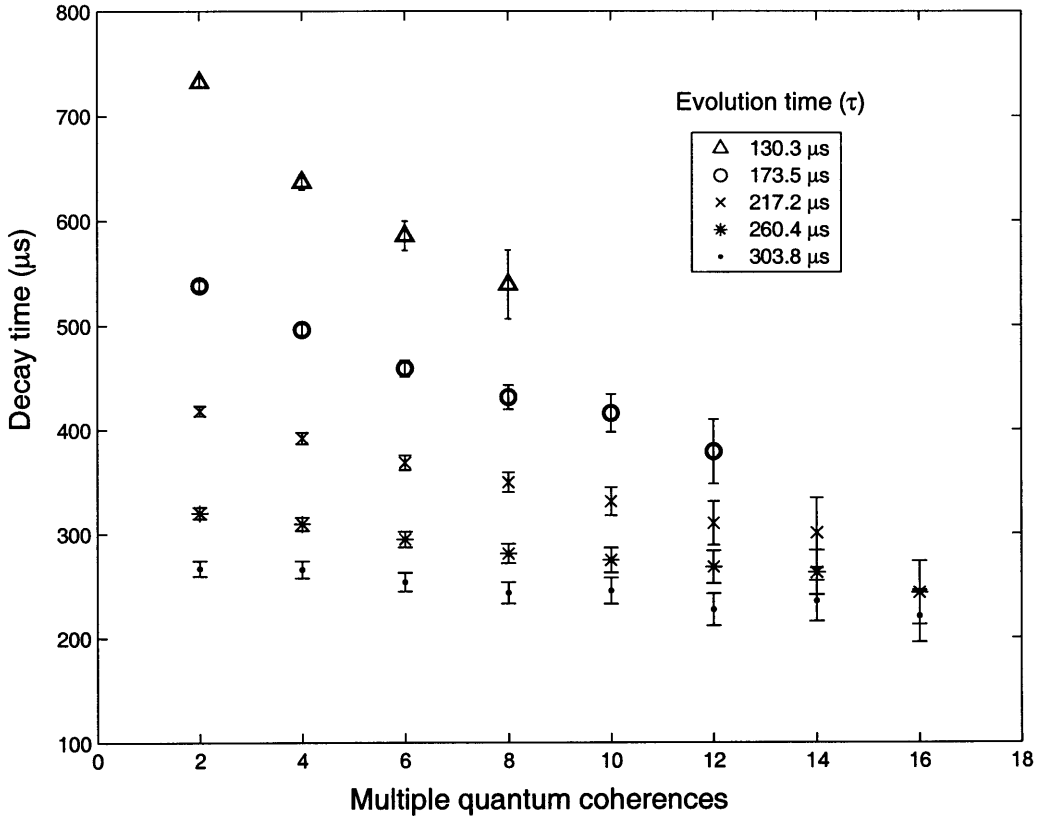

Figure 5-9: Effective decay times of various coherence orders at different evolution time under the 48-pulse sequence

pulse sequence ($n\delta$) in CaF_2. Decay curves are also seen to follow Gaussian decay, and we have fit the data to the Gaussian curves to extract effective decay time for each coherence order.

Fig. 5-9 shows effective decay times of coherence orders obtained by fitting the decay of coherence order intensities under the evolution of 48-pulse sequence to Gaussian curve. It shows very similar behavior to the decay time measurements under the dipolar evolution.

Fig. 5-10 shows effective decay time for correlated X and Z basis coherence order under 48-pulse time suspension sequence (Method described in section 2.3.3), and it also shows very similar behavior to Fig. 5-7.

Fig. 5-11 shows the ratio of decay time of multiple quantum coherences under

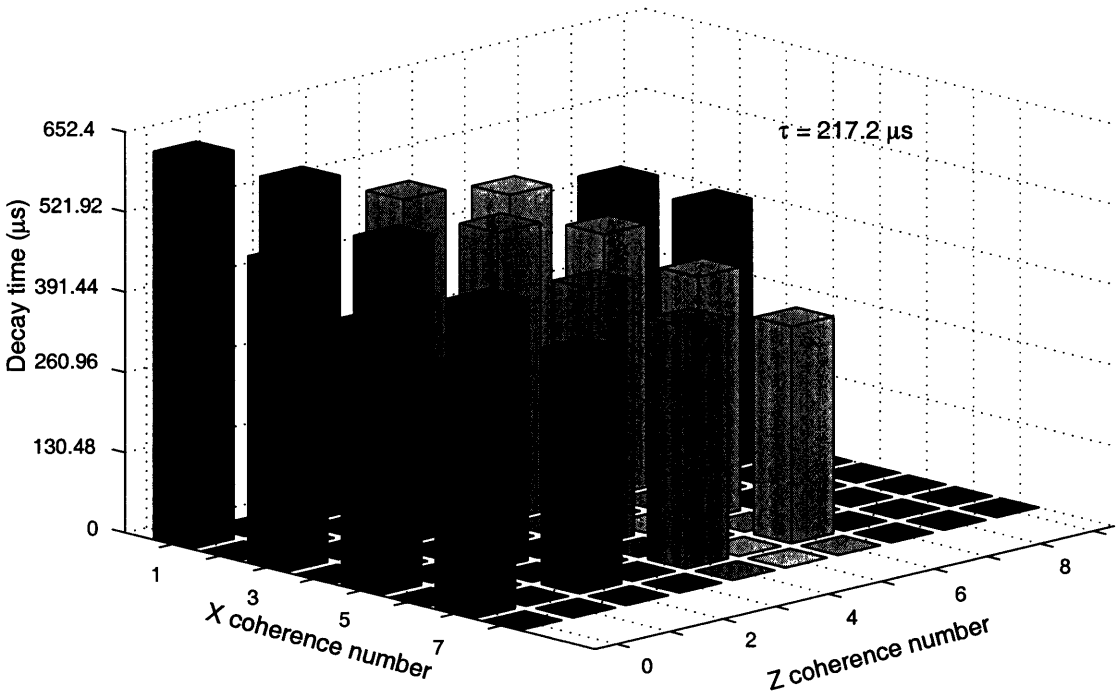

Figure 5-10: Effective decay times for correlated x and z bases coherence orders under the 48-pulse time suspension sequence

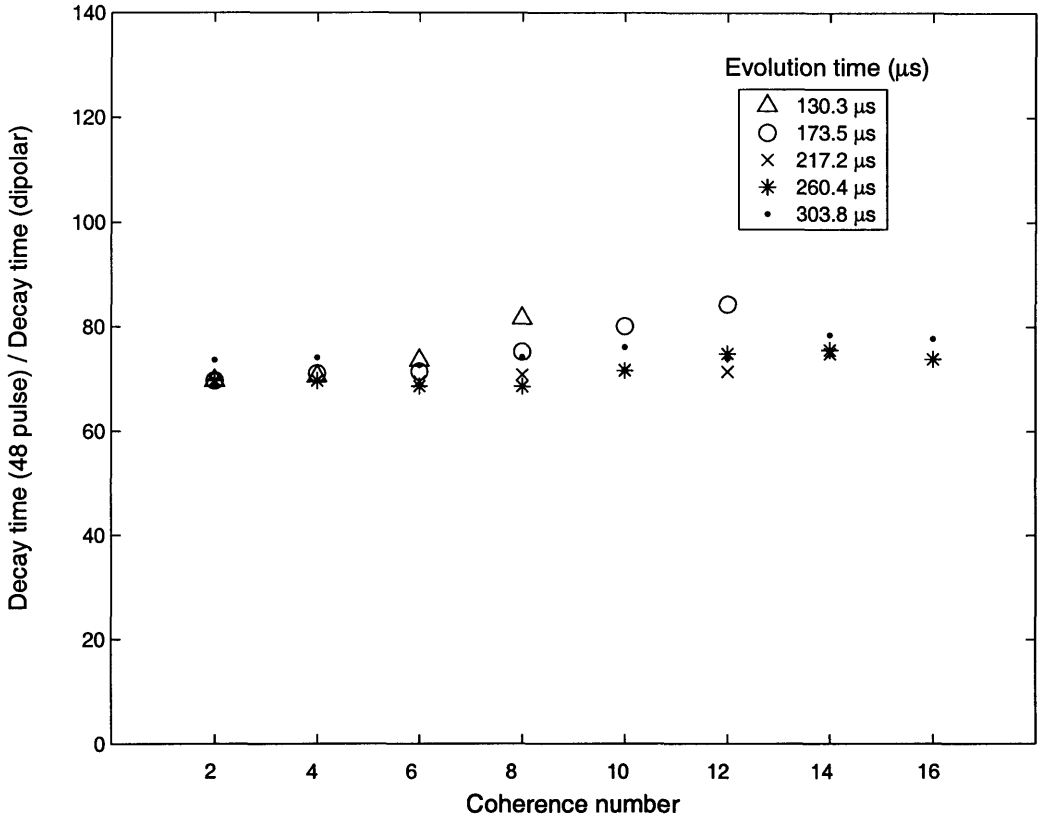

Figure 5-11: Ratio of decay time under the 48-pulse sequence to decay time under the dipolar evolution

48-pulse sequence to decay time under dipolar evolution to see the efficiency of 48-pulse sequence over various size of spin correlations. The efficiency of our control sequence appears to be maintained around 70 regardless of the size of spin correlations experimentally created in CaF_2 sample.

5.5 Discussion

We measured the effective T_2 decay time of highly correlated spin states in a single crystal CaF_2, and tested the efficiency of our control sequence on these states. Effective T_2 decay times are observed to be faster for larger spin correlations and to become uniform among different coherence orders as the evolution time under the double quantum Hamiltonian gets longer in a single crystal CaF_2. A theoretical decay

times are estimated based on the number of possible transition pathways on the $K-n$ Liouville space, and are seen to reproduce the features of experimental decay time measurements under the dipolar evolution. Additionally, it is seen that the efficiency of our control sequence, which is the ratios of the effective T_2 decay times of various coherence orders to decay times under of our control sequence remain unchanged regardless of the size of spin correlations experimentally probed.

Chapter 6

Toward state purification in solid state nuclear spins

Liquid state NMR allowed us to implement key quantum algorithms and to develop control methods in small quantum systems. These studies have been limited up to 10 qubits, primarily because creating pseudo-pure state from highly mixed states at room temperature requires exponential costs either in the signal strength or the number of experiments involved.

In the solid state, the nuclear spins can be highly polarized using technique such as Dynamic Nuclear Polarization (DNP) by polarization transfer from electron spins. DNP can significantly increase the nuclear polarization in a coupled electron-nuclear spin system by irradiating near Electron Spin Resonance (ESR) frequency [7]. In theory, signal enhancement on the order of γ_e/γ_n is obtainable.

Efficiency of DNP enhancement primarily depends on the microwave power and the length of spin-lattice relaxation time of both nuclear and electron spins. With limited available high power microwave source at a specific frequency range, most DNP experiments have been performed at low temperatures to maximize the efficiency of polarization transfer process.

In this chapter, we describe the design and the fabrication of low temperature DNP probe which enables multiple pulse irradiations at low temperature environments and microwave irradiation with horn system. Our design approach will be presented to

achieve highly efficient rf circuitry as well as good thermal contact and anchoring of samples while maintaining a high vacuum to prevent rf breakdown at gaseous He cooled environments. A mode structure inside the microwave horn-mirror cavity is studied using HFSS (High Frequency Structure Simulator, Ansoft) simulations, and preliminary DNP results are presented with signal enhancement in TEMPO and BDPA samples. Proposed modification of microwave cavity for enhanced efficiency will be discussed.

6.1 Theory of Dynamic Nuclear Polarization (DNP)

In solids, containing magnetic nuclei and unpaired electron, polarization transfer between electron and nuclear spin systems can be obtained. This enhancement in nuclear polarization is called Dynamic Nuclear Polarization (DNP). There are several mechanisms that explain the transfer processes of electron polarization to nuclear polarization. Extensive reviews of DNP have been documented elsewhere [7, 80, 81]. In this chapter, we will give a brief introduction of the different DNP mechanisms: which are Overhauser effect, solid state effect and thermal mixing effect.

In general, the Hamiltonian of an interacting electron and nuclear spin system in an external magnetic field can be given as

$$H = -\omega_e S_z - \omega_n I_z + H_{ee} + H_{en} + H_{nn}, \tag{6.1}$$

where the first two terms represent Zeeman interaction of electron and nuclear spin. H_{ee}, H_{nn}, and H_{en} represent spin-spin interaction between electron-electron, nuclei-nuclei, and nuclei-electron respectively. H_{en} is also called hyperfine interaction and is the most important term for DNP enhancement. Hyperfine interaction between nuclei and electron give rise to simultaneous electron-nuclei transition when the electrons are irradiated at electron Larmor frequency, which is the key requirements for DNP. Generally, the scalar interaction term H_{en}^{s} and the dipolar interaction term H_{en}^{d} are two parts of hyperfine interaction.

Historically, Overhauser first proposed that the NMR signal in metals can be enhanced by saturating the resonance line of conducting electrons [79]. This is called Overhauser effect, which occurs when H_{en} is time-dependent on a time scale of the order $1/\omega_e$. Then $H_{en}(t)$ can induce relaxation transitions between the electron-nuclei energy levels, resulting in a change in nuclear polarization when the spin system is irradiated at the electron Larmor frequency. This required time dependence condition can be met in conductors or semiconductors, where conducting electrons move very fast. The enhancement factor of the Overhauser effect is given by

$$(P)_{\text{Overhauser}} = 1 - \frac{W}{W + W_e}\frac{W_0}{W_0 + W_n^a}\frac{\gamma_e}{\gamma_n}, \tag{6.2}$$

where $W = \pi\gamma_e^2 B_1^2 g(\omega - \omega_e)$ is the induced transition probability driven by irradiation near electron Larmor frequency ($g(\omega - \omega_e)$ refers to the normalized line-shape function of the ESC line and B_1 is the magnitude of the microwave magnetic field), W_o, W_e and W_n^a correspond to the relaxation rate of the electron-nuclear system, the electron Zeeman relaxation rate, and the nuclear autorelaxation, respectively [82]. Enhancement is maximal when $\omega = \omega_e$, and becomes $1 - \gamma_e\gamma_n$ when $W >> W_e$ and $W_o >> W_n^a$.

Solid state effect can be induced in solids with fixed paramagnetic centers and with electron-nuclear interactions that are time independent. This time independent hyperfine interaction leads to a mixture of electron-nuclear states from the second order perturbation theory. The energy level of electron-nuclear system ($|m_n m_e>$) is modified due to this mixture as follows,

$$\begin{aligned}
|-+> &\rightarrow |-+> + q|++> \\
|++> &\rightarrow |++> - q^*|-+> \\
|--> &\rightarrow |++> - q|+-> \\
|+-> &\rightarrow |+-> + q^*|-->,
\end{aligned} \tag{6.3}$$

where $q \sim \gamma_e\gamma_n/\omega_n$ is a mixture constant.

Since eigenstates are mixed, a small nonzero transition element such as $q < + - |H_{rf}| + + >$ give rise to what is called forbidden transitions. ($W^{\pm}$)

$$W^{\pm} = 2|q|^2 \pi \gamma_e^2 B_1^2 g(\omega_e - \omega \pm \omega_n). \tag{6.4}$$

With forbidden transitions driven by microwave irradiations, the enhancement factor of solid state effect is given by

$$(P)_{\text{solideffect}} = 1 + \frac{W^+}{W^+ + W_n}(\frac{\gamma_e}{\gamma_n} - 1), \tag{6.5}$$

where W_n^e corresponds to the nuclear relaxation rate [82].

Thermal mixing effect has features similar to those of the solid state effect, and occurs primarily when the concentration of unpaired electrons is so large that the ESC line has a homogeneously broadened line. More details of thermal mixing effect can be found elsewhere [84].

6.2 Design and fabrication of low temperature DNP probe

6.2.1 Low temperature NMR probe

As pointed out in the earlier section of this chapter, it is important to design and fabricate robust NMR probe enabling low temperature operations to achieve highly efficient transfers of electron polarization to nuclear polarization in DNP experiments. Obviously, no single design is suitable for all low temperature NMR experiments, and the choice of the cryogenic apparatus poses substantial constraints on the NMR probe. We used a top-loading continuous flow cryostat, called spectrostatCF from Oxford Instruments which are fitted in the bore of a superconducting magnet. Our design specifications for low temperature NMR probe are meant to comply with dimensional and functional aspect of this cryostat, but should be general enough for any other cryostats that are being used in low temperature NMR applications.

Major issues in designing NMR probes for low temperature applications in solid state NMR have two goals. One is to maintain efficient rf circuitry so that high power rf pulses can be applied for good manipulation of spins as at room temperature applications, while enabling adjustable tuning and matching ability of resonant frequency. The other is to prevent a rf breakdown under multiple pulse irradiations.

The simplest approach for tunable rf circuitry for low temperature applications is to keep the tuning and matching elements of circuit outside the cryostat at room temperature inside a shielding can. This design is very simple and easy to build, but the long transmission line becomes the part of a LC resonant circuit so that power efficiency of this circuit is poor, because typically a transmission line is much longer than the coil wire itself. An alternative approach that needs no tuning parts at low temperatures is design by McKay [87]. In his approach, he used a very large coaxial line to simply reduce the losses in the transmission line. The drawback to this approach is that this design will take up too much space. Our approach is to keep the tuning and matching capacitor close to the coil to maintain high efficiency of the circuit; this is critical for high power multiple pulse solid state NMR applications. We used copper plated sapphire tube (7.8 mm OD, 4.8 mm ID, 14 mm in length) and piston mechanism to obtain 1-12 pF tunability capacitors which can be tuned at low temperatures. Thickness of copper plating was 50 micron taking into consideration that the skin depth of copper at 100 MHz is $\sim$7 micron. Piston design using beryllium copper bellow (part number : BC-159-60-125 from Mini-flex Corporation) was designed to enable vertical motion of a inner conductor (copper rod) inside a copper plated sapphire tube to achieve the tunability of capacitance while maintaining a high vacuum seal around rf circuitry and the sample area.

Fig. 6-1 shows a schematic diagram of this custom made piston capacitor assembly. A housing ring (HO31 from Rotor Clip, Inc) that was mounted inside the adapter on top of the bellow was used to keep a screw in place so that the bellow can be either extended or contracted with rotational motions provided by the screw. Unfortunately, very little electric power leads to rf breakdown in gaseous He environment at low temperatures. There might be no need to worry about this breakdown for a one-

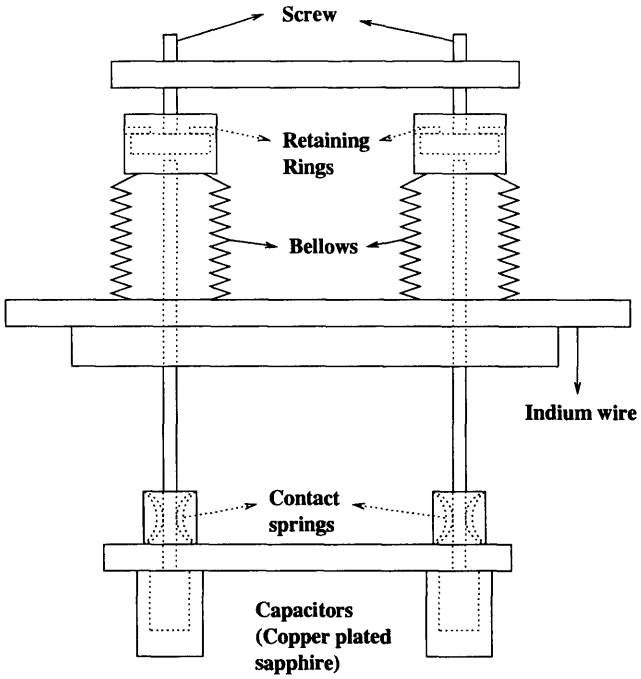

Figure 6-1: A schematic diagram of piston capacitor assembly

pulse experiment, but long spin locking irradiations or multiple pulses cannot avoid rf breakdown. To prevent rf breakdown, we put the tuning circuits and rf coil inside a custom made vacuum can ($\sim$ 1x10^{-5} Torr at 4 K). Obviously, cooling down the sample by thermal contact is a critical issue with vacuum can approach. We initially used conflat flange from Varian, Inc on the bottom of our probe so that we can open up this conflat flange to gain access to the rf coil area, and mounted our sample on the end of the sapphire tube and thermally anchored this sapphire onto the side of the can wall using low temperature grease. This scheme gave us successful low temperature measurements but changing and orienting samples was too cumbersome. To improve sample preparation, we tested copper tapered conical and greased seal (Dow Corning silicon grease was effective below 4 K), which also works as a sample mount. The advantage of using this approach is that one can easily change the samples without opening the entire vacuum can, and the sample (when it is crystal) orientation can be systematically varied by rotating conical seal with respect to the vacuum can wall. Fig. 6-2 shows a picture of this conical seal and a dial on the vacuum can wall. The

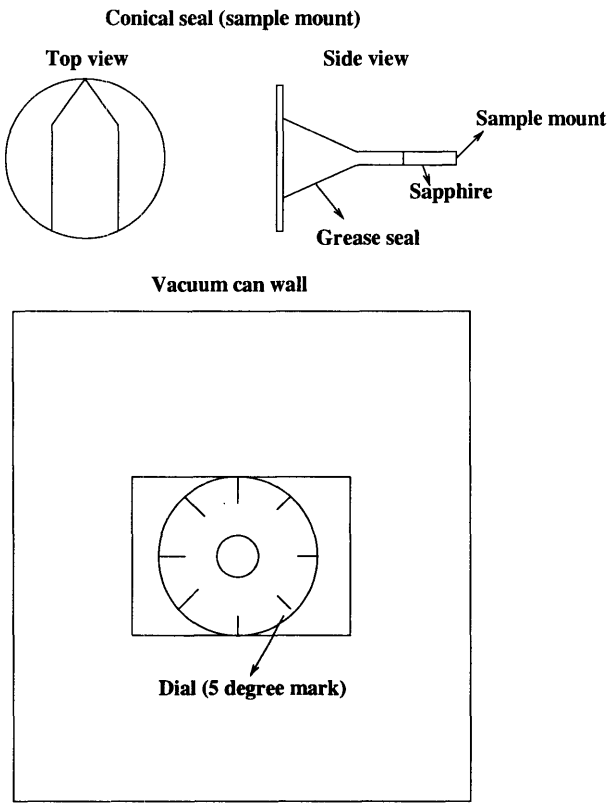

Figure 6-2: A schematic diagram of conical seal and vacuum can wall

sapphire rod attached to this copper conical seal is extended into the center of coil and the sample is mounted on the end of this sapphire rod for thermal contact. (Sapphire is used since it is the most effective in thermal conduction at low temperatures among non-conducting materials).

6.2.2 HFSS simulation with microwave cavity using horns

For continuous microwave irradiations of samples for DNP experiments, we used a horn-mirror cavity system [85, 86]. A horn-mirror system does not have a good quality factor (Q$\sim$10), but provides spacious areas to accommodate other components such as rf and gradient coils, and is easier for impedance matching. Fig. 6-3 shows reflected power versus the relative distance of the mirror from the horn at 66 GHz microwave frequency, as well as same data for a horn-horn geometry (gap between the two horns

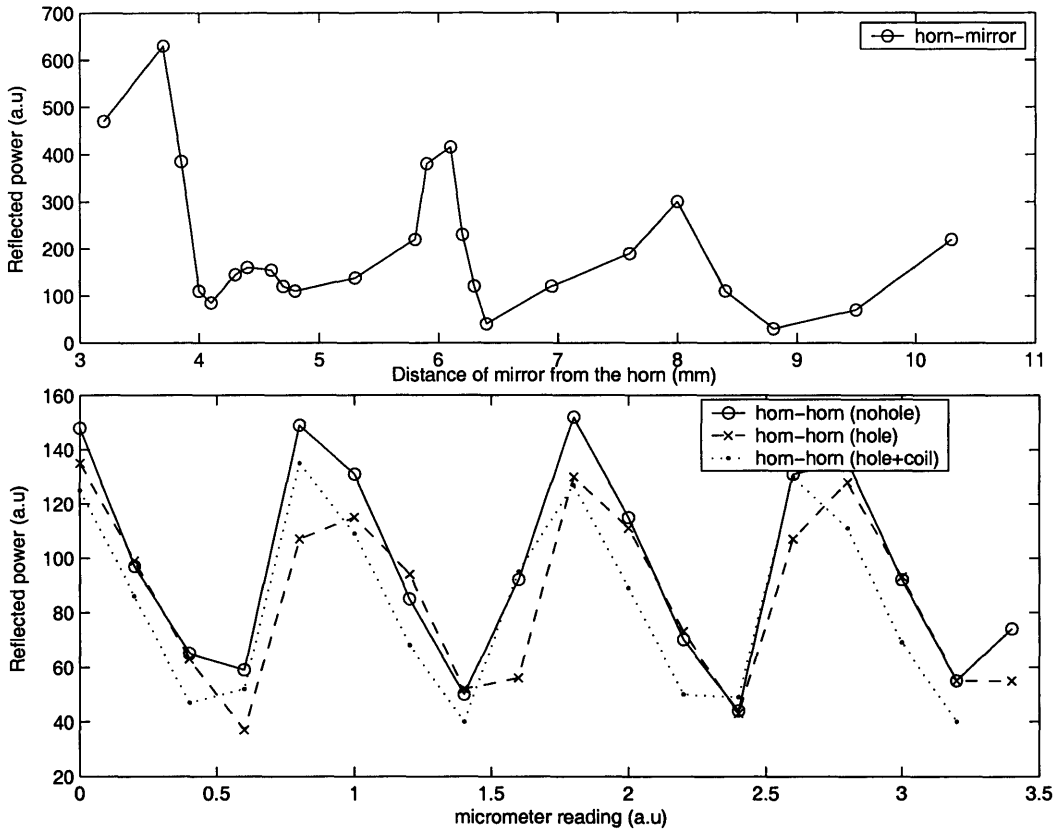

Figure 6-3: Reflected power measurements for various geometry of horn cavities. It should be noted that the micrometer reading and the location of the shorting plug inside the neck of the horn is not calibrated with respect to each other for horn-horn system, and needs to be calibrated for future references.

is set to 4.5 mm, a wavelength at 66 GHz) as a function of a sliding shorting plug that is placed within the neck of one horn. The distance between the two horns are set equal to a wavelength of microwave source to make the $3\lambda/4$ point (shown in Fig. 6-7) be the minimum E field region to minimize the distortion of the wave profiles due to the hole for rf line. In a horn-mirror geometry, a loss in microwave power is observed as the gap between the horn and the mirror increases. A double-horn scheme is seen to compensate this power loss with enhanced quality factor (Q~100).

Inside the standard rectangular waveguide (a=3.76 mm and b=1.88 mm, $a = 2b$),

a cutoff frequency of continuous microwave can be given by [83]

$$f_{\text{cutoff}} = \frac{c r_{\text{cutoff}}}{2\pi}, \tag{6.6}$$

where r_{cutoff} is

$$r^2_{\text{cutoff}} = \pi^2(\frac{m^2}{a^2} + \frac{n^2}{b^2}). \tag{6.7}$$

Integers m and n denote the modes of TE_{mn} wave.

A cutoff frequency is ~40 GHz for TE_{10} mode; therefore it is apparent that the TE_{10} wave is dominant inside the waveguide, and H field profiles of TE_{10} wave inside the waveguide are shown below [83]

$$\begin{aligned} H_z &= H_0 \cos(\frac{\pi x}{a}) e^{ikz - iwt}, \\ H_x &= -\frac{ika}{\pi} H_0 \sin(\frac{\pi x}{a}) e^{ikz - iwt}, \end{aligned} \tag{6.8}$$

where z is the direction of the wave propagation and x is the orthogonal direction to z.

To effectively see the B field profile in the horn-mirror system, we performed HFSS (High Frequency Structure Simulator, AnSoft) simulation with various configurations. Fig. 6-4 shows simulation results for B field profiles with horn, Fig. 6-5 with horn-mirror, and Fig. 6-6 with horn-horn arrangements with a 66 GHz microwave source. It is seen that horn-mirror and horn-horn configurations have 4.5 dB and 7 dB gains, respectively, in B field strength over a single horn arrangement.

Fig. 6-8 shows a CAD drawing of final probe, incorporating all the issues arising from low temperature application and microwave irradiations using a horn-mirror microwave cavity. Based on the reflected power measurement and HFSS simulation results (Fig. 6-3 and Fig. 6-6), a horn-horn microwave cavity is also designed to enhance the efficiency of microwave delivery into the sample for future applications. Fig. 6-7 shows two horn arrangements.

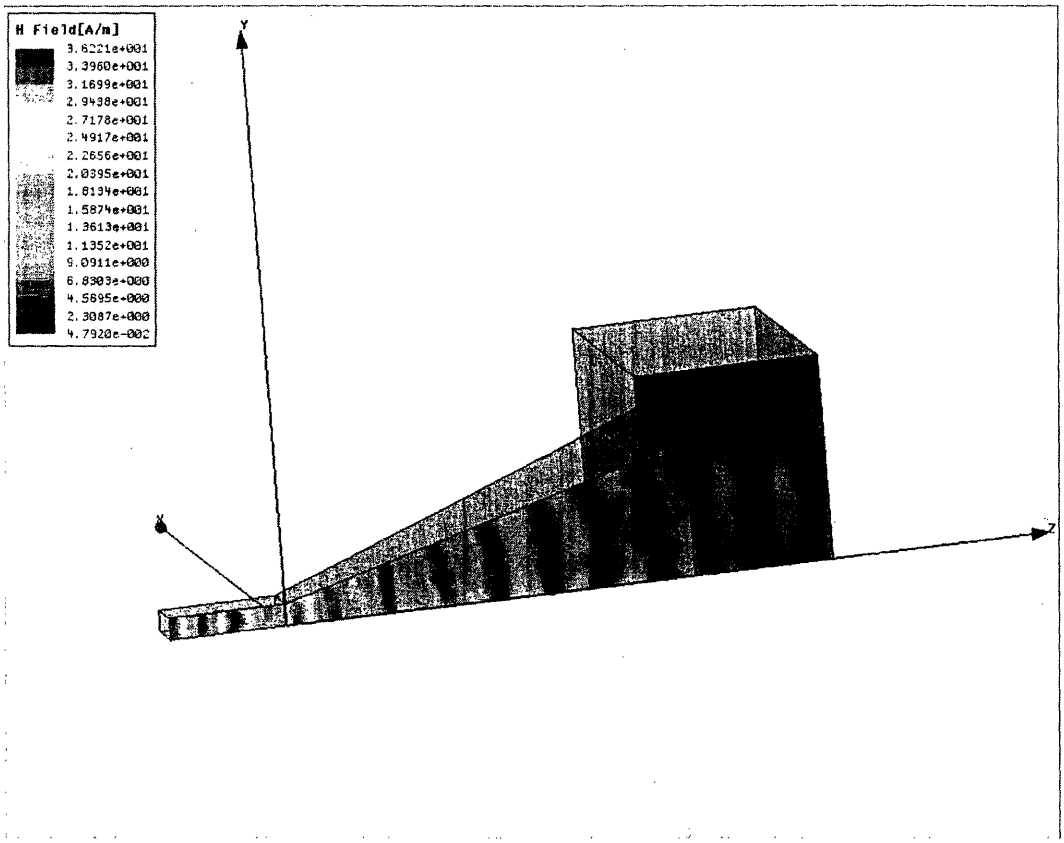

Figure 6-4: The B field profile in horn geometry

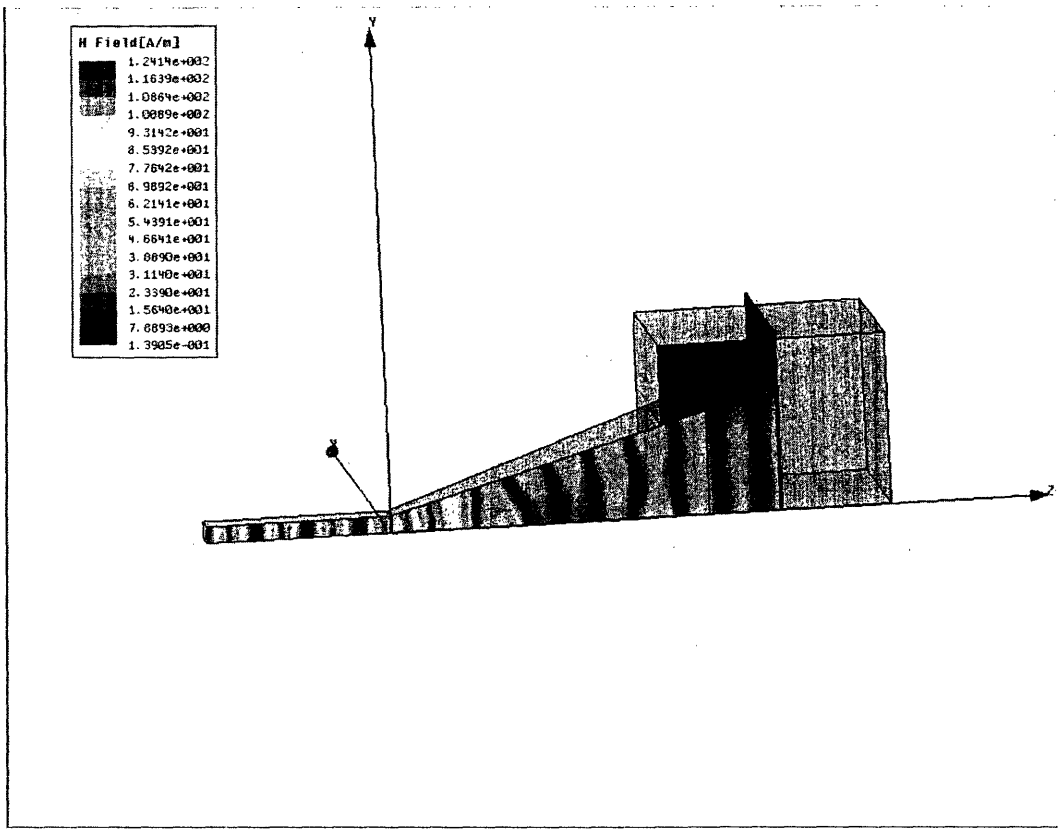

Figure 6-5: The B field profile in horn-mirror geometry

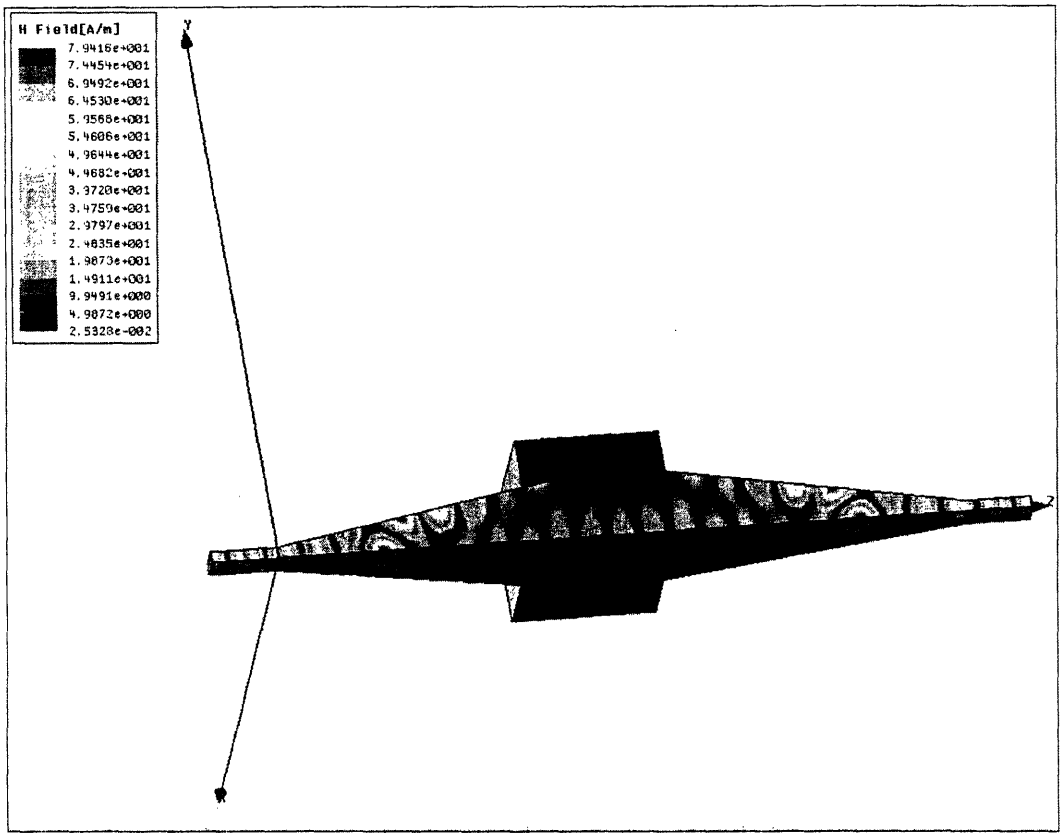

Figure 6-6: The B field profile in horn-horn geometry

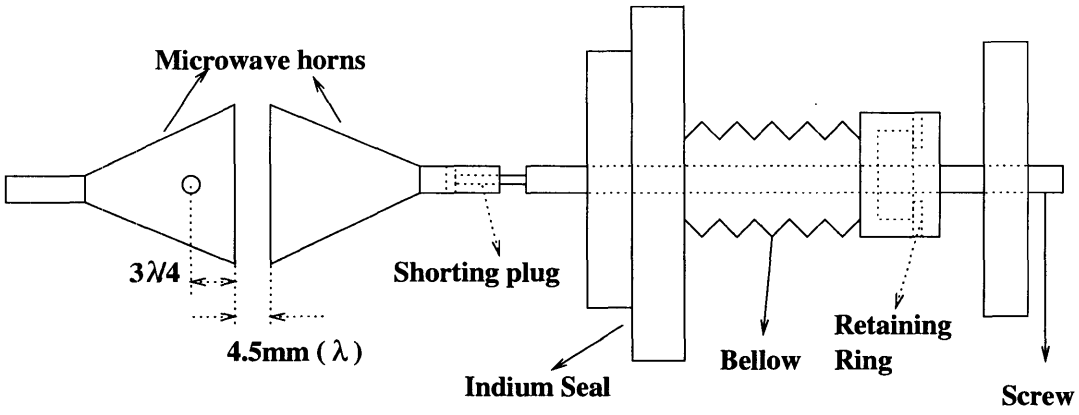

Figure 6-7: A schematic diagram of two horns arrangement

6.2.3 Microwave source

We used backshort tuned Gunn oscillator (GDM-15-4016HIR, from Millitech, LLC) with an attached isolator for our microwave source. Its center frequency is 66.2 GHz ± 0.1 GHz with mechanical tuning ability of ±2.0 GHz. Available output power of this Gunn oscillator is 40-65 mW. (Quinstar Technology, Inc can provide 1 W IMPATT oscillator with ±250 MHz tuning capability at 66 GHz, which has higher power but limited tuning range at the same frequency). To connect the probe assembly and microwave source while maintaining vacuum inside the probe assembly, we used a bulkhead flange unit (1662, from Aerowave, Inc) as a vacuum window on the top of low temperature NMR probe with mica and rubber O-ring seals. A mica window serves as a vacuum feed-through for microwave and has low insertion losses. To reduce the microwave loss while maintaining thermal isolation between the sample area and the waveguide, a 4 inch section of stainless steel waveguide was brazed into a 40 inch long coin-silver waveguide that has a smaller attenuation factor but poor thermal isolation. Fig. 6-9 describes a schematic diagram of microwave components layout for continuous irradiations with insertion loss across various components. Total loss of microwave line was ~10.6 dB, resulting in ~5 mW output microwave power on the end of the waveguide.

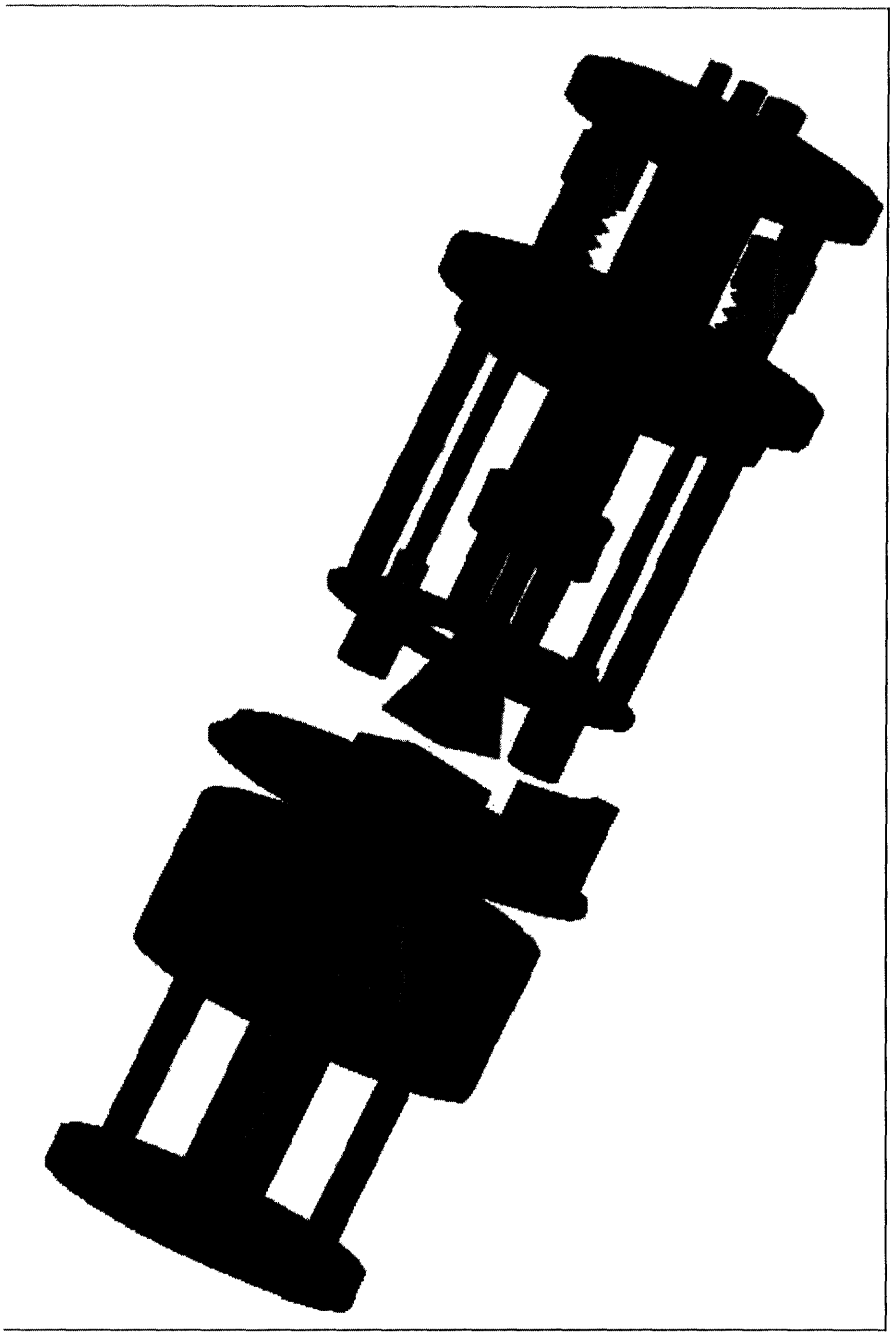

Figure 6-8: A CAD drawing for low temperature DNP probe

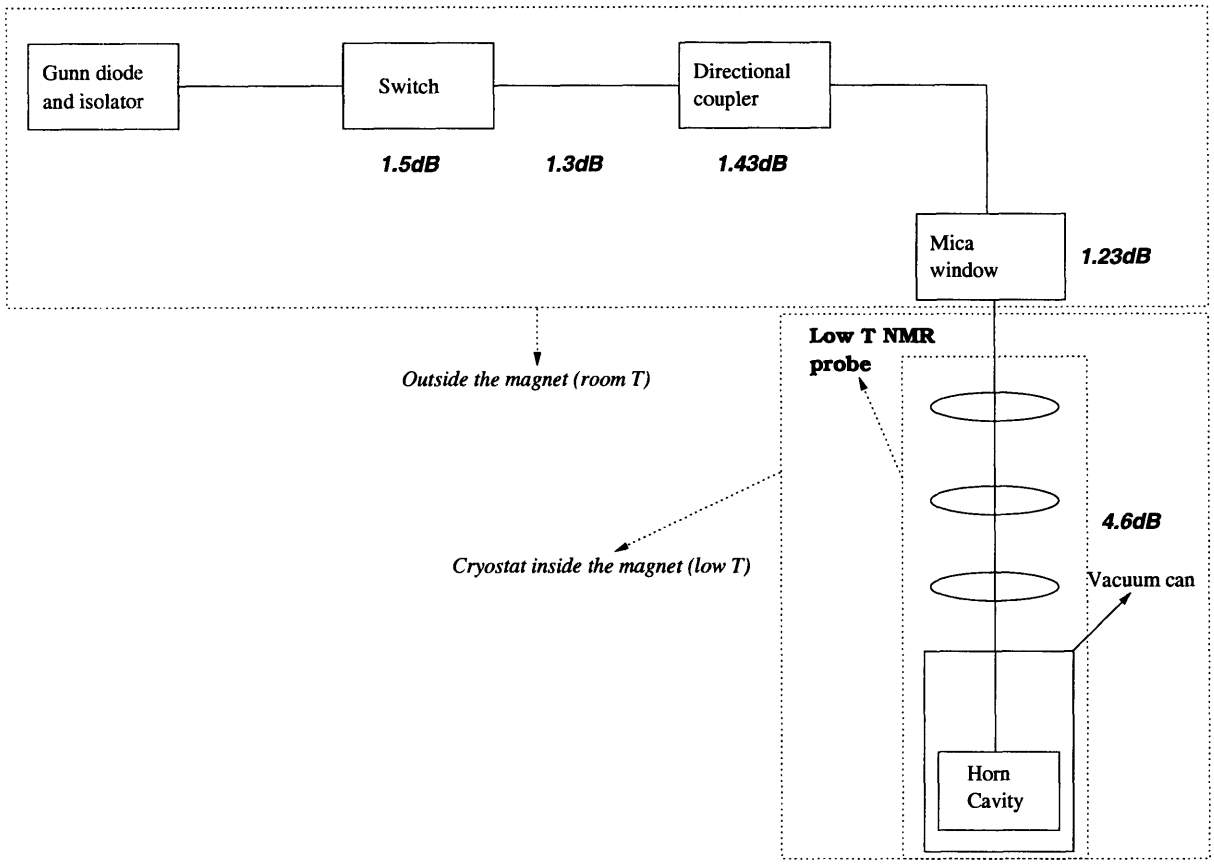

Figure 6-9: A schematic drawing for experimental setup including microwave source

6.3 Experimental results (thermal mixing : TEMPO and solid effect : BDPA)

DNP experiments are performed at 4 K at 2.35 T (94.2 MHz, ^{19}F), using a BRUKER Avance spectrometer and home built low temperature DNP probe. The samples used were a 2 mm^3 40 mM 4-amino-TEMPO (4-Amino-2,2,6,6-tetramethylpiperidine 1-Oxyl), and powder of BDPA (α,γ-Bisdiphenylene-β-phenylallyl, $C_{39}H_{29}$). 40 mM TEMPO is prepared by dissolving 0.05 g of 4-amino TEMPO with 4.38 ml of glycerol and 2.92 ml of water solution. BDPA is prepared by dissolving 1 mg of BDPA and 50 mg of polystyrene (Mw 50,000) with chloroform solvent. A free induction signal was taken at 4 K with and without continuous DNP irradiation, and the ratio of total intensity of signal is plotted as a function of microwave frequency for TEMPO in Fig. 6-10 and for BDPA in Fig. 6-11.

6.4 Discussion

We showed the design and the construction of a low temperature DNP probe with preliminary experimental DNP enhancements using TEMPO and BDPA samples. This probe enables multiple pulse irradiations at low temperature with enhanced nuclear polarization. To increase the efficiency of microwave delivery to the sample, a double horn cavity that has better quality factor and less loss is designed and fabricated for next generation low temperature DNP probe.

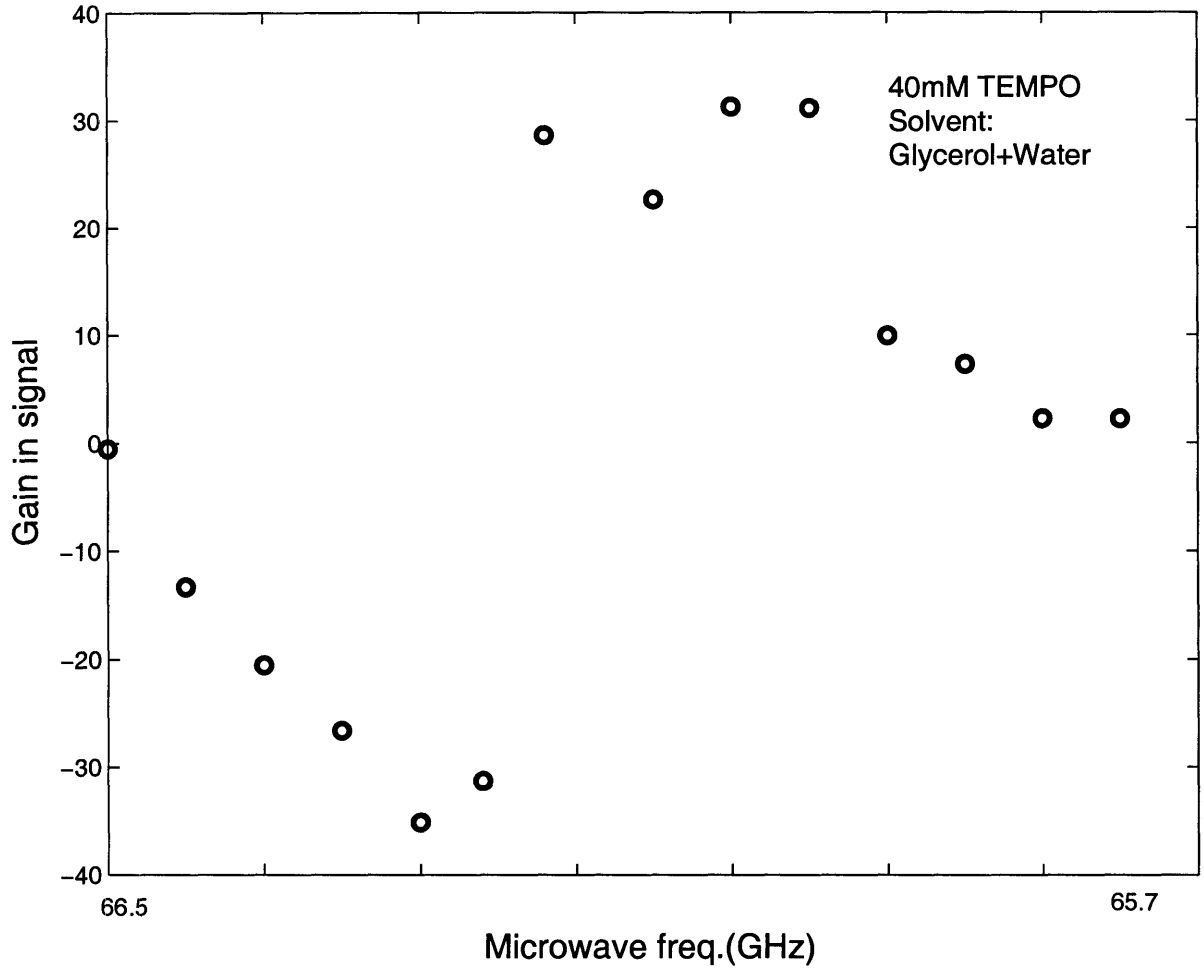

Figure 6-10: DNP enhancements of 40 mM TEMPO as a function of microwave frequency

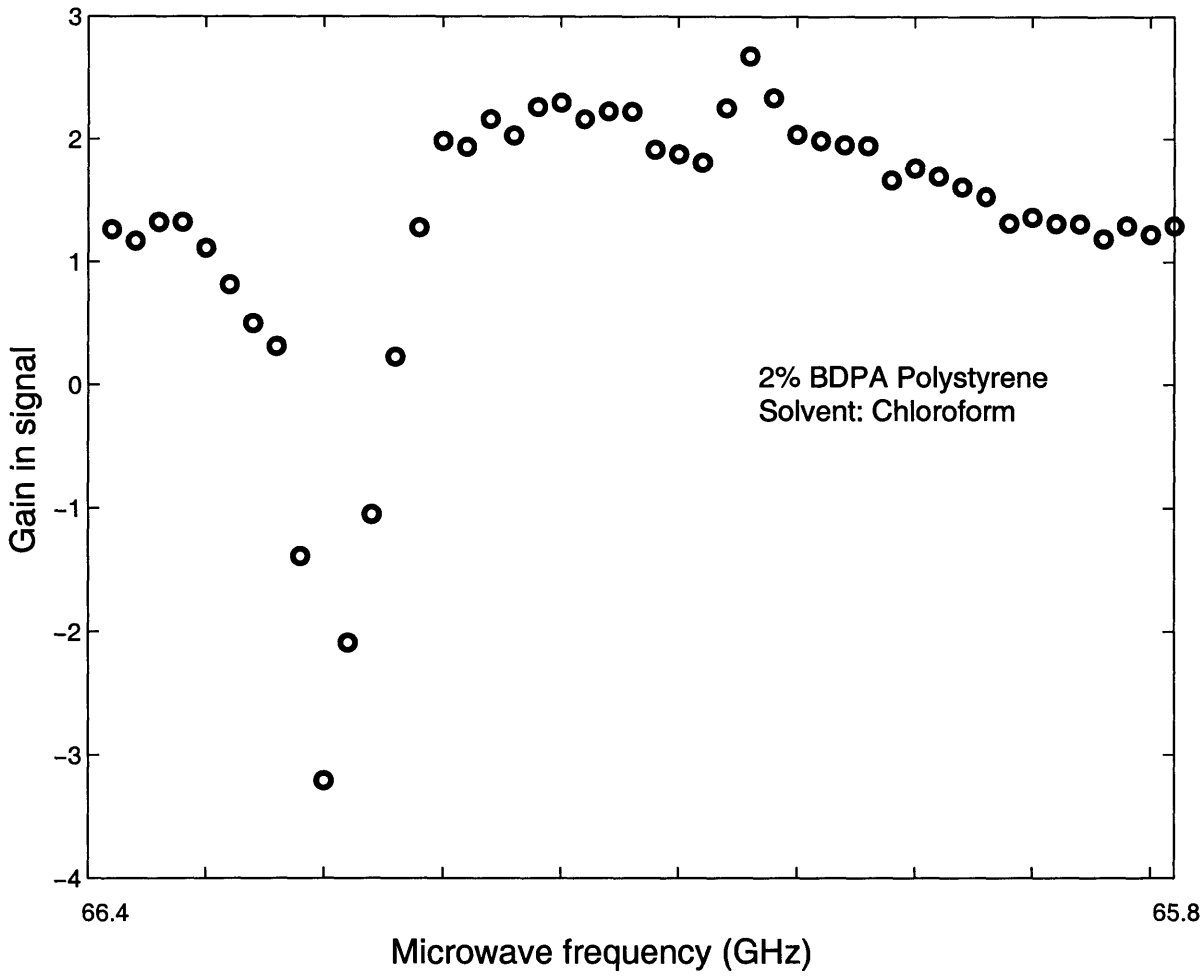

Figure 6-11: DNP enhancements of BDPA as a function of microwave frequency

Chapter 7

Conclusion

In this thesis, we provided a new experimental methods and findings, with which we can start to understand the dynamics of spins in a large Hilbert space under the action of many-body Hamiltonian.

Encoding multiple quantum coherences (MQC) in an arbitrary quantizing axis is developed, which provides new experimental tools to study the multi-spin dynamics in a dipolarly coupled spin system. We utilized this method to encode coherence numbers in an orthogonal basis to Zeeman basis and showed that the dipolar-ordered state is a two spin correlated state, and confirmed the presence of the $I_i^+ I_j^- + I_i^- I_j^+$ (flip-flop) terms in the experimentally prepared dipolar-ordered state. A new experimental investigation of the problem of the NMR free induction decay (FID) in a lattice of spin 1/2 nuclei is presented to verify the multi-spin nature of the FID and the dominant role of the geometrical arrangement of the spins in the development of higher order correlations under the dipolar evolution. This measurement provided the first direct experimental observation of the growth of coherent multiple spin correlations during the FID. Experiments were performed with a cubic lattice of spins (19^F in calcium fluoride) and a linear spin chain (19^F in fluorapatite) and the results are discussed in light of existing theoretical models. To study the dynamics and the controllability of these multiple spin correlations, effective decay times of individual coherence orders are measured under the dipolar interaction and under the control sequence that suppresses the dipolar evolution. It is seen that the decay time of each

coherence order becomes shorter and more uniform among different coherence orders as the spin correlation size grows larger in both cases.

Additional work has been done in this thesis, toward creating a pure state in solid state nuclear spins by transferring polarization from electron spins, i.e Dynamic Nuclear Polarization (DNP). A new cryogenic DNP probe was developed enabling multiple pulse irradiations at low temperature with enhanced polarization using horn-mirror cavity. To increase the efficiency of microwave delivery to the sample, a double horn cavity that has better quality factor and less loss is designed and fabricated for next generation low temperature DNP probe.

Bibliography

[1] D. G. Cory, A. F. Fahmy, and T. F. Havel, Proc. Natl. Acad. Sci. USA **94** , 1634 (1997)

[2] N. Gershenfield, and I. L. Chuang, Science. **275** , 350 (1997)

[3] D. G. Cory, R. Laflamme, E. Knill, L. Viola, T. F. Havel, N. Boulant, G. Boutis, E. Fortunato, S. Lloyd, R. Martinez, C. Negrevergne, M. Pravia, Y. Sharf, G. Teklemariam, Y.S Weinstein, and W. H. Zurek, Fortschr. Phys. **48** , 875 (2000)

[4] B. E. Kane, Nature. **393** , 133 (1998)

[5] T. D. Ladd, J. R. Goldmann, F. Yamaguchi, and Y. Yamamoto, Phys. Rev. Lett. **89** , 017901 (2002)

[6] D. Suter and K. Lim, Phys. Rev. A. **65** , 052309 (2002)

[7] A. Abragam, Principles of Nuclear Magnetism. (Clarendon Press, Oxford, 1961)

[8] W. Zhang and D. G. Cory, Phys. Rev. Lett. **80** , 1324 (1998)

[9] G. S. Boutis, D. Greenbaum, H Cho, D. G. Cory, and C. Ramanathan, Phys. Rev. Lett. **92** , 137201 (2004)

[10] C. Ramanathan, H. Cho, P. Capperallo, G. S. Boutis, D. G. Cory, Chem. Phys. Lett. **369**, 311 (2003).

[11] C. Ramanathan, H. Cho, P. Capperallo, G. S. Boutis, D. G. Cory, 'Exploring large nuclear spin systems in the solid state using NMR,' in Proceedings of the

6th International Conference on Quantum Communication, Measurement and Computing , Eds. Jeffrey H. Shapiro and Osamu Hirota, pp. 267-270, Rinton Press (2003).

[12] H. Cho, D. G. Cory, and C. Ramanathan, J. Chem. Phys. **118** , 3686 (2003)

[13] H. Cho, T. D. Ladd, J. Baugh, D. G. Cory, and C. Ramanathan, submitted to Phys. Rev. B, cond-mat/0501578.

[14] S. Sinton and A. Pines, Chem. Phys. Lett. **76** , 263 (1980)

[15] H. Hatanaka, T. Terao, and T. Hashi, J. Phys. Soc. Japan. **39** , 835 (1975)

[16] A. Pines, D. J. Ruben, S. Vega, and M. Mehring, Phys. Rev. Lett. **36** , 110 (1976)

[17] W. P. Aue, E. Batholdi, and R. R. Ernst, J. Chem. Phys. **64** , 2229 (1976)

[18] S. Vega, T. W. Shattuck, and A. Pines, Phys. Rev. Lett. **37** , 43 (1976)

[19] G. Bodenhausen, Progr. NMR Spectrosc. **14** , 137 (1981)

[20] D. P. Weitekamp, Adv. Magn. Reson. **11** , 111 (1983)

[21] G. Drobny, Ann. Rev, Phys. Chem. **26** , 451 (1985)

[22] M. Munowitz, Coherence and NMR. A Willey-Interscience publication, (1988)

[23] M. Munowitz and A. Pines, Adv. Chem. Phys. **66** , 1 (1987)

[24] W. S. Warren, S. Sinton, D.P. Weitekamp and A. Pines, Phys. Rev. Lett. **43** , 1791 (1979)

[25] W. S. Warren, D.P. Weitekamp and A. Pines, J. Chem. Phys. **73** , 2084 (1980)

[26] Y. -S. Yen, and A. Pines, J. Chem. Phys. **78**, 3579 (1982).

[27] J.Baum, M. Munowitz, A. N. Garroway, and A. Pines, J. Chem. Phys. **83**, 2015 (1985).

[28] J.Baum and A. Pines, J. Am. Chem. Soc. **108**, 7447 (1986).

[29] R. Tycko, J. Magn. Reson. **139**, 302 (1999).

[30] M. Munowitz and A. Pines, Science. **233**, 525 (1986).

[31] S.Lacelle, S. -J. Hwang, and B. C. Gerstein, J. Chem. Phys. **99**, 8407 (1993).

[32] E. B. Feldman and S.Lacelle, J. Chem. Phys. **107**, 7067 (1997).

[33] A. K. Khitrin, Phys. Lett. A. **228**, 317 (1997).

[34] S.Lacelle, Adv. Magn. Reson. **16**, 193 (1991).

[35] L. Emsley and A. Pines in: B. Maraviglia (Ed.) , Proceedings of the International School of Physics (Enrico Fermi). p. 123 (1994).

[36] D. A. Lathrop, E. S. Handy, and K. K. Gleason, J. Magn. Reson. Series A. **111**, 161 (1994).

[37] D. Suter and J.G. Pearson, Chem. Phys. Lett. **144** , 328 (1988)

[38] Y. Zhang, W. E. Mass, and, D. G. Cory, Mol. Phys. **86**, 347 (1995)

[39] I. J. Lowe and R. E. Norberg, Phys. Rev. **107**, 46 (1957).

[40] D. G. Cory, J. B. Miller, and, A. N. Garroway, J. Magn. Reson. **90**, 205 (1990)

[41] C. P. Slichter and W. C. Holton, Phys. Rev. **122**, 1701 (1961)

[42] A. G. Anderson and S. R. Hartmann, Phys. Rev. **128**, 2023 (1962)

[43] A. G. Redfield, Phys. Rev. **98**, 1787 (1955).

[44] J. Jeener and P. Broekaert, Phys. Rev. **157**, 232 (1967)

[45] P. Broekaert and J. Jeener, Phys. Rev. B. **15**, 4168 (1977)

[46] S. Emid, A. Bax, J. Konojnendijk, and J. Smidt, Physica B&C. **96**B, 333 (1979)

[47] S. Emid, A. Bax, J. Konojnendijk, and J. Smidt, Physica B&C. **100**B, 215 (1990)

[48] S. Emid, A. F. Mehlkopf, J. Smidt, and N. Yousef, J. Magn. Reson. **50**, 165 (1985)

[49] I. J. Lowe and R. E. Norberg, Phys. Rev. **107**, 46 (1957)

[50] A. A. Ludin and B. N. Provotorov, Phys. Lett. A. **55**, 426 (1976)

[51] F. Lado, J. D. Memory, and G. W. Parker, Phys. Rev. B. **4**, 1406 (1971).

[52] B. V. Fine, Phys. Rev. Lett. **79**, 4673 (1997).

[53] A. A. Nevzorov, and J. H. Freed, J. Chem. Phys. **112**, 1425 (2000).

[54] A. A. Nevzorov, and J. H. Freed, J. Chem. Phys. **115**, 2401 (2001).

[55] M. Engelsberg, I. J. Lowe, and J. L. Carolan, Phys. Rev. B. **7**, 924 (1973)

[56] M. Engelsberg, and I. J. Lowe, Phys. Rev. B. **10**, 822 (1974).

[57] M. Munowitz, and M. Mehring, Chem. Phys. **116**, 79 (1987).

[58] J. H. van Vleck, Phys. Rev. **74**, 1168 (1948).

[59] W. -K. Rhim, A. Pines, and J. S. Waugh, Phys. Rev. B. **3**, 684 (1971).

[60] N.G. Van Kampen, Stochastic Processes in Physics and Chemistry. North-Holland, (1992).

[61] M. Munowitz, A. Pines, and M. Mehring, J. Chem. Phys. **86**, 3172 (1987).

[62] D. Suter, S. B. Liu, J. Baum, A. Pines, Chem. Phys. **114**, 103 (1987).

[63] S. Lacelle, Adv. Magn. Opt. Reson. **15**, 173 (1991).

[64] D. H. Levy, and K. K. Gleason, J. Phys. Chem. **96**, 8125 (1992).

[65] G. Cho and J. P. Yesinowski , J. Phys. Chem. **100**, 8125 (1996).

[66] U. Haeberlen and J. S. Waugh, Phys. Rev. **175**, 453 (1968).

[67] W. -K. Rhim, A. Pines, J. S. Waugh, Phys. Rev. B. **3**, 684(1971).

[68] W. -K. Rhim, D. D Elleman, R. W. Vaugan, J. Chem. Phys. **58**, 1772 (1973).

[69] J. S. Waugh, L. M. Huber, U. Haeberlen, Phys. Rev. Lett. **20**, 180 (1968).

[70] C. H. Wang and J. D. Ramshaw, Phys. Rev. B. **6**, 3253 (1972).

[71] P. Mansfield and U. Haeberlen, Z. Naturforch. **28**, 1081 (1973).

[72] S. Idziak and U. Haeberlen, J. Magn. Reson. **50**, 281 (1982).

[73] U. Haeberlen, High resolution NMR in Solids : Selective Averaging. Academic Press, (1976).

[74] B. C. Gerstein and C. R. Dybowski, Transient Techniques in NMR of Solids : An Introduction to Theory and Practice. Academic Press, (1985).

[75] D. P. Burum and W. K. Rhim, J. Chem. Phys. **71**, 944 (1979).

[76] M. Linder, D. P. Burum and R. R. Ernst, J. Magn. Reson. **43**, 463 (1981).

[77] M. Maricq, Phys. Rev. B. **25**, 6622 (1982).

[78] G. S. Boutis, P. Cappellaro, H Cho, C. Ramanathan, and D. G. Cory, J. Magn. Reson. **161** , 132 (2003)

[79] A. W. Overhauser, Phys. Rev. **92**, 411 (1953).

[80] M. Goldman, Spin Temperature and NMR in Solids. (Clarendon Press, Oxford, 1970).

[81] A. Abragam and M. Goldman, Nuclear Magnetism : Order and Disorder. (Clarendon Press, Oxford, 1982).

[82] R. A. Wind, M. J. Duijvestijn, C. van der Lugt, A. Manenschijn, and J. Vriend, Prog. NMR Spectrosc. **17**, 33 (1985).

[83] C. P. Poole, Electron spin resonance. DOVER PUBLICATION, INC, (1983).

[84] M. J. Duijvestijn, R. A. Wind, and J. Smidt, Physica B. **138**, 147 (1986).

[85] E. S. Gravlin, and J. A. Cowen, Am. J. Phys. **27**, 566 (1959).

[86] H. Nishiguchi, S. Sugito, and N. Hirota, J. Magn. Reson. **68**, 40 (1986).

[87] R. A. Mckay, U. S. Patent., 4,446,431 (1984).